Small scale testing of crawler outlet diffusers for plume reduction of offshore mining

Jorge Osejo Rodriguez

DELFT UNIVERSITY OF TECHNOLOGY

MASTER THESIS
REPORT

Small scale testing of crawler outlet diffusers for plume reduction of offshore mining

Author:
J. A. Osejo Rodriguez - Student Number: 4723384

Graduation committee:

Dr. Ir. A.M. Talmon   *TU DELFT - Dredging Engineering Section (**Chairman**)*
Dr. Ir. R.L.J. Helmons   *TU DELFT - Dredging Engineering Section*
Prof. Dr. Ir. C. Poelma *TU DELFT - Laboratory for Aero and Hydrodynamics*
Ir. S.J. Dasselaar   *ROYAL IHC - IHC Mining*

29 October 2019

Delft
University of
Technology

para Andrea

Abstract

Over recent years, there has been an increase in demands for rare and precious minerals worldwide. Mostly this is due to the rise of the world's population and because of the drive towards a green energy transition and low carbon economy. Prices are rapidly increasing, and there is an identifiable risk of an increasing supply shortage of raw materials, including those identified as critical to Europe's high technology sector. The development of surveying techniques and advances in new technologies in remotely operated vehicles (ROV) has allowed to detect that the most valuable and rare mineral resources are spread out in the sea-floor and international waters.

Currently, the most significant setback towards exploitation licenses is not because of lack of technology but because of a lack of knowledge on deep-sea biodiversity and the impacts of mining on ecosystems. The ISA (International Seabed Authority) is responsible for the regulation and the control of mineral-related activities in the international waters is currently working on drafting environmental regulations. This presents significant opportunities for research on the development of technologies that will incur in the least environmental impact possible. Currently, the main concerns are regarding the horizontal sediment-laden plume that is generated as a result of the mining process. Therefore, the industry is working towards the development of equipment that lessens the plumes spread by using diffusers to reduce the momentum of the flow.

Work done in this research focuses on small scale sized laboratory experiments in which the sea-floor crawler's outlet shape is varied, and its plume's effects of the sediment waste and other effluents (SWOE) are measured. Besides gaining insight in the horizontal plume spreading under different conditions and geometries, the outcome of the research is to provide a set of measurement data that can be used for future numerical model validation towards determining an optimal outlet shape for the seabed crawler. For this purpose, a total of three diffusers were designed and tested based on a specific scaling factor and input parameters defined by IHC Mining.

A total of 19 experiments of horizontal offset jets are performed in which synthetic spherical glass particles were used to recreate the sediment found in the ocean sea-floor. Experiments consisted of capturing visual imagery of the generated plume on both top and side views for further analysis and performing velocity and concentration profile measurements in different locations. The offset jet transition from jet to plume and the respective impingement point for all diffusers was compared. Velocity and concentrations measurements were analyzed and compared to determine an ideal diffuser.

Using diffusers reduces the plume's initial momentum while maintaining the density differences and therefore reduces the transition from jet to plume, allowing for gentler deposition over the surface and resuspending less material. All experiments show similar behavior in which a free jet can be observed initially. Then substantial entrainment can take place the jet impacts on the seabed due to the negative buoyancy. Once the discharge impinges the lower boundary, it forms a radially spreading layer along the boundary which transitions into a wall jet. This area is also known as a turbidity current.

Keywords: Deep-Sea Mining, small scale experimental work, horizontal plumes, offset jets, diffusers, wall jets, velocity and concentration profiles.

Acknowledgments

Furthermore, I wish to express my sincere gratitude an appreciation to all the people who have helped me, often without knowing, during my full master program at TU Delft.

First, I would like to thank my committee members who were involved in my final graduation project for guiding me in the right direction. I sincerely thank my supervisor Rudy Helmons, not only for suggesting the topic and presenting it as a challenge but also for his enormous commitment, support, and advice during the length of the investigation. I want to acknowledge my indebtedness and my warmest thanks to my company supervisor, Siemen Dasselaar. His friendly guidance, constant support, and expert advice have been invaluable throughout all stages of the work. I would also like to thank Arno Talmon and Christian Poelma for their valuable comments, extended discussions and helpful suggestions that have contributed to improving this thesis.

My gratitude to the professors and Ph.D. students at the TU dredging department: Cees van Rhee, Geert Keetels, Xihuan Chen and Edwin de Hoog for sharing their truthful and illuminating views on several issues related to the project. Specifically, I'd like to thank Frans Grunsven for his invaluable advice and expertise that was critical during the early stages of the project. Also, I would like to thank Mohammed Elerian and Dennis van Pouderoijen for lending me extra hands to perform the tiring experiments.

I would also like to thank the TU Delft dredging laboratory staff Ed Stok and Freek Brakel for lending me their knowledge and resources during my experiments. Specifically I would like to thank Andre van den Bosch. Without his problem-solving solutions and extra pair of hands, it would not have been possible to conclude the experimental investigation.

I am grateful to Royal IHC for their hospitality and collaboration during the time I spent in their company. Specifically, I would like to thank Jort van Wijk and Maarten in t' Veld at IHC MTI for opening their doors of the company and allowing me to start my research exercise. A special thanks to Hans Greve, Robin Hageman, and Wiebe Boomsma for giving me the opportunity and resources to carry out my graduation project in IHC Mining. My most profound appreciation to Jazzie Hoebe and Martijn van de Berg for their help in my 3D printing diffuser design. Finally, I would like to thank all IHC staff for the kind, and warm environment felt during my stay in their office.

I want to express my gratitude to my family for their encouragement and unreserved and unwavering love. To my friends, both inside and outside the Netherlands for their unconditional support that made it possible for me to spend time far away from home.

<div align="right">J.Osejo (Delft, October 2019)</div>

Contents

List of Figures

List of Tables

Introduction

1.1. General Background

Throughout the years, the demands for rare and precious minerals have increased primarily due to the rise of the world's population and the drive towards a low carbon economy. Commodity prices rapidly rise, and there is an identifiable risk of an increasing supply shortage of raw materials, including those identified as critical to Europe's high technology sector.

At present, the EU imports 77 % of its critical raw materials, furthermore as shown in Figure 1.1, supplies of precious metals from land base mines have not always been reliable due to a limited number of primary producers and are expected to decrease with an increase in competition for metal resources from expanding economies (i.e. China, India, Brazil, Indonesia) (Hein et al., 2013)[20].

Element	Leading Producer	2nd Producer	3rd Producer
Aluminum	Australia (31%)	China (18%)	Brazil (14%)
Arsenic	China (47%)	Chile (21%)	Morocco (13%)
Cadmium	China (23%)	Korea (12%)	Kazakhstan (11%)
Chromium	South Africa (42%)	India (17%)	Kazakhstan (16%)
Cobalt	Congo (40%)	Australia (10%)	China (10%)
Copper	Chile (34%)	Peru (8%)	USA (8%)
Gallium	China	Germany	Kazakhstan
Germanium	China (71%)	Russia (4%)	USA (3%)
Gold	China (13%)	Australia (9%)	USA (9%)
Helium	USA (63%)	Algeria (19%)	Qatar (12%)
Indium	China (50%)	Korea (14%)	Japan (10%)
Iron	China (39%)	Brazil (17%)	Australia (16%)
Lead	China (43%)	Australia (13%)	USA (10%)
Lithium	Chile (41%)	Australia (24%)	China (13%)
Manganese	China (25%)	Australia (17%)	South Africa (14%)
Molybdenum	China (39%)	USA (25%)	Chile (16%)
Nickel	Russia (19%)	Indonesia (13%)	Canada (13%)
Niobium	Brazil (92%)	Canada (7%)	—
Palladium	Russia (41%)	South Africa (41%)	USA (6%)
Platinum	South Africa (79%)	Russia (11%)	Zimbabwe (3%)
Rare Earths	China (97%)	India (2%)	Brazil (1%)
Selenium	Japan (50%)	Belgium (13%)	Canada (10%)
Silver	Peru (18%)	China (14%)	Mexico (12%)
Tellurium	Chile	USA	Peru
Tin	China (37%)	Indonesia (33%)	Peru (12%)
Uranium	Canada (21%)	Kazakhstan (19%)	Australia (19%)
Vanadium	China (37%)	South Africa (35%)	Russia (26%)
Zinc	China (25%)	Peru (13%)	Australia (12%)

Figure 1.1: Leading global metal producers. Elements highlighted in blue are common in marine deposits

Source: *Hein et al.(2013)*[20]

China is currently the major producer of 30 critical metals, and the Chinese exports of these metals are decreasing as more of their production is being used internally. This forces the EU to establish a more diverse import market for the sake of securing domestic industries against market shocks and increased prices (TNO, 2015)[55].

Previously mining in the sea had only occurred under the sea bed harvesting hydrocarbons such as oil and gas. However, with advances in surveying technologies, mainly photographic and video imaging and the development of new technologies such as autonomous underwater vehicles (AUV), remotely operated underwater vehicles (ROV) and artificial seismic source waves, efficient techniques have been developed which have allowed to detect resources in broader areas of seafloor (Halbach et al. 1988)[19]. This has set forth the discovery that a vast amount of the world's most valuable and rare mineral resources can be found several kilometers beneath the ocean surface and in international waters.
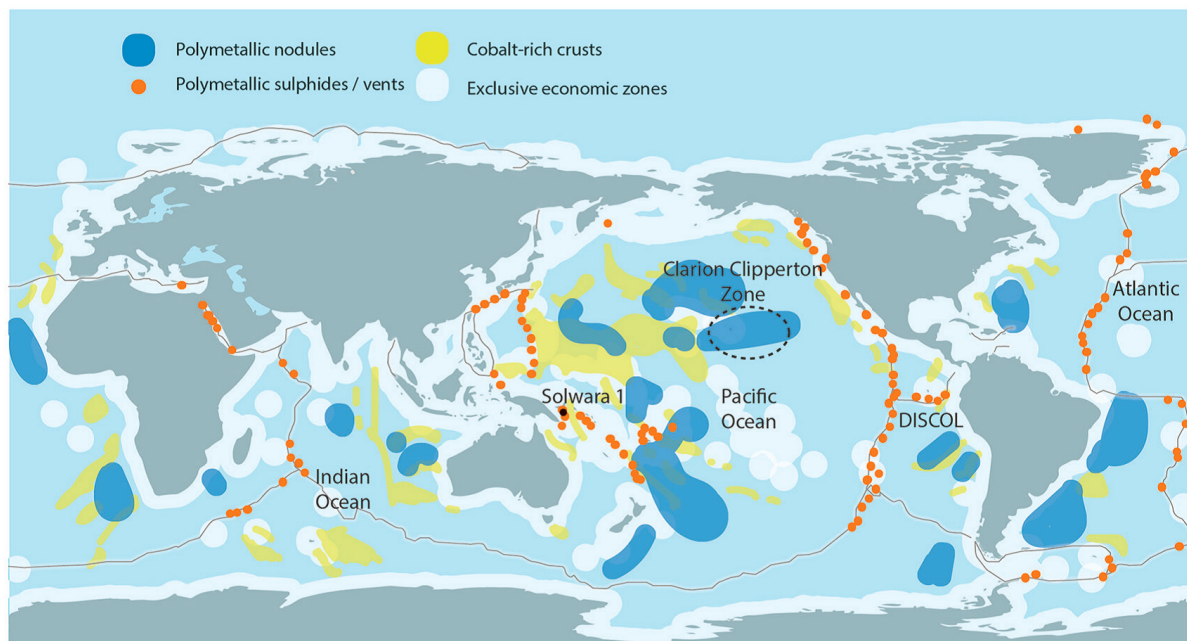
Figure 1.2: World map showing the location of the three main marine mineral deposits

Source: *Miller et al. (2018)*[34]

With this discovery, alongside depletion of land-based reserves, the commercial viability of deep-sea mining industry has been increasingly boosting. The continuous growing demand for raw materials used commonly in smart electronics is also crucial for green technologies, such as solar power and electric cars. These technologies are driving the prices for metals such as copper, cobalt, magnesium, lithium and other rare metals, incentivizing further developments to explore these mineral deposits in the deep seas.

Since the late 70s, the mining industry has been hard at work developing specialized dredgers, pumps, risers, booster stations, crawlers, drills, platforms, cutters and corers, many of them robotic and all designed to work in the harsh conditions of the deep sea. Seafloor mining has the potential to help meet the demand for many materials used worldwide and could help bolster the economies of developing nations (van Muijen, 2017)[36].

However, the extremely hostile operational conditions found on the ocean floor present specific challenges, both technically and environmentally, which are extremely complex and completely different from land-based mining.

Deep-sea mining would especially have significant impacts, as has been documented in various scientific reports. Given the broad lack of knowledge of the benthic zones, it is difficult to estimate the extent of these impacts and the potential resilience of species following the disturbance caused by mining. Therefore, the

development of regulations has been complicated, hindering the exploitation phases of deep-sea mining until a better grasp of the extent of the environmental damage is known.

1.2. Deep Sea Mining

The extraction of different types of minerals from the seafloor vastly varies depending on the habitat types the minerals are located. The three main types of mineral deposits of commercial interest are the polymetallic nodules (Mn) commonly found in the abyssal plain, the seafloor massive sulfides (SMS) located at hydrothermal vents and the cobalt-rich crusts which are found at seamounts and mid-ocean ridges. All these mineral deposits present unique challenges. However, they are based on similar concepts of using a seabed resource collector, a lifting system, and a support vessel for processing and transporting, as shown in Figure 1.3.
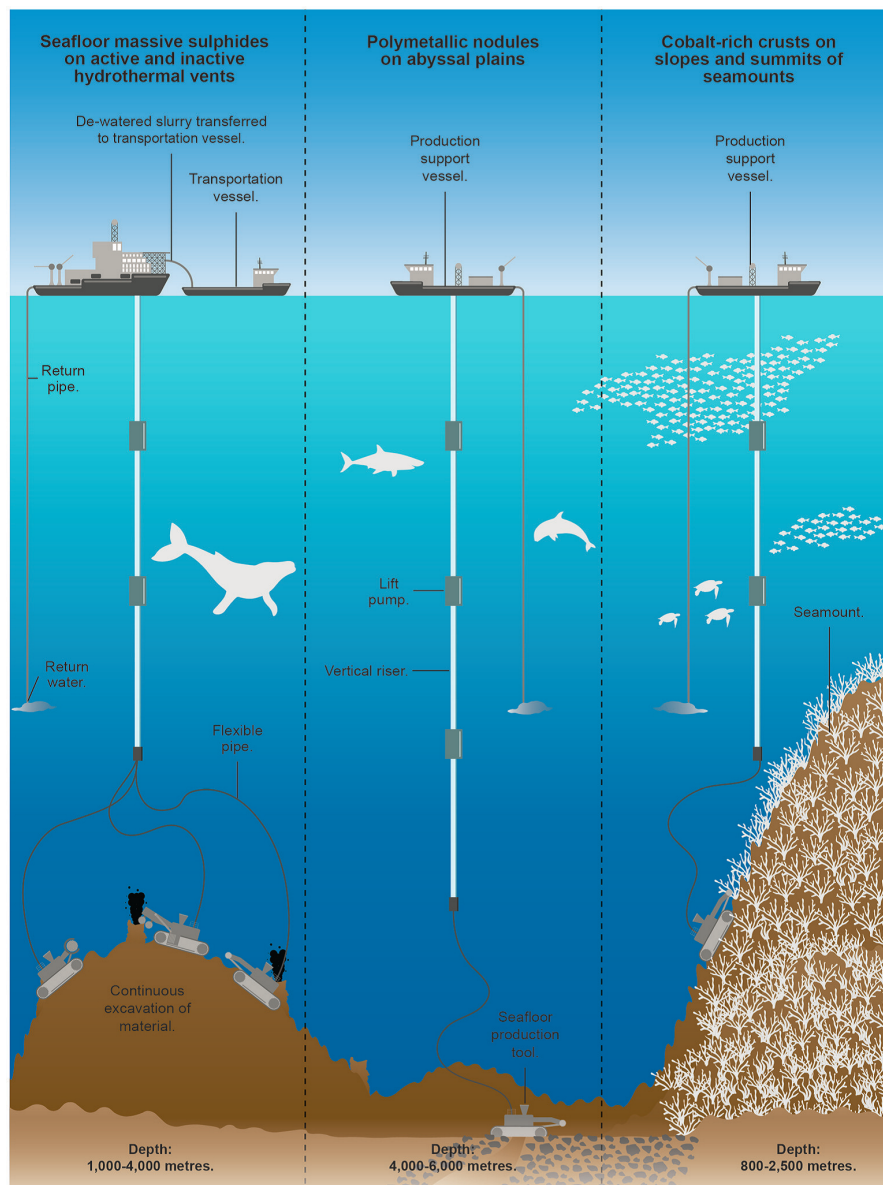
Figure 1.3: Schematic showing the processes involved in deep-sea mining for the three main types of mineral deposit.

Source: *Miller et al. (2018)*[34]

1.2.1. Characteristics of Mineral Deposits

Polymetallic Nodules

Polymetallic nodules are shown in Figure 1.4a are formations of 40% water and 60% mineral containing rich concentrations of mainly manganese, nickel, copper, and cobalt. They are positioned at the sediment surface, roughly 50% above and below the sediment-water interface. They are located on the abyssal plains at depths of 3,000 to 5,500 meters and are spread out over a vast area. Nodules have a potato-like shape with a diameter of 5 to 10 cm and grow extremely slowly (Hein, 2016)[21].

The most significant nodule deposit has been found in the Clarion-Clipperton Zone (CCZ), a great abyssal plain as vast as the United States located on the eastern Pacific Ocean. Very few studies have investigated nodule fauna because of their inaccessibility, but they have been reported to provide some of the only hard substrates for marine species at those locations and therefore removal may result in significant habitat loss.

Seafloor Massive Sulfides

Seafloor massive sulfides (SMS) as shown in Figure 1.4b is associated with both active and inactive hydrothermal vents. These are located along oceanic ridges and were discovered in depths that vary from 1500 to 3500 meters in the late 1970s. Hydrothermal vents on the seabed release superheated solutions that undergo a chemical process generating high concentrations of valuable minerals (Miller et al.2018)[34]. Deposits formed by these eruptions, along with shallow subsurface deposits, have a high sulfide content and are also rich in copper, gold, zinc, lead, barium, and silver.

SMS are concentrated in small areas of less than one square kilometer. Their mining can only be possible near inactive hydrothermal vents due to the high temperatures and environmental impact towards organisms present in active vents.

Cobalt Rich-Crusts

Cobalt-rich crusts, also referred to as ferromanganese crusts shown in Figure 1.4c. They are formed on the slopes and summits of seamounts in the depths of 800 to 2500 meters and cover areas of several square kilometers. Crusts are composed mainly of iron and manganese. They also reportedly contain three times more cobalt and five times more platinum than terrestrial deposits (Hein et al., 2013).

The basic exploitation method is to remove the crusted skin by means of ROV without including too much of the rock beneath it. The crust thickness usually varies between 10 to 15 centimeters. The possibility of mining crusts has been the subject of little investigation and few exploration campaigns have been undertaken since it is technologically more challenging than harvesting polymetallic nodules and seafloor massive sulfides from abyssal plains due to the high slopped and uneven terrain over which they are located and their delicate extraction process.

(a) Polymetallic Manganese Nodules

(b) Seafloor Massive Sulfides

(c) Cobalt Rich-Crusts
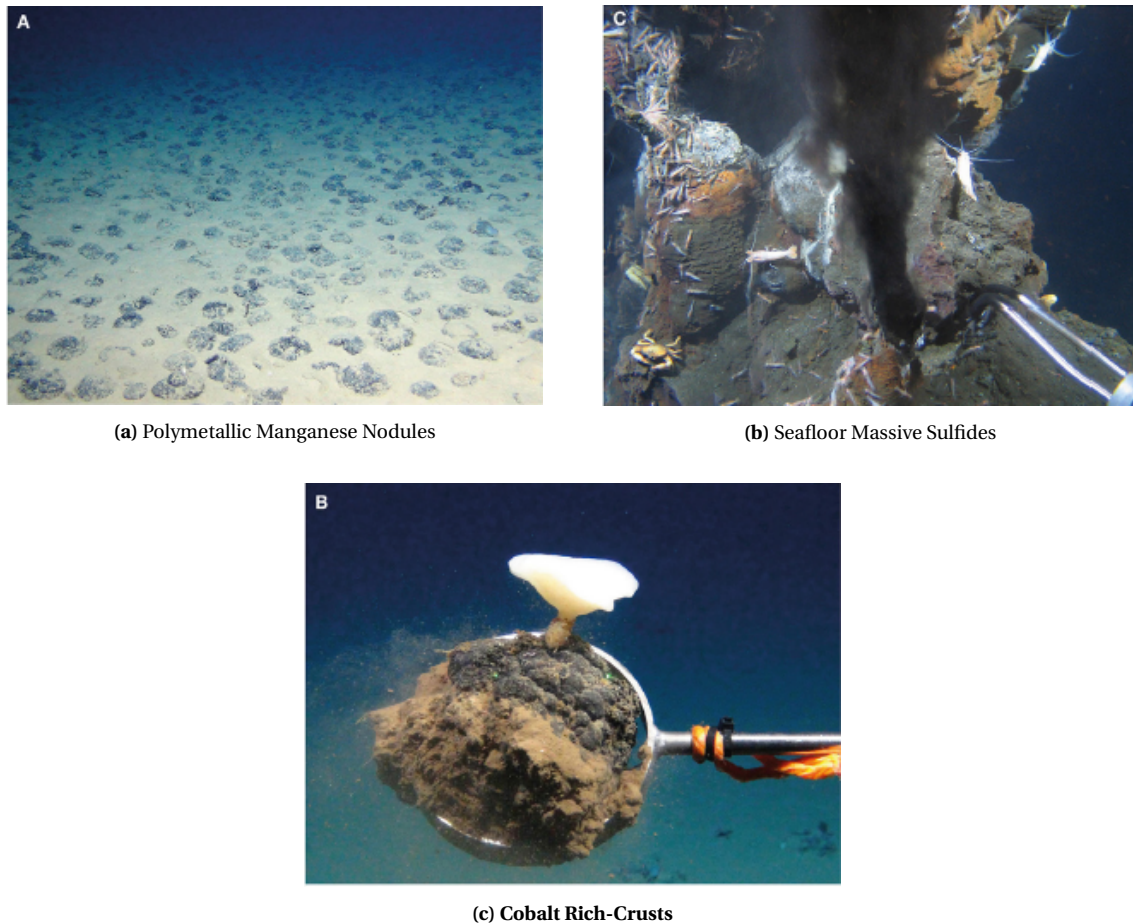
Figure 1.4: Types of mineral deposits

Source: *Miller et al. (2018)*[34]

1.2.2. Deep-Sea Mining Equipment

Extraction technologies for deep-sea mining vary significantly compared to onshore mining. Deep-sea mining's primary constraint is that it must be carried out by remote methods controlled from a floating support vessel (Figure 1.5). Also, every mining site is significantly different presenting multiple variables such as different water depths, temperatures, and seabed topography.

Deep-sea mining can be split into several processes listed below (Ecorys, 2014)[13]

1. Excavating/Cutting of the deposit with the least amount of associated sediments;

2. Vertical transport of both the ore and the least amount of sediments to the support vessel;

3. Separation of precious minerals ore from associated sediments and disposal of sediments;

4. Transportation of ore to shore for further processing.
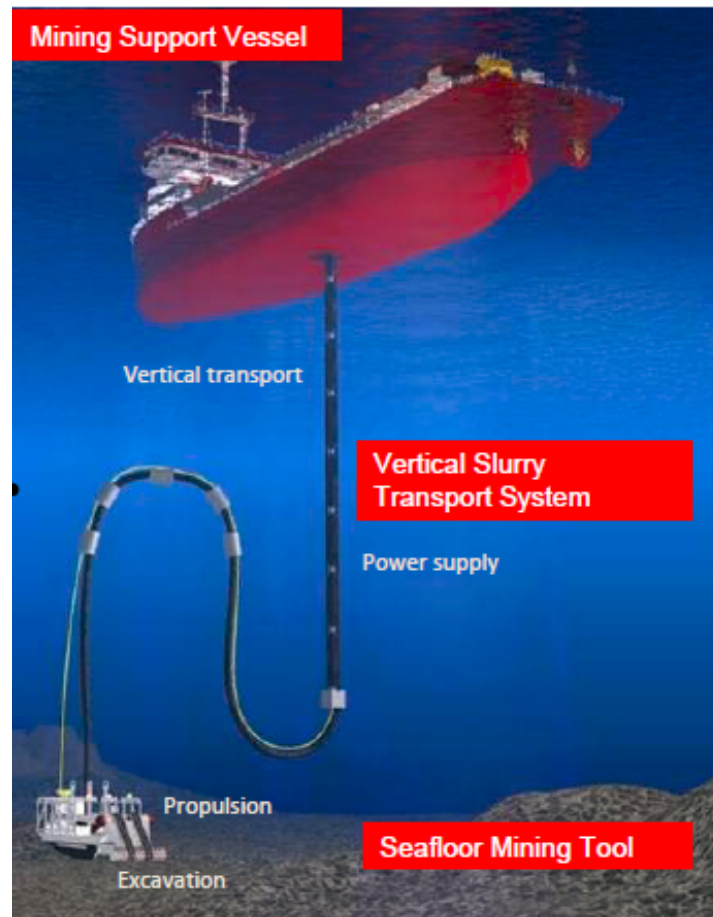
Figure 1.5: Overview of deep sea mining equipment

Source: *IHC Mining*

Of these processes, the first three are those which constitute the main technical challenge. To recover ore, two techniques can be used depending on what mineral deposit is being mined. Since SMS and CRC are bonded to their substrate rock and require breaking, these must be collected utilizing mechanical cutting or drilling which may be done through a drum cutter and a collecting machine is shown in Figure 1.6 (Nautilus, 2016)[1].

The polymetallic nodules, on the other hand, are not locked into a matrix, so there is no need to break rock during excavation. The excavation equipment is therefore often referred to as collectors and picks the polymetallic nodules from the sea bed. This may be done by means of a hydraulic or a mechanical collector. The mechanical system consists of moving parts that collects and transports the nodules into the riser system, usually, by means of a vibrating comb mechanism. Due to the great number of moving parts, a higher risk of breakdown exists; therefore, hydraulic collectors are preferred. Hydraulic collectors are crawlers equipped with aligned nozzles that produce a low pressure and a scouring action lifting the nodules from the seabed minimizing interaction between the collector and the seabed (Figure 1.7).

The preferred method to bring the ore to the surface depends on the complexity and depth of the deposits. Commonly hydraulic transport systems such as centrifugal pumps have been considered due to its reliability and high lifting capacity. The required systems already exist as the same hydraulic pumps have been applied in the dredging and the oil and gas industry.

Finally, similar to oil and gas or dredging, a production support vessel is present at the center of the mining operation. Its purpose is to supply a large deck space from which all mining operations such as seafloor mining tools, lifting pre-processing, storage and transfer of the ore.
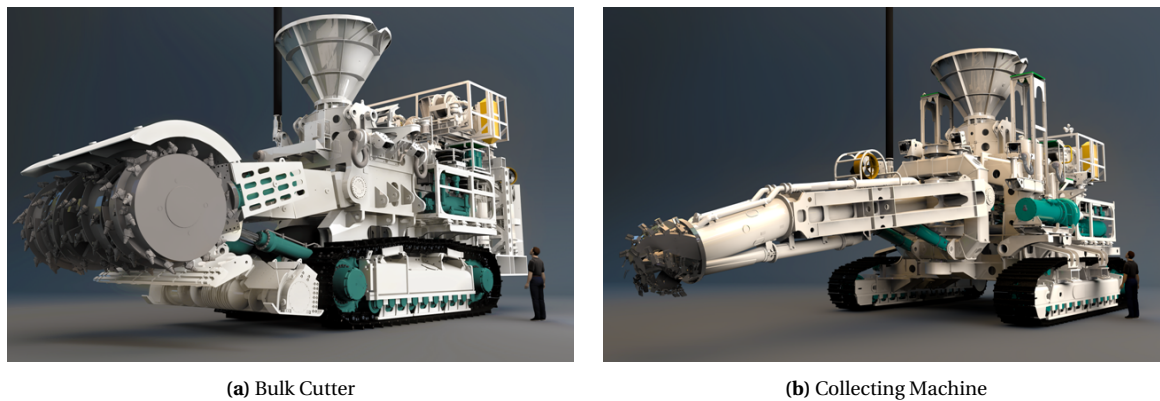
(a) Bulk Cutter   **(b)** Collecting Machine

Figure 1.6: Seafloor Production Tools

Source: *Nautilus Minerals*[1]
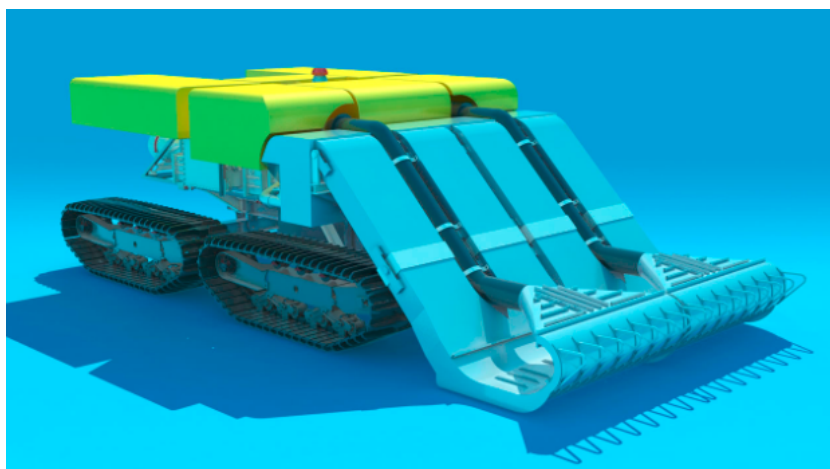
Figure 1.7: Polymetallic nodule collector

Source: *IHC Mining*

1.2.3. Environmental Impacts

Currently, the most significant setback towards exploitation licenses is not because of lack of technology but because of a lack of knowledge on deep-sea biodiversity and the impacts of mining on ecosystems. Many studies seem to indicate that deep-sea mining inevitably causes loss of biodiversity on a local scale (Van Dover et al., 2017)[58]. Given the prolonged natural rates of recovery of these ecosystems, damages may be considered to be irreversible in human time scales. This leads to an enormous amount of controversy towards the development of deep-sea mining projects due to possible irreparable damage that may occur to the environment and its ripple effect towards communities for many generations to come (Niner H. et al., 2018)[42].

The International Seabed Authority is currently drafting a regulatory framework for deep-sea mining that includes measures for environmental protection; however, new research and discoveries keep arriving which have hindered the development of a final regulation. Some of the main hazards that contribute to most of the environmental impact are listed below (Navarre et al., 2017)[39]:

- **Destruction of benthic organisms that inhabit the mining area:** Deep-sea mining will cause loss of biodiversity on a local scale, both directly and indirectly, during operations due to the vulnerability and low resilience to changes of the organisms in that environment.

- **Suspended sediment plumes on the seafloor:** Removing nodules and their associated sediments with seafloor production vehicles will create sediment-laden plumes on the ocean floor. These plumes are clouds of potentially toxic particles are likely to impact habitats well beyond the areas of mining leading to smothering of multiple benthic habitats.

- **Impact to species because of the noise, vibration, and light that is induced:** Deep-sea organisms habitats are dark and noiseless. Operations of the submerged remotely operated vehicles will disrupt this environment by increasing underwater ambient noise, generating vibrations on the seafloor and by implementing artificial lighting.

- **Water discharge after ore separation:** Sediment plumes can also occur near the surface, in the case of dispersion from the ship, or if the water is ejected near the surface after ore separation. In this case, particle clouds can reduce light and temperature and impact plankton growth, leading to possible repercussions for the entire food chain.

Recent research is focusing on determining not only environmental impacts but mitigation strategies as well. Most mitigation strategies focus on facilitating recolonization areas that have been impacted by mining as well as methods to reduce the effects of the sediment plumes produced during mining activities.

1.2.4. Existing Regulations

The ocean is carved up in different jurisdictions, and over 60% of the ocean falls into international waters or areas beyond national jurisdiction. To regulate mining activities, a constitutional document governing mineral exploitation was developed by the U.N. in the year 1982. The United Nations Convention on the Law of the Sea (UNCLOS) taken effect since 1994, and three sections are particularly relevant to deep-sea mining; Article 136, Article 137.2, and Article 145. These articles watch over the common heritage of humanity, the legal status of the areas and its resources and the protection of the marine environment respectively.

The UNCLOS also divides the sea into three distinct areas of commercial and international interest. The first 12 nautical miles (22 Km) from the coastline is described as the territorial sea. Within this area, the coastal state law is absolute except as restricted by UNCLOS and other international laws. Beyond this territorial sea is an area known as exclusive economic zone (EEZ) that stretches up to 200 nautical miles (370.4 Km). Within this area, the coastal state does not have absolute sovereignty but is granted with a limited set of rights related to its resources regarding activities of economic exploration and exploitation on both seabed and water column. Further out to sea, in international waters, is called the area beyond national jurisdiction (ABNJ) which is designated by UNCLOS as a common heritage of humanity. This final area is the jurisdiction of the International Seabed Authority (ISA).

The ISA is responsible for the regulation and the control of mineral-related activities in the international waters. Its main goals are to deliver licenses for exploration and exploitation in deep-sea mining, protect marine biodiversity by assessments of environmental impacts and collect and distribute royalties product of deep-sea mining. Currently, no legislation exists for exploitation, however, up to 26 exploration licenses have been granted. Implementing deep-water regulations is challenging given the currently minimal knowledge of this environment.
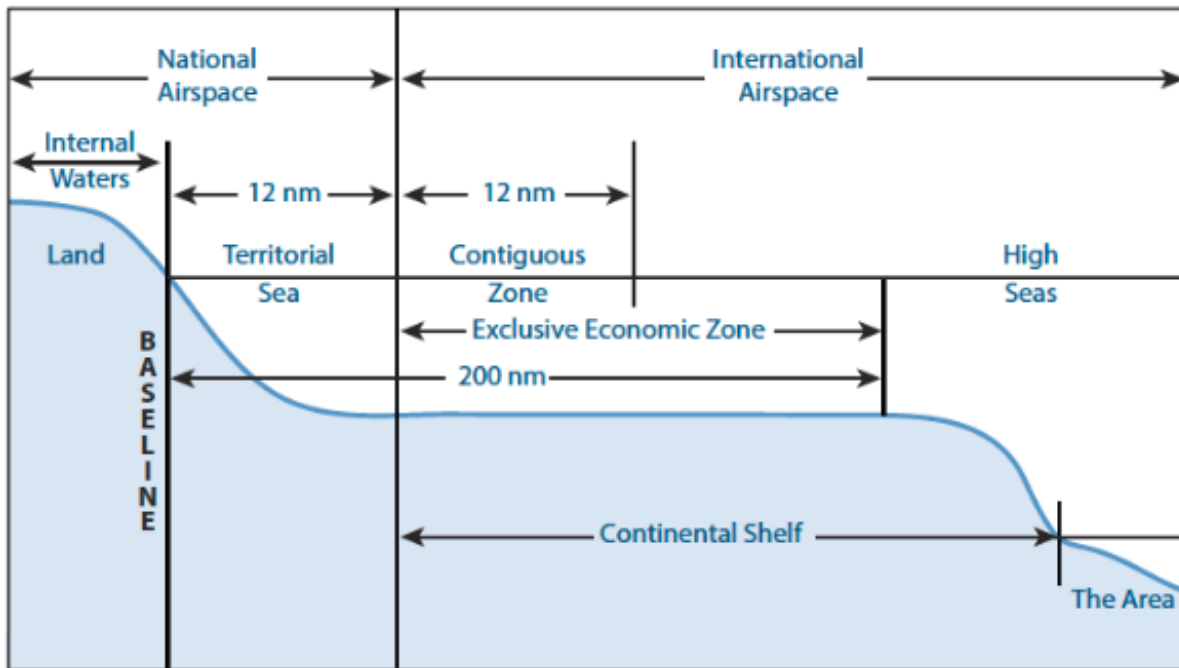
Figure 1.8: Maratime zones schematic

Source: *UNCLOS*[57]

1.3. Research Outcome

As previously mentioned, the environmental hazards in deep-sea mining remain the most significant obstacle towards deep-sea mining exploitation. Researchers of the Blue Mining Project, a European international consortium of 19 large industry and research organizations, agreed in their final report that the most significant concern towards environmentally friendly mining was to reduce the sediment plume that was generated during mining, particularly on the seabed (Blue Mining, 2018)[35].

Due to the lack of understanding of the environmental impacts, the industry is moving towards developing technological modifications that could be employed to lessen the effects of plumes by minimizing their size.

As part of the deep-sea mining operation, in which polymetallic nodules are mined from the sea bottom, waste streams are generated. One of the main flow of waste streams is the SWOE (Sediment Waste and Other Effluents), a product of the unavoidable sediment extraction during the subsea crawler's mining phase. All though a minor portion of the SWOE is produced after the mineral processing onboard the mining vessel, most of its solids is released at the subsea crawler prior to vertical transportation.

This research focuses on small scale sized laboratory experiments in which the crawler's outlet shape is varied, and its plume's effects of the SWOE are measured. Besides gaining insight in the horizontal plume spreading under different conditions and geometries, the outcome of the research is to provide a set of measurement data that can be used for future numerical model validation towards determining an optimal outlet shape for the seabed crawler in which the plume can visibly settle.

This research at TU Delft is in cooperation with IHC Mining and its involvement in the Blue Nodules, Blue Harvesting and JPI Oceans which aim to develop an innovative vehicle that enables mining while causing minimal environmental impact (IHC, 2019)[37]

1.4. Problem Identification

As previously mentioned, since the most recent discoveries of the rich benthic ecosystem on the deep ocean floor, concern has been expressed about the potential environmental impact due to the exploitation of deep-sea mineral deposits. To lessen environmental impacts into these environments, mitigation strategies that aim at reducing the size, concentration and toxicity of the sediment-laden plumes generated in mining are being investigated.

Currently, the ISA is working on drafting environmental regulations. This presents significant opportunities for research on careful deep-sea environmental studies and for the development of technologies that incurs in the least possible environmental impact. Since field data is scarce or non-existing, there exists a need to provide numerical models which allow evaluation and extrapolation to the dimensions to be expected in future commercial mining.

Numerical modeling is currently being applied to determine plume developments and seafloor blanketing caused by various sediment discharges in order to predict their environmental impact. However, the reliability of the present numerical models depends on experimental validation data produced throughout small scale experiments. Once sufficient data has been collected, numerical model calibration and validation is expected to take place in order to be able to optimize the sub-sea crawler outlet and reduce the plume generation to an absolute minimum.

1.5. Research Objective

The spreading distance of the plumes that are generated by the mining process and the cleaning of nodules is unknown. Over the last years, some numerical models have been developed for vertically negatively buoyant plumes which have been validated with experimental data (Grunsven F. 2018)[17], used mainly to test the determine the effectiveness of discharging the vertical discharge pipe in the proximity of the seabed. Horizontal negatively buoyant offset jets have also been vastly studied. Numerical models have been validated to determine concentration and velocity profiles mainly for brine diffusers and desalination purposes. (Shao D., 2010)[51]. However, as part of the design for the blue nodule seafloor collector of IHC Mining, accurate set of measurable data is required for in-house model verification. This allows for future modifications to mining equipment such as the diffusers or modifies mining procedures.

The main research objective of this master thesis is formulated as follows:

To provide on a small laboratory scale a validation data set for numerical models to predict plume development, sediment concentration and velocity profiles in the near field area for three different diffusers and to compare data to propose an optimal diffuser.

The research objective will be achieved by addressing the following research questions:

- How will the proposed diffuser designs alter the properties of the outlet flow?

- What are the near field outflow velocity and suspended sediment concentration profile for the three different diffusors through the plume's pathway?

- What are the influence of the diffuser's shape on the plume's length?

- What are the effects of modifying the plume's source concentration on the fully developed plume length?

To address the first question three different shapes of diffusers are proposed based on a basic diffuser design method that relates the geometry and inlet flow conditions of the diffusers to several standard geometries with defined inlet flow conditions. This is done to have appropriate flow distribution and to minimize energy losses. Subsequently, the most significant deliverable is the data set resulting from the measurements of velocity profiles and suspended sediment concentration that is to be used to compare and validate numerical models used to predict the plume environmental impact. This data set has been handed to Royal IHC - Mining at the end of this investigation. The final research questions focus on measurement and visualization of the recorded plumes for the different diffusers and initial concentrations to determine an area of impact.

1.6. Assumptions and Limitations

The main assumptions and limitations encountered during this research are as follows:

- In order to keep experiments within budget and schedule an existing setup is being used. These present limitations towards the scaling factors due to space considerations and the fully developed plume's expected length

- For the sake of repeatability and controlability the inlet flow and concentration are assumed to be constant during the experiments.

- The initial position of all diffusers is assumed to be the same without completely horizontal and without any angle deviations product of installation.

- For simplicity reasons, the material used for simulate the SWOE that will be encountered in the deep-sea environment will be round glass beads which do not posses any cohesion or flocculation.

- No external or environmental conditions are included in the experiments such as currents, density effects or relative velocity from the crawler.

1.7. Research Approach

The research of this master thesis can be divided into several steps. The first part comprises a literature review in which a description of deep-sea mining horizontal plume development and the diffuser geometry design are investigated. Next based on parameters that IHC Mining has supplied regarding inlet flow and concentrations, scaling factors are determined in order to prepare the experimental setup.

After the scaling factors have been determined an existing laboratory setup located in the dredging laboratory at the TU Delft is modified, and three different geometries of the outlet diffuser are constructed through 3D printing.

The following step is to carry out laboratory experiments under specific and scaled monitored scenarios. The experimental procedure is to discharge a sediment mixture through a centrifugal pump at a constant flow inside a water basin through the diffusers to generate a horizontal plume and obtain experimental data for all three different outlet geometries.

Finally, conclusions are drawn based on measurements and recorded visual data. This ultimately allows determining final recommendations towards the crawler outlet diffuser geometry that eventually leads to a plume reduction. Experiments are carried out in the Dredging Laboratory in TU Delft, while data analysis is carried out in IHC Mining in Kinderdijk.

1.8. Report Structure

The report structure is a description of the entire research project and can be described in the following chapters:

In Chapter 2 the theoretical framework is explained, including literature regarding horizontal negatively buoyant dense jets, free jets, offset jets and diffuser geometry selection methods.

Chapter 3 the experimental setup, procedure, calibration, and measuring techniques are described. All experiments that are performed are listed in this chapter as well.

In Chapter 4 summarizes the most important results such as velocity and concentration profiles as well as visual recordings of the plume development.

Chapter 5 provides data analysis, comparison with existing literature and discussion.

Finally, in Chapter 6, the conclusion and recommendations to reduce the generated plume based on experimental data are given.

2

Theoretical Framework

2.1. Overview

In environmental fluid mechanics it is quite common to find stagnant fluids being intruded by other fluids with a different density or carrying a concentrated material. Some examples of this include wastewater discharges into rivers, plumes exiting industrial smokestacks or in this specific case sediment-laden plumes generated from Sediment Waste and Other Effluents (SWOE).

In every case, a fluid with a certain amount of momentum and/or buoyancy exits a specific orifice and intrudes into a larger body that contains different characteristics such as velocity, temperature or density. Usually, these flows are characterized as turbulent because their intrusion creates situations of mixing and entrainment. The prediction of the path of mixing of these fluids is important for sound environmental control and impact assessment, therefore theories based on experiments and numerical modeling have been developed. The goal of this chapter is to give a theoretical background for physical processes that are expected to occur during experiments for turbulent jets and plumes with and without solid particles.

The first section focuses on the existing literature on the development of free turbulent jets. Existing theories of flow configuration, mixing, theoretical modeling have been presented as well as some relevant research that has proven useful for this investigation. The next section focuses on bounded jets. Bounded jets are comparable to the free turbulent jets, except that they have a strong interaction with a boundary layer. Bounded jets are expected to have physical processes similar to those found in the plume generated by the crawler outlet mostly, because of the plume's interaction with the seabed.

The third section of the literature review includes the expected particle sedimentation process and how it correlates to the physical length scales. It is determined that sedimentation depends mainly on the parameters of the particle-laden-jet such as the discharge velocity, concentration, flow velocity and mainly the particle properties such as density, shape and size. Finally, in order to reduce flow velocity and momentum fluxes aiming to reduce the particle-laden plume generated by the nodule collector, diffuser design theory is analyzed. Different existing flow regimes, as well as methods to improve performance in order to reduce flow separation, are included.

2.2. Free Turbulent Jets

Whenever a moving fluid enters a stagnant fluid body, a velocity shear layer is created between the entering and the ambient fluid which causes turbulence and mixing. Whenever this fluid is uninterrupted by any boundary conditions, it may be considered as a free turbulent jet. Free turbulent jets and plumes are phenomena that have been extensively investigated. Some of the most important literature regarding this subject was published by Morton et al. (1956)[38] Fischer et al. (1979)[16], and List (1982) [29].

These investigations report that free turbulent jets penetrating into a quiescent fluid of the same density usually adopts a conical shape and widens proportional to the distance downstream with an average angle from the point of origin. Observations also reveal that the velocity in the free jets obey a law of similarity in which all cross-sections exhibit a nearly Gaussian distributed shape relative to maximum velocity present in the centerline as shown in Figure 2.1.

When the jet contains a contaminant or a concentration of a material and the ambient fluid does not, entrainment causes dilution, and the concentration decreases downstream adopting a Gaussian distribution similar to the velocity profile where the maximum concentration is located along the centerline. Because of the dilution generated by the entrainment of ambient fluid, both velocity and concentration profiles diminish with distance from the discharge location.
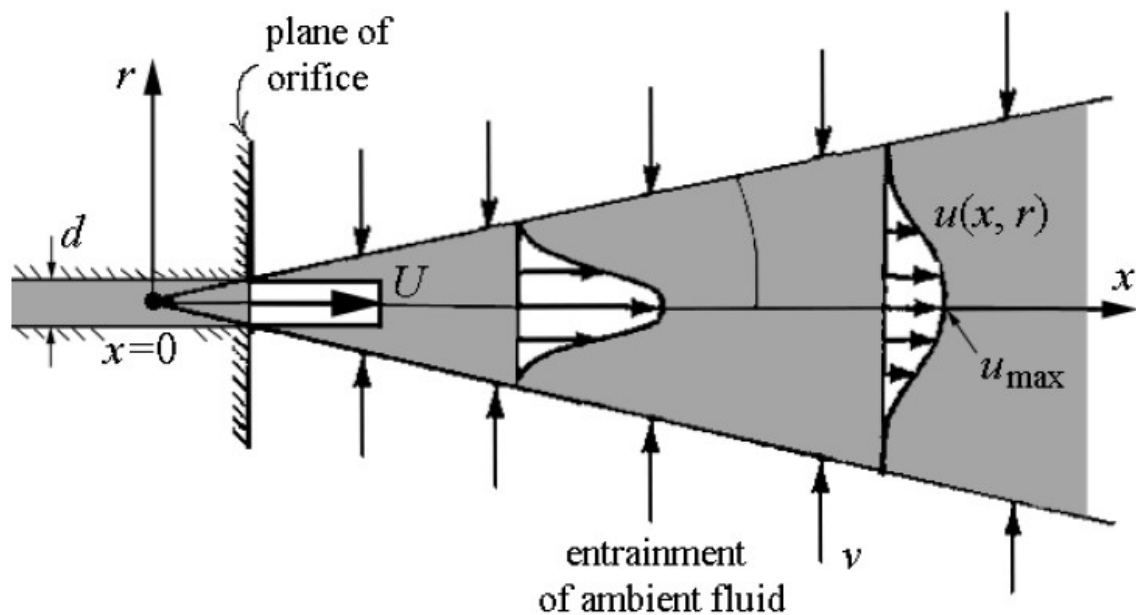
Figure 2.1: Schematic description of a jet penetrating in a fluid at rest

Source: *Cushman-Roisin, B. (2019)*[10]

2.2.1. Free Jet Flow Configurations

Turbulent free jets have three basic flow configurations in which it can be classified depending on the source of momentum and buoyancy present in the fluid. Jets can be briefly defined as the release of a fluid with a given velocity through an orifice in a field filled with a receiving fluid. Plumes are generated due to the release of potential energy that provides the fluids with positive or negative buoyancy. These two phenomena are seen as the limiting cases of a more common scenario where both momentum and buoyancy are present at the same time: this condition is referred to as a buoyant jet.

A typical buoyant jet has momentum dominated jet behavior near the source but basically becomes plume like behavior as the distance from the source increases. This is because the initial momentum gets diluted across the plume increasing size. The buoyant jet flow is fully turbulent whenever its efflux Reynolds number; based on efflux velocity, orifice dimension, and fluid kinematic viscosity, is sufficiently large. A negatively buoyant jet presents density larger than that of the receiving fluid and thus tends to sink.

Pure Jet

A simple jet flow has no buoyancy flux; this means that the density of the fluid in the jet and the ambient fluid are the same. The behavior of the jet is dominated by the initial momentum flux. This flux is conserved for a pure jet when discharged into an unlimited environment as no other forces are acting. The initial momentum flux is defined as:

$$M_o = Q_o U_o \tag{2.1}$$

where U_o is the initial (uniform) velocity of the flow, and Q_o is the discharge.

Time-averaged measurements on the concentration and velocity profiles show essentially a proper fit to a Gaussian distribution across the jet. The development of the jet can be determined by the width of its orifice (d_o) and the distance from the source (x) is divided into two zones; Zone of Flow Establishment (ZFE) and Zone of Established Flow (ZEF) as shown in Figure 2.2. The velocity and concentration in the potential core of the ZFE are constant. In the Zone of Established Flow (ZEF), $x > 5.2 d_o$, when the turbulence has penetrated to the centerline reducing the initial velocity and concentration but maintaining the Gaussian distributions. Any cross section can express the time-averaged velocity, or tracer distribution, in terms of a maximum value and a measure of the width.
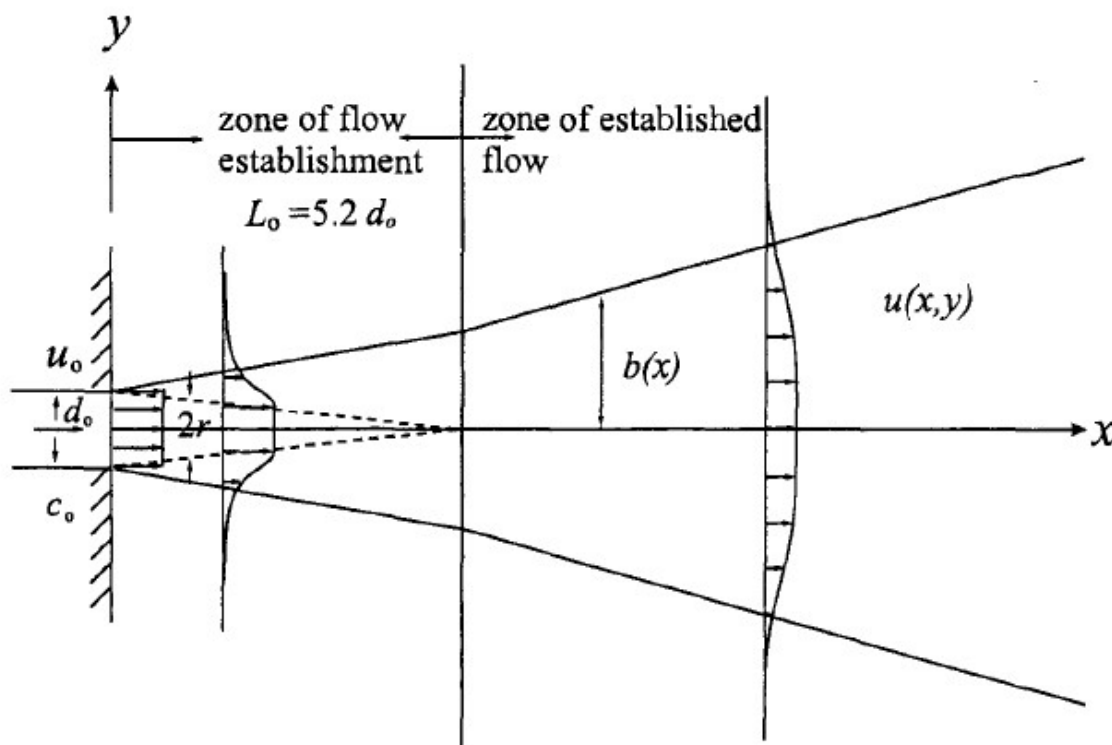
Figure 2.2: Turbulent slot jet showing the Zone of Flow Establishment (ZFE) and Zone of Established Flow (ZEF)

Source: *Chu and Lee (2003)*[27]

Pure Plume

Plumes are common features in environmental fluids, which occur whenever a persistent source of buoyancy creates a rising/lowering motion of a buoyant fluid upward/downward and away from the source. Pure plume flows into a still ambient fluid of different density where the velocity of the flow is almost negligible. Due to these density differences, gravitational potential energy is generated that drives a force to move the flow while the initial volume and momentum fluxes are assumed to be zero. These forces drive the convective mixing processes, where the discharged fluid moves through and entrains ambient fluid thereby diluting the discharged fluid.

For pure plumes, the discharge behavior is mostly dependent on the initial buoyancy flux B_o which can be found in Equation 2.2 and its distance from the source.

$$B_o = \hat{g}_o Q_o \tag{2.2}$$

The term $\hat{g}_o$ is referred to as reduced gravity and is used to describe the distribution of the force per unit mass of the fluid while the Q_o specifies the distribution of momentum per unit mass of the fluid. The term $\hat{g}_o$ is defined in Equation 2.3 where ρ_o is the initial density of the discharged fluid, ρ_a is the density of the ambient fluid, and g is the gravitational constant.

$$\hat{g}_o = \left(\frac{\rho_o - \rho_a}{\rho_a} \right) g \tag{2.3}$$

The mean cross-sectional concentration and velocity profiles of pure-plumes have also been shown to fit the Gaussian assumption (Lee and Chu 2003)[27].

Buoyant Jet

Buoyant jet motions (also called sometimes forced plumes) are prevalent in the natural environment and in engineering applications. In deep-sea mining, they may be observed through hydrothermal vent flows, vertical SWOE discharge through the fall pipe or in this specific case as horizontal sediment-laden plumes from a seafloor mining tool (SMT) or a crawler outlet.

A buoyant jet has jet-like characteristics depending on its initial volume and momentum fluxes and plume-like characteristics depending on its initial buoyancy flux. A buoyant jet is generated when relatively fast flowing fluid, is discharged in a reservoir of relatively slow flowing fluid from a continuous source and a density difference between the two fluids is present. The high-velocity gradients at the interface between the jet and the ambient fluid make it highly unstable and cause the jet fluid to separate the flow into eddies as described in Section 2.2.2 . These turbulent vortices entrain the ambient fluid into the jet, causing mixing processes and dissipation of energy from the discharge.

Dimensional analysis has been used to determine the approximate location of the transition between the jet-like region and the plume-like region based on specific length scales (Fischer et al 1979)[16] shown in Section 2.2.5. The mean velocity and concentration profiles of the buoyant jet are found to be similar to those of the jet and plume.

2.2.2. Entrainment

As previously mentioned, jets and plumes spread in a direction normal to the primary flow by the process of entrainment. During this process, ambient water gets enclosed by the jet fluid at its boundaries disperses the jet and increases its total mass. In order to ensure a constant momentum flux through every cross-section,

the jet velocity in turn decreases.

The first step of entrainment is known as the *induction* phase as defined by Sreenivas and Praasad (2000)[54]. During this phase, the induced fluid mixes with the turbulent fluid by the turbulent eddies shown in Figure 2.3. Afterward, *diastrophy* takes place were the induced fluid reduces its spatial scale until viscous diffusion becomes dominant. Finally, *infusion* occurs were mixing at a molecular level happens.
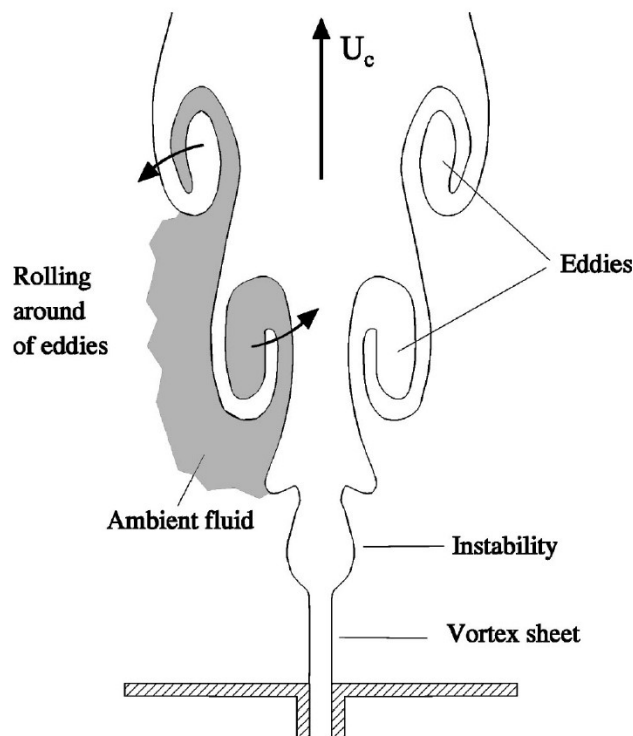
Figure 2.3: Entrainment process in axisymmetric jet in the near field. The shaded region indicates entrapped ambient fluid

Source: *Sreenivas and Praasad (2000)*[54]

The mean inward velocity at which the ambient fluid enters the jet boundary is known as the entrainment velocity. Assuming self-similarity Morton(1957)[38] and Fischer (1979)[16] proposed that the entrainment velocity was proportional to the local velocity scale using Equation 2.4

$$U_e = \alpha U_c \tag{2.4}$$

Where U_c is the time-averaged centerline velocity, α is the entrainment coefficient that relates the local velocity scale to the entrainment velocity U_e. The numerical value of α depends primarily on chosen length scales, local velocity profiles but primarily on the type of flow (jet/plume). Conventionally according to Turner (1986)[56], the radius at which the velocity reduces to $1/e$ (e = mathematical constant) of the center line value is chosen as the length scale revealing entrainment coefficients of the plume ($\alpha_p = 0.08$) to be greater than that of the jet ($\alpha_j = 0.05$). Hence the dilution rate in a plume is higher than in a jet for the same amount of momentum flux.

The entrainment hypothesis are well established and have been applied by many researchers. Without entrainment profile assumptions, additional closure equations would be needed to take the turbulent nature of the jets and plumes.

2.2.3. Governing Parameters

The turbulent jet behavior depends mainly on the three different kinds of parameters: jet parameters, environmental parameters, and geometrical parameters.

The jet parameters include factors such as velocity distribution, density, turbulence level, momentum flux and the flux of any jet tracer material such as contaminants or sediments. Environmental parameters include factors such as currents, density stratification, and turbulence levels. These factors usually influence jet behavior at a certain distance from the source. Finally, the geometrical parameters that enter into the jet analysis are the jet shape, orientation, and proximity to any possible adjacent boundaries.

2.2.4. Mixing Zones

An effluent discharging into a receiving body of water can be conceptualized as a mixing process that can be divided into an initial near field or jet dilution, and a subsequent far field dilution. The first region is close to the outfall structure and depends mostly on the outfall geometry, discharge velocity, and density differences. In the second region, which is known as the far-field region, the turbulent plume travels further away from the source mostly through currents, settling rates of particles, diffusive behavior or Coriolis effects.

Near field mixing is a complex process highly influenced by diffuser characteristics, discharge parameters, and ambient conditions. These properties make the near field process easier to control or modify through engineering measures. Some important diffuser characteristics are the port diameter and its closeness to boundaries, as well as its orientation to the ambient current. Flow field and mixing characteristics are dominated by small length and time scales (meters and minutes).

In the far field region, the plume trajectory and its mixing are mostly controlled by environmental conditions throughout passive diffusion and particle settling. Ambient conditions mostly control the trajectory throughout buoyant spreading motions due to density differences. Flow and mixing characteristics are dominated by large length and time scales (kilometers and days).

An illustration of turbulent jets mixing zones and their spatial areas is shown in Figure 2.4.
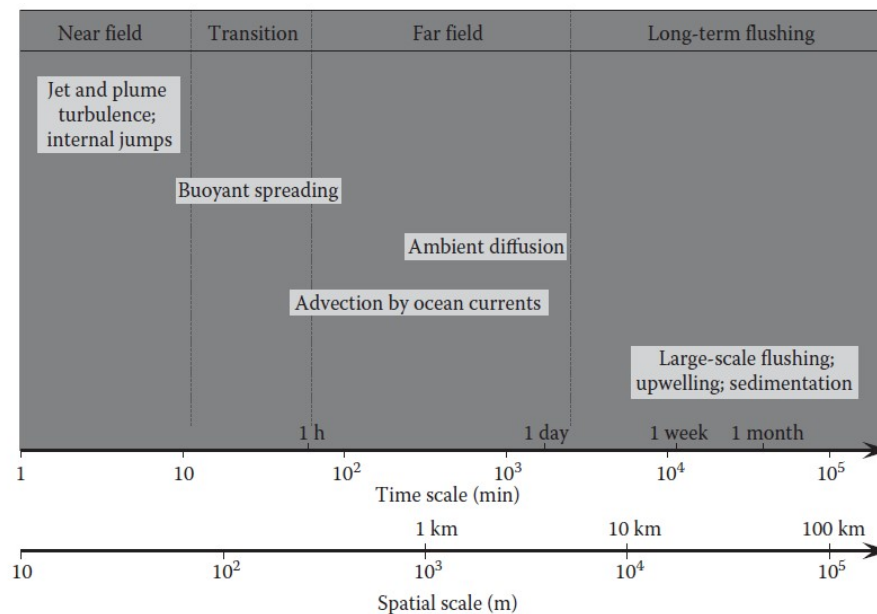
Figure 2.4: Main mixing zones and their approximate length and time scales

Source: *Roberts, J.W. (2013)*[49]

2.2.5. Modeling

For characterizing and modeling of the behavior of dense jets, experimental and numerical approaches are usually followed. Modeling of dense jets have mostly been done for brine discharges on desalination plants where the governing equations are the continuity equations, the momentum conservation equations, a transport equation and an equation of state.

For modeling of dense jets, simplifying assumptions are applied such as the Boussinesq approximation in order to neglect small density differences, water is assumed to be an incompressible fluid, hence the density of water does not depend on pressure or depth in the water column and Reynolds decomposition for separation of time-averaged and turbulent components. Closure models based on entrainment parameters are used as well.

Once the simplification assumptions and hypotheses have been formulated, the resulting equations are solved following three different approaches, namely by using dimensional analysis, by integration of ordinary differential equations, and numerically, with fewer assumptions, thanks to CFD models (Palomar et al. 2012)[43].

Dimensional Analysis

Dimensional analysis is used to formulate a reasonable hypothesis about complex physical situations that have been tested experimentally. In dimensional analysis, only the variables with a greater influence on the process are considered with the other values held constant. These variables are related through the discharges of mass (Q_o), momentum (M_o) and buoyancy (B_o) of the flow shown in Equations 2.5, 2.6 and 2.7 (Fischer et al. 1979)[16].

$$\rho Q = \int_A \rho u \, dA \tag{2.5}$$

$$\rho M = \int_A \rho u^2 \, dA \tag{2.6}$$

$$\rho B = \int_A \rho u \hat{g} \, dA \tag{2.7}$$

These fluxes are used to determine specific length scales that are used to characterize the effluent behavior. The main length scales for a round buoyant jet in a stagnant environment are shown in Equations 2.8 and 2.9:

$$L_q = \frac{Q}{M^{1/2}} \tag{2.8}$$

$$L_m = \frac{M^{3/4}}{B^{1/2}} \tag{2.9}$$

Equation 2.8 shows the flux-momentum length scale (L_q) which is proportional to the jet diameter and is close to the jet orifice. For values of z in the streamwise direction of $x/L_q < 1$, the initial geometry has an important effect on the flow, while for length scales of $x/L_q > 1$, the flow is dominated by the momentum close to the source and buoyancy at a larger distance.

Equation 2.9 shows the Momentum-Buoyancy length scale (L_m) which defines the relative importance of initial momentum and buoyancy fluxes. The flow dependent on this length scale determines how far downstream a transition from jet to plume behavior occurs. For values of $x/L_m <1$ a jet-like behavior may be expected while values for $x/L_m >1$ a plume-like behavior is foreseen.

A similar Momentum-Buoyancy length scale for that of round buoyant jet can be found on a two-dimensional slot in Equation 2.10 (Lee and Chu, 2003)[27]. This condition is the most relevant to our specific scenario.

$$L_m(2D) = \frac{M}{(B)^{2/3}} \tag{2.10}$$

Dimensional analysis has been used by various authors to calibrate different formulas based on experimental data or conventional optical measuring techniques. Another governing buoyant jet parameter is the densimetric jet Froude number, which can be used to determine the Momentum-Buoyancy length scale as well. The initial densimetric Froude number is a dimensionless number that determines the relative importance of inertial and gravitational forces at the source and can be defined in Equation 2.11.

$$F_r = \frac{U_o}{\sqrt{\hat{g}d}} \tag{2.11}$$

Integral Models

Integral models are a mathematical representation of mean flow behavior. The governing equations are integrated over the cross-section transforming them into simple differential equations which are commonly solved by Lagrangian or Eulerian methods. These integrations do not include boundary effects so the results are only valid prior to the impact of the jet in the bottom.

The results of the calculated equations refer to magnitudes on the jet axis, therefore in order to determine values for the cross section an assuming distribution function, generally a Gaussian or a Top-Hat distribution are required. Also, diffusion of the plume is modeled by entrainment formulas determined by experimentally. As mentioned previously, for axisymmetric negatively buoyant profiles, Chu and Lee (2003)[27] defined the development of the jet different for the Zone of Flow Establishment (ZFE) and the Zone of Established Flow (ZEF).

The velocity and concentration in the potential core of the ZFE are constant while surrounding the potential core there is a mixing layer. Velocity and concentration values are given by Equation 2.12.

$$U(x,y) = U_o exp\left(-\frac{(y-r)^2}{b_w^2}\right) \tag{2.12}$$

$$C(x,y) = C_o exp\left(-\frac{(y-r)^2}{\lambda^2 b_w^2}\right) \tag{2.13}$$

As shown in Figure 2.2 the length of the ZFE is of 5.2 do after which the ZEF begins. In this layer, the turbulence has penetrated the centerline through entrainment and the velocity and concentration profiles can be well approximated by Gaussian distribution in Equations 2.14 and 2.15.

$$U(x,y) = U_m(x) exp\left(-\left(\frac{y}{b_w}\right)^2\right) \tag{2.14}$$

$$C(x,y) = C_m(x) exp\left(-\left(\frac{y}{\lambda b_w}\right)^2\right) \tag{2.15}$$

Where (x, y) are the streamwise and radial coordinates and r is the half-width of the potential core. The centerline maximum values of the profile are given by $u_m(x)$ for velocity and $c_m(x)$ for concentration shown in Equation 2.16 and 2.17 respectively.

The parameter λ is introduced to account for mass and momentum diffusion and b_w is the width of the mixing layer, defined as the lateral location where the velocity is equal to $1/e$ of the centerline value. Values of λ and of the spreading coefficient β are determined experimentally in different papers for both slot and round jets (Brooks, 1972[5], and Papanicolau and List 1988[44]). Studies have shown that the jet properties such as jet trajectory, centreline velocity, jet width and dilution predicted by the integral model agree well with experimental and field observations.

Adopting values for β as 0.12 and λ as 1.35 the maximum centerline velocity and concentration solution for plane jets can be summarized in Equation 2.16 and 2.17 according to Chu and Lee (2003)[27].

$$\frac{U_m}{U_0} = 2.58\left(\frac{x}{D_0}\right)^{-1/2} \tag{2.16}$$

$$\frac{C_m}{C_0} = 2.27\left(\frac{x}{D_0}\right)^{-1/2} \tag{2.17}$$

Computational Fluid Dynamics Modeling (CFD)

The governing equations for fluid flow can be numerically solved by Computational Fluid Dynamics (CFD) modeling as an alternative to integral modeling however it has proven to have higher processing time and computational costs. CFD models use more complex turbulence model to correlate the turbulent transport term to the gradient of mean flow quantities, such as $k - \omega$ model or $k - \epsilon$ model and are more rigorous since they have fewer assumptions solving the complete Reynolds-Averaged Navier-Stokes equations (RANS). Very refined information can be extracted for these simulations, however, due to high Reynolds numbers present in jets, these models become high time-consuming compared to traditional integral models.

2.2.6. Relevant Studies

There are a vast amount of laboratory experiments and investigations carried out on simple momentum jets. One of the most significant was carried by Albertson et al. (1950)[2], wherewith experimental results, velocity profiles for jets were demonstrated to be self-similar and held a Gaussian distribution after the zone of flow establishment.

Morton et al. (1956)[38] introduced the idea that fluid momentum, vorticity, and scalars in a jet are spread by turbulent entrainment rather than turbulent diffusion. They hypothesized that non-turbulent, irrotational fluid from outside the jet was entrained into the turbulent jet and that way the jet was increased in size.

The first to incorporate the entrainment approach into a general jet model was Fan (1969)[15]. He used a Eulerian integral method, in which the flow passes through a fixed control volume, and integrated the equations of motion over that control volume. Jirka (2004)[24] developed an integral model for the prediction of jet effluxes into ambient fluid environment years later that used the entrainment approach as well validated by experimental data.

Brooks (1972)[5] and Papanicolaou List (1988)[44] amongst others, investigated the velocity and concentration decay of round and slot turbulent buoyant jets. Values for mean and turbulent properties were reported for velocity and dilution with different environments based on collected experimental data.

Fischer et al. (1979)[16] defined main parameters that influenced the jet behavior and brought together experimental data of various research to perform a dimensional analysis for jets, plumes, and buoyant jets. Lee and Chu (2003)[27] gathered data from many types of research and gave comprehensive descriptions of jets and plumes alongside semi-empirical formulas to determine fluxes along the path of the plume. A consistent and unified development of a Lagrangian approach for prediction of free jets and plumes, including effects of crossflow and ambient density stratification was developed.

In recent years the study of buoyant jets has been greatly enhanced by novel experimental techniques, especially field-based methods such as particle-image velocimetry (PIV) and laser-induced fluorescence (LIF), that provide valuable structural insight into the buoyant jet mixing and entrainment processes as well as more reliable data for model testing and evaluation. Most of these experimental techniques have been used to determine jet behavior in inclined angles for desalination plants for brine discharges such as Crowe (2013)[9] and Shao (2009)[51].

2.3. Bounded Turbulent Jets

Considering that jets are commonly discharged into a stagnant, but not unlimited environment, close attention has to be made towards jets that are in the vicinity to the bottom or the surface of the environment which are considered as bounded jets.

As previously mentioned fluid jets may be considered either as free jets as discussed in Section 2.2 or they may be considered as bounded jets. This depends on the distance of the discharge point to confining boundaries. If the distance from the orifice is large enough, then the jet is to behave as a free jet and all the free turbulent jet flow characteristics apply. Bounded jets arise in various practical applications such as environmental dischargers or fluid injection systems. They are classified in three different types:

- Impinging Jet

- Wall Jet

- Offset Jet

The main focus of this investigation is directed towards offset jets since this condition is what is expected to occur in the near bottom discharge of the crawler outlet.

2.3.1. Offset Jets Flow Configuration

Offset jets are formed when a jet discharges into a medium above a parallel boundary by a specific height thus having an influence on the development of the flow. Therefore offset jets can be considered as an intermediate case between a free jet and a wall jet. The flow is characterized by a longitudinal variation of curvature, skewed impingement onto a flat surface, a recirculating region, and the development of a wall jet region as observed in Figure 2.6.

The proximity of a solid boundary for a two-dimensional offset jet significantly affects the jet characteristics. Reduced entrainment from the boundary side of the jet results in a low pressure between the jet and the boundary causing the jet to bend towards the boundary and eventually be attached to it (Hoch and Jiji, 1981)[23].

The offset jet behaves differently in various regions. In the near field close to the discharge point the jet is a momentum-dominated flow having the properties of a free jet. After impingement occurs, the flow tends to move along the boundary with characteristics similar to an impinging jet. This results in a formation of a high-pressure gradient that later accelerates and drives the flow establishing a wall jet condition. The thickness of the wall jet region increases due to the presence of solid boundary and turbulent diffusion but its velocities undergo a decaying process.
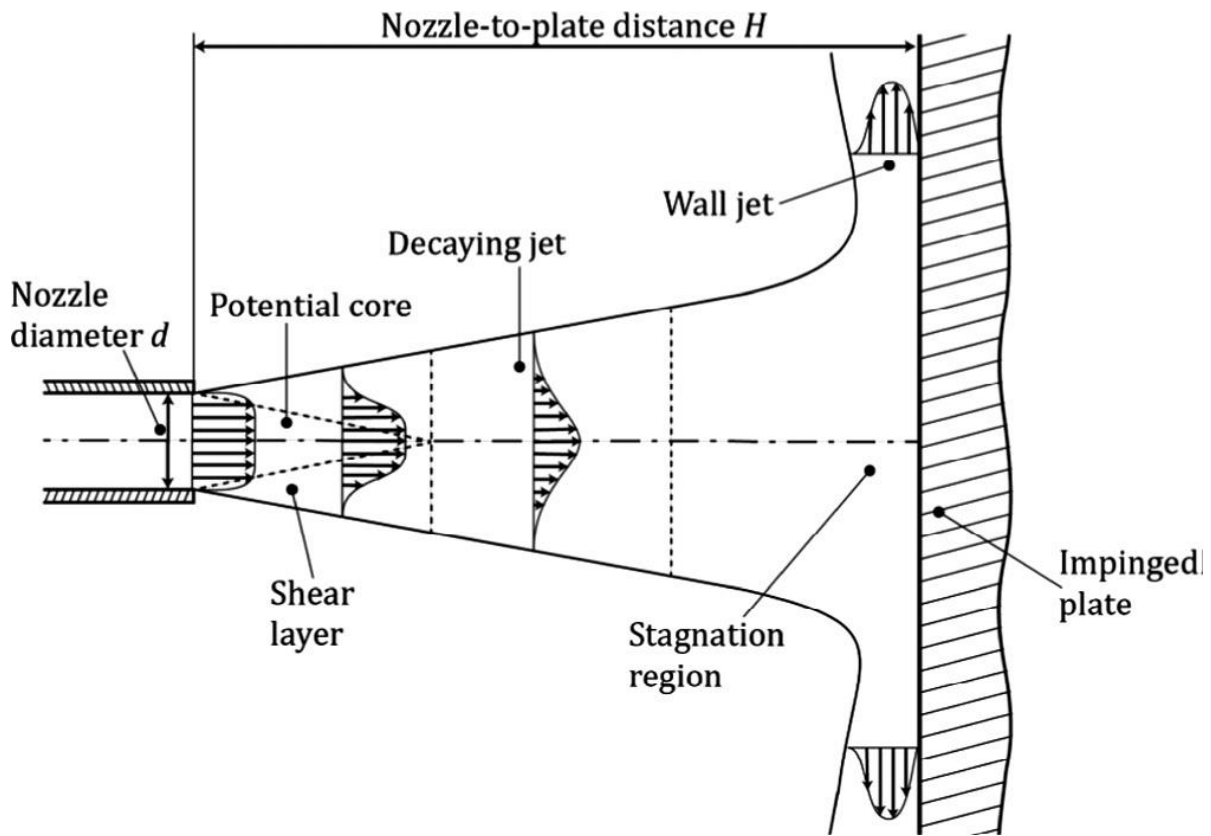
Figure 2.5: Flow characteristics of impinging and wall jets

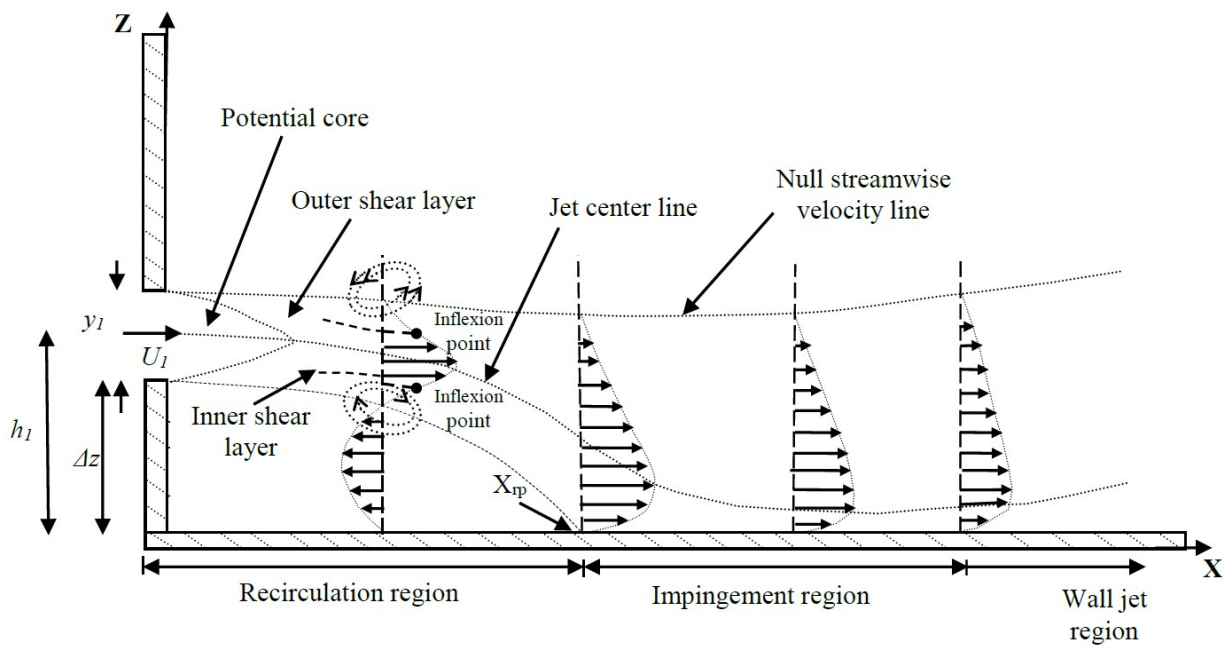**Source:** *G.M. Carlomagno and A. Ianiro (2014)*[7]

Figure 2.6: Flow characteristics of offset jets

Source: *Kishore et al. (2016)*[25]

Other factors such as stratification, ambient motion, density difference, discharge orientation, and three-dimensional (3D) effects may further complicate the jet-boundary interaction and behavior of an offset jet.

2.3.2. Coanda Effect

The portion of the offset jet flow before the reattachment location, termed recirculation region, possesses a negative gauge pressure due to entrainment of the ambient fluid in the presence of the bottom wall.

Following Bernoulli's principle, a pressure difference across the jet flow is developed, which acts on top of the negative buoyancy to deflect the jet towards the boundary. This phenomenon that acts as an external force deflecting the flow towards the boundary is known as the Coanda effect.

Experimental investigation on the effect of the Coanda attachment related to a horizontal dense jet discharge have been conducted in several studies (Sobey et al, 1988[53]; Shao et al, 2011[52]) where two-dimensional parameters to account for the boundary constraints were introduced; the free surface proximity parameter $(H - z_o)/L_m$ and the bed proximity parameter z_o/L_m where H is the water depth, z_o is the offset height and L_m is the momentum-buoyancy length scale. These studies suggest that a complete Coanda attachment does not occur under a bed proximity parameter of 0.1-0.15.

2.3.3. Relevant Studies

Bourque and Newman (1960)[4] were among the first to investigate the velocity and pressure behavior of a two-dimensional jet discharging with the effect of a solid boundary. However, the problem was greatly simplified by assuming that the presence of the boundary has no effect on the velocity distribution of the jet and using a velocity field similar to that of a free turbulent jet.

Rajaratnam and Subramanya (1968)[46] experimentally investigated the velocity and pressure fields of a two-dimensional jet initially offset from a parallel surface. The transition from a free jet towards the wall jet region was the investigation main focus. In addition, the characteristics of plane offset jets have been experimentally and theoretically studied by Sawyer (1960)[50], Pelfery and Liburdy (1986)[45], Yoon et al (1993)[60] and Dey et al (2017)[12]

An integral analysis based on an entrainment model was presented by Hoch and Jiji (1981)[23] to predict the jet trajectory, the reattachment length, and the maximum axial velocity decay. However, the integral model needs assumptions of appropriate velocity profiles and an empirical entrainment coefficient. Gu (1996)[18], presented a turbulent plane offset 2D model by solving the Navier-Stokes equations along with a $k - \epsilon$ turbulence model. With this method, pressure, velocity, and entrainment were obtained as part of the solution. Both of these models have been validated with experimental data of nonbuoyant offset jets only.

There are very few studies on the mixing of three-dimensional horizontal negatively buoyant jets near a parallel boundary reported in the literature as far as the author is aware.

2.4. Sediment-Laden Plumes

As previously mentioned, the environmental impact of polymetallic nodule harvesting is expected to be attributed to the sediment plume that is expected to be generated. Therefore the prediction of the deposition pattern is of importance if effective measures are to be taken to minimize the impact of the fall-out material. The difficulty of analyzing particle-laden-jets lies in the complex changes of transport mechanisms in the jet as the carrier medium of the suspended particles which tend to settle out if the flow field changes.

A conceptual model of the structure of a horizontal sediment-laden momentum jet with dilute concentration is shown in Figure 2.7. The horizontal laden jet with a source diameter D and initial flow velocity U_o mixes with ambient fluid by shear-induced turbulent entrainment. Sediment particles with source concentration C_o and still-water settling velocity ω_s are transported in the horizontal direction and dispersed by turbu-

lent mixing. As the flow velocity and turbulence intensity reduce, particles fall to the bottom under gravity, forming a deposition profile with a peak close to the jet nozzle and an elongated tail. The overall jet mixing characteristics can be shown to depend on the integral jet volume and momentum fluxes Q_o and M_o and the characteristic sediment settling velocity ω_s. This however, does not consider the sediment being carried by density currents after impingement.
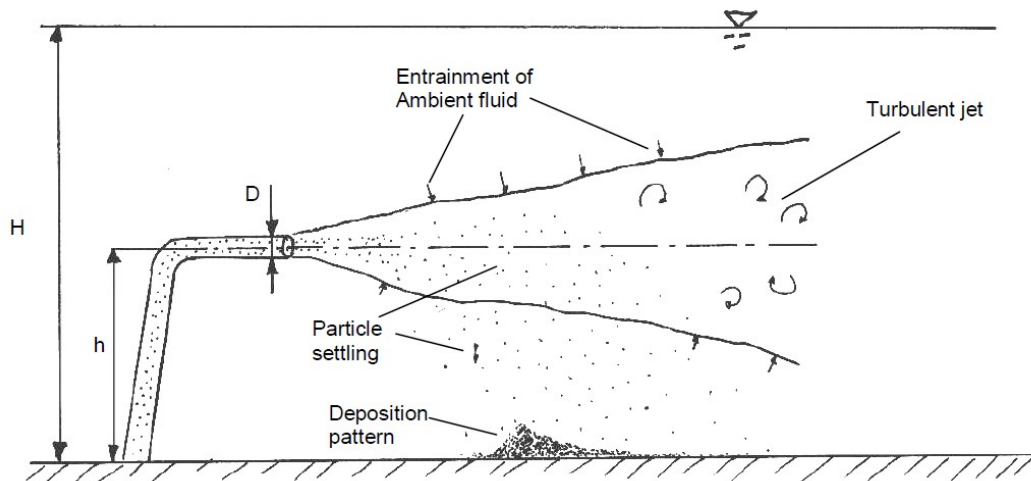
Figure 2.7: Diagram of a horizontal jet discharge of a sediment ladden plume into a stagnant environment

Source: *T. Bleninger (2000)*[3]

2.4.1. Settling Velocity

The settling velocity (or terminal velocity) of particles is one of the key variables in the study of any type of flow involved in transport or sedimentation. Particle settling velocity in a stagnant fluid is determined by particle geometry, specific density, and fluid viscosity.

The settling velocity of a spherical particle in a fluid at rest can be determined by solving a balance between a gravitational force and the drag resistance. By rearranging these terms, the settling velocity (ω_s) may be determined for small particles ($d_{50} < 100\mu m$) by Equation 2.18 (Van Rhee, 2002)[48].

$$\omega_s = \sqrt{\frac{4(s-1)g d_{50}}{3C_D}} \tag{2.18}$$

Equation 2.18 depends on a drag Coefficient C_D which may vary depending on the particle Reynolds number. The particle Reynolds number is calculated in Equation 2.20 and is usually low for small particles. When the Re_p is below 1, the flow is considered in a laminar regime and C_D may be calculated by the equations below:

$$C_D = f(Re_p) = \frac{24}{Re_p} \text{ (Laminar regime)} \tag{2.19}$$

$$Re_p = f(Re_p) = \frac{d_{50}\omega_s}{\nu} \tag{2.20}$$

where s is the specific gravity of the particle given; d_{50} is particle diameter, g the gravitational acceleration. Shown in Equation 2.19 is the drag coefficient which is a function of particle Reynolds number and v is the kinematic viscosity of the fluid.

The particle motions in turbulent jet-flows are difficult to define. Therefore the rigorous assumption of a terminal settling velocity independent of the velocity fluctuations to ω_s is used. For the laminar regime, the relation for the drag coefficient can be substituted into Equation 2.18 yielding Equation 2.21 which is the Stokes equation for settling velocity.

$$\omega_s = \frac{\Delta g d_{50}^2}{(18v)} \tag{2.21}$$

2.4.2. Horizontal Jet Settling

Integral models and dimensional analysis have been proposed to determine particle sedimentation in sediment-laden jets. Integral models have been proposed by authors such as Lane-Serff et al. (2005)[26] and Lee et al. (2013)[28] where they take into account a simple entrainment assumption to describe the spreading of the plume and the resulting deposition profile. The sediment is assumed to first fallout from the jet where its settling velocity exceeds the inflowing entrainment velocity. The jet velocity decreases quickly downstream, inversely proportional to the downstream distance.

Dimensional analysis has also been used quite frequently in research of horizontal sediment-laden jets to reduce the number of interacting quantities to a number of appearing principle dimensions. For a horizontal sediment-laden jet, a characteristic length scale called momentum-settling length scale was introduced (Neves, 2002)[40].

2.4.3. Dimensional Analysis

As previously mentioned, the sediment jet can be characterized by a sedimentation length scale l_m defined by the jet momentum flux and particle settling velocity shown in Equation 2.22.

$$l_m = \frac{M^{2/3}}{(\omega_s)} \tag{2.22}$$

This length scale plays an important role in the analysis of the sedimentation spatial variation. The horizontal distance when particle fallout first occurs can be linearly correlated to l_m. A larger value of l_m suggests that the particle is light or the initial momentum is relatively large, therefore it reaches the floor at a larger distance from the jet origin. On the other hand, a smaller l_m indicates that the particle settling velocity dominates over jet momentum and due to gravity the particle will settle out of the jet rapidly.

According to experiments realized by Lee et al. (2013)[28], the particle concentration contours may be divided into three regions. For $x < 0.5l_m$, the upper half the sediment jet behaves like a pure jet with concentric contours. For $0.5l_m < x < l_m$, the sediment cloud starts to depart from the water jet and for $x > l_m$ the particle jet is separated significantly from the water jet. Also, a longitudinal bottom deposition rate F_s (g/m/s) has been determined based on the characteristic length scale. According to Lee et al. (2013)[28], the sediment starts to fall out of the jet at approximately $x/l_m \approx 0.2 - 0.3$, the peak deposition rate at approximately $x = 0.93l_m$ and at $x = 2.4l_m$ over 90% of the sediment input mass has settled as shown in Figure 2.8.
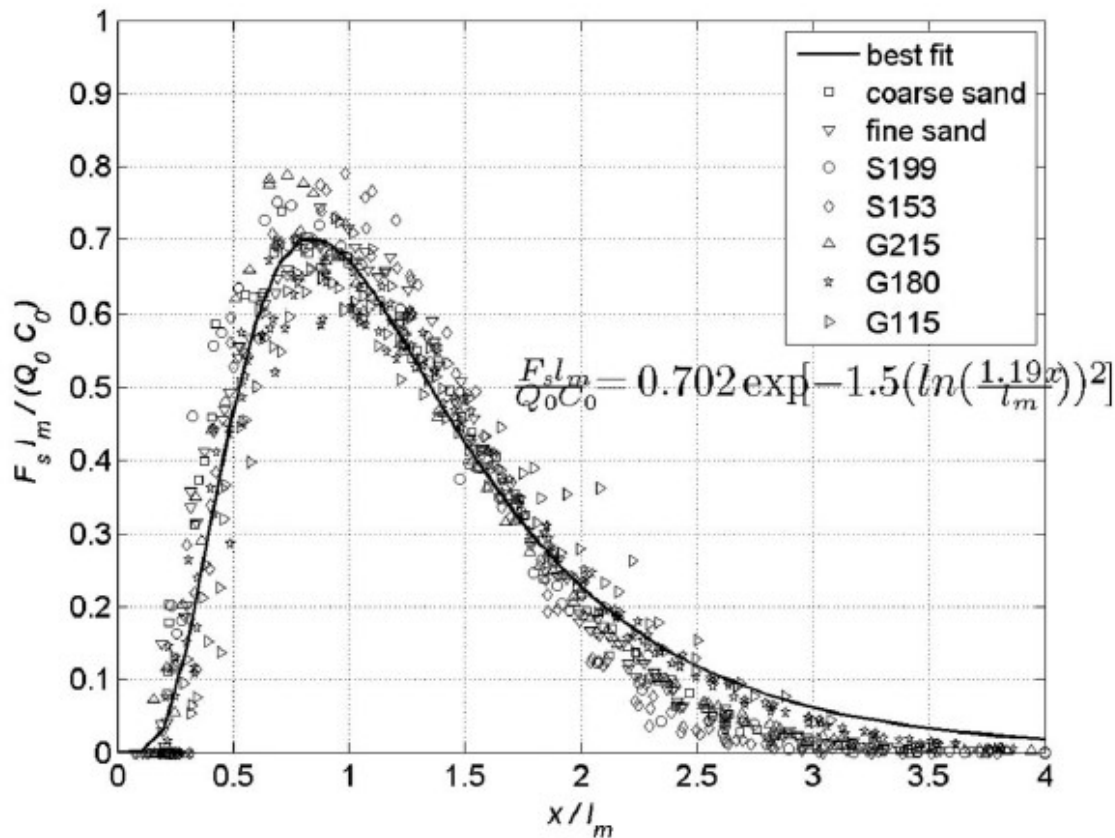
Figure 2.8: Normalized measured longitudinal bottom deposition rate as a function of x/l_m

Source: *Lee et al. (2013)[28]*

2.4.4. Relevant Studies

Studies on vertical sediment-laden jet have been a good start towards the comprehension of sediment plume behavior in general mostly because of the self-similarity properties expected fluids and sediment distributions. In vertical jets, the sediment velocity can be taken as the sum of fluid velocity and the settling velocity. For a sediment-laden jet discharging in a horizontal direction, the effects of particle-flow interactions are harder to analyze and have a larger impact because particle falling out occurs and the mean flow is not expected to be asymmetrical. Studies also take into account the effect of re-entrainment of particles from the environment into the plume and how the entrainment velocity influences the deposition of particles.

Neves and Fernando (1995)[41] conducted experiments on particle-laden jets discharging the jet effluent in a vertical direction and applying dimensional analysis to determine deposition patterns based on the jet strength and particle settling velocity.

Ernst (1996)[14] developed an integral model for particle sedimentation for a vertical up-ward turbulent buoyant plume assuming the mass of fluid on each particle decreased exponentially with time and stating that sediment deposition decreases linearly with a distance r for momentum jet and should decrease with $r^{1/3}$ for a buoyant plume.

Small scale experiments for horizontal sediment-laden plumes were conducted by Bleninger et al. (2000)[3] and Neves et al. (2002)[40] where the sediment deposition was found to be log-normal distributed. These experiments were coupled with dimensional analysis to determine the deposition rate of small particles based on a momentum-settling length scale

Cuthbertson et al. (2008)[11] and Liu et al. (2012)[30] demonstrated experimentally and through numerical analysis that for initial sediment concentrations below 0.1% no significant changes to the properties of the jet flow are noticeable. For jets with higher initial sediment concentrations, the settling of particles is observed to drag the jet with a downward bending trajectory.

Lee et al. (2013)[28] carried out experimental and theoretical research to determine bottom deposition measurements for particles of different size. The sediment jet was characterized by the momentum-settling length scale and a deposition semiempirical formula was derived based on a log-normal distribution. Experiments were compared to a calibrated two-layer Lagrangian model with excellent agreement.

Chan et al. (2014)[8] determined by CFD calculations that there were settling velocity fluctuations due to turbulent effects that have been neglected previously. The solid particles in the jet not only tend to settle by gravitational force, but can be maintained in the main stream by the turbulence in the jet. It was found that this can account for a significant reduction up to 30% in the settling velocity to determine the proper sedimentation profiles.

2.5. Diffusers

In most cases of engineering that involve the motions of fluids, a need to decelerate a flow often arises. A diffuser is an expansion or area increase intended to reduce velocity in order to recover the pressure head of the flow. In a deep sea mining nodule collector, a diffuser is expected to reduce the outlet flow velocity, in turn, reducing its momentum and eventually leading to a reduction of the plume.

Diffusers come in different types of shapes and forms that influence their final performance, however, the flow phenomena encountered in the diffusers are qualitatively similar. Their performance is often coupled with knowledge of the existing flow conditions, and a good performance is critical to avoid problems downstream on processes that require uniform and low velocity flows or rapid pressure recovery.

According to Miller[34], diffuser performance is interrelated with that of turbo-machinery, leading to the use of efficiency, η, as a performance parameter. Efficiency is defined as:

$$\eta = \frac{\text{Actual static pressure recovery}}{\text{Ideal static pressure recovery}} \tag{2.23}$$

The basic output of a diffuser is the pressure-recovery coefficient C_p, which is defined in Equation 2.24 by:

$$C_p = \frac{p_e - p_i}{p_o - p_t} \tag{2.24}$$

where subscripts P_e stands for the pressure at the exit, P_i is the pressure at the inlet and P_o is the stagnation pressure the fluid would achieve if the fluid were slowed to rest without pressure losses. A higher C_p is related to better performance.

By substituting the Bernoulli equation and the continuity equation, the frictionless pressure recovery coefficient may be presented in terms of the area ratio ($AR = A2/A1$) shown in Equation 2.25.

$$C_{p,\text{ frictionless}} = 1 - (AR)^2 \tag{2.25}$$

Therefore it can be concluded that performance of diffusers depend on the total divergence angle of the diffusers and the wall-length to throat-width ratio. Diffuser performance is often related as well to is loss co-efficient (K_d) which is shown below:

$$K_d = 1 - C_p \tag{2.26}$$

2.5.1. Pressure Losses in Diffusers

Velocity pressure conversion into static pressure usually requires significant energy dissipation due to the non-uniformity of velocity in parallel flow against the uniformity of the static pressure. When fluid enters a region of rising static pressure its energy has to be supplied from a higher energy fluid away from the walls or it will come to a rest (White, 2008)[59]. If part of the flow is brought to rest, the flow is said to have stalled or separated from the boundary.

When separation takes place the main flow usually contracts for some distance downstream of the separation point and an area of reverse flow forms. Following separation, large scale mixing spreads through the main flow, evening out the energy distribution at the expense of a drop in total pressure as shown in Figure 2.9. If the divergence of a diffuser is too rapid, then larger scale separation and stall may occur, causing low-pressure recovery and very distorted outlet flow.
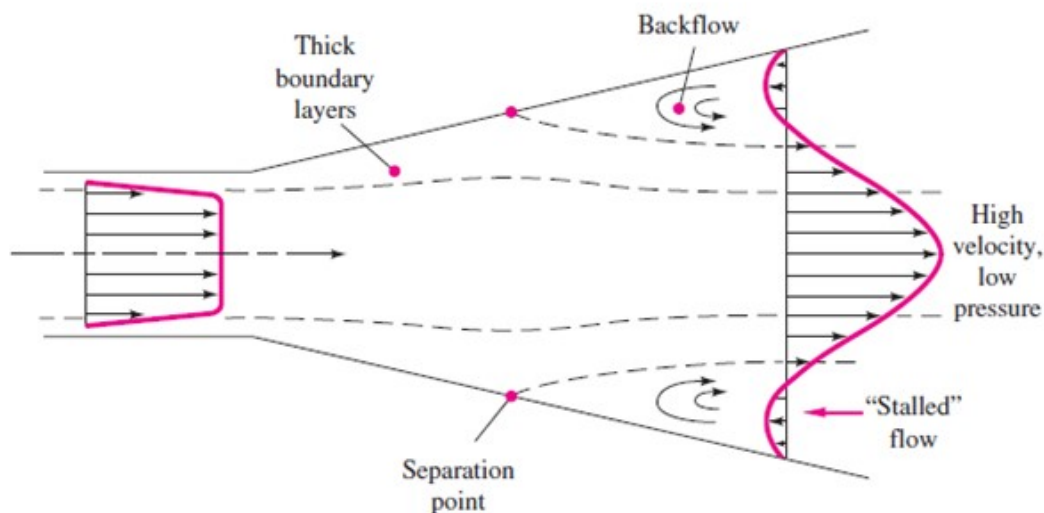
Figure 2.9: Boundary layer separation on diffusers

Source: *F.M. White (2009)*[59]

2.5.2. Flow Regimes

As previously mentioned, there is a clear relationship between performance and the flow regimes found in straight diffusers. While the flow regimes blend into each other, for purposes of description they can be divided into four regimes; *unstalled flow, transitory stall, fully developed or steady stall, and jet flow*

Based on flow visualization techniques, a complete stability map as shown in Figure 2.10 of these four regions was defined by Reneau et al. (1967)[47] as a function of geometrical parameters. This is analogous to setting up a diffuser with a fixed length and opening the divergence of the diffuser angle to identify the different flow regimes.
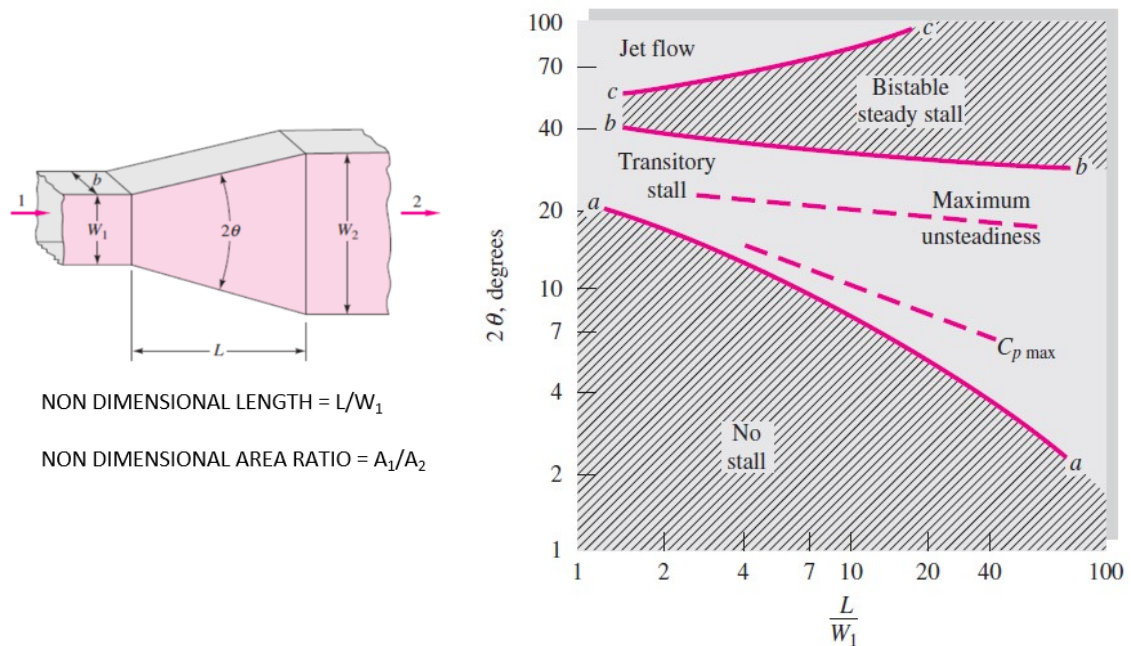
Figure 2.10: Diffuser stability map based on studies by Reneau et al. (1967)

Source: *F.M. White 2008*[59]

Below line $a - a$ there is steady viscous and apparent unseparated flow, with moderately good performance. As the divergence angle is increased, the boundary layer separates at one of the walls, and a stall region with reverse flow is formed. Between lines $a - a$ and $b - b$ is the transitory stall region with a strongly unsteady flow in which flow separation varies in position, size and time. The best performance is found in this region. The third pattern is between $b - b$ and $c - c$, called a region of fully developed stall. In this region, the major part of the diffuser is filled with a recirculation region but extended throughout one wall only with poor performance. The fourth pattern, above line $c - c$ which is known as the jet flow region. Here the wall separation is so gross and pervasive that it separates from both walls, and does not reattach until well downstream from the diffuser. This occurs at high angles of the diffuser and has an extremely poor performance.

2.5.3. Performance Charts

Based on experimental data and existing literature, compiled performance charts have been elaborated (D.S. Miller, 2014)[33] where performance and pressure loss coefficients have been correlated to inlet flow and diffuser geometry conditions. By adopting this approach, the performance of a wide range of diffusers in different operating situations can be covered using relatively few graphs.

For readers who are interested in detailed topics for diffuser design, it is recommended to look into more detail on the book "Internal Flow Systems" by D.S. Miller. In this book, the author specifies a range of perfor-

mance charts based on diffusers with different flows, inlet and outlet conditions. Usually, an optimum design line is included for which the lowest expected loss coefficient is formed.
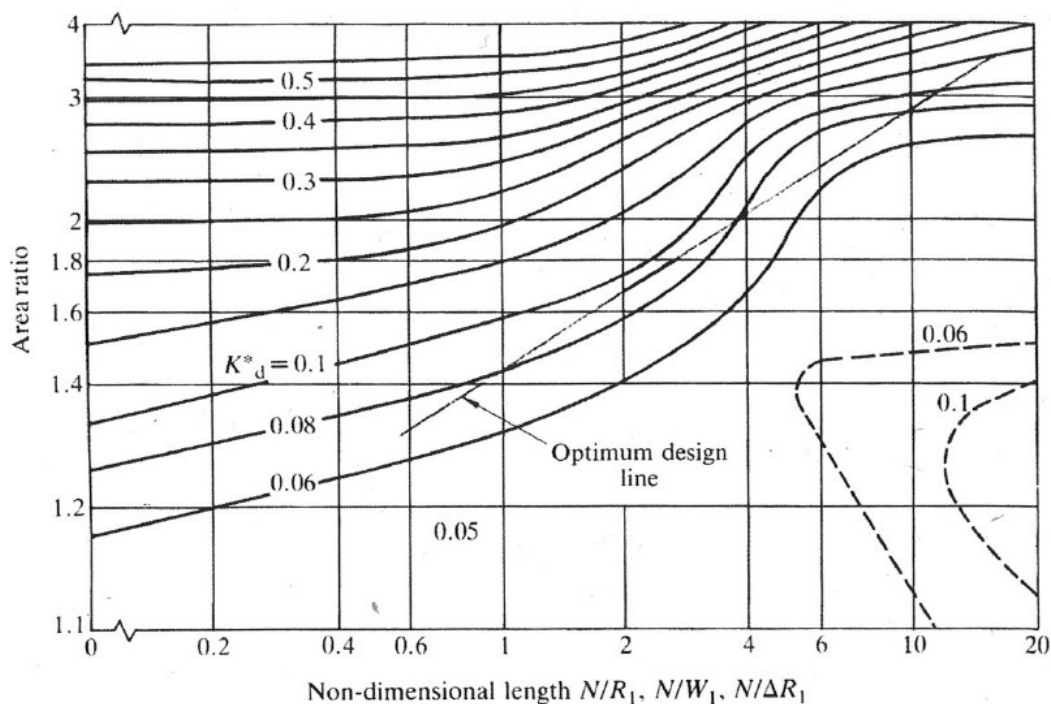
Figure 2.11: Performance chart for diffusers with outlets and developed inlet flows

Source: *D.S. Miller (2014)*[33]

2.5.4. Methods of Improving Performance

According to D.S. Miller (2014)[33], the diffuser performance can be improved on either pressure recovery, flow distribution or flow stability by using one of four methods shown in Figure 2.12 and described below:

- Boundary layer suction

- Boundary layer blowing

- Insertion of guided vanes

- Insertion of vortex generators

Removing low energy near wall flow by suction or energizing the near-wall flow by blowing are very effective methods of improving performance, but are practical only in special circumstances and require the incorporation of external equipment.

Inserting vortex generators on a diffuser may bring high energy fluid down towards the wall to re-energize the near-wall flow, however, these often require the location to be determined experimentally for every particular case.

Installing vanes within a wide-angle diffuser is normally a more practical method of improving static pressure recovery, stability, and outlet flow distribution. With vanes, it is not possible to achieve a static pressure recovery above that of a plain diffuser of the same length and with an area ratio corresponding to that for maximum static pressure recovery according to performance charts, however, it allows for a wider angle diffuser to be used so that flow velocities can be decreased better.

(a) Diffuser with suction

(b) Diffuser with injection

(c) Diffuser with vortex generator

(d) Diffuser with guided vanes
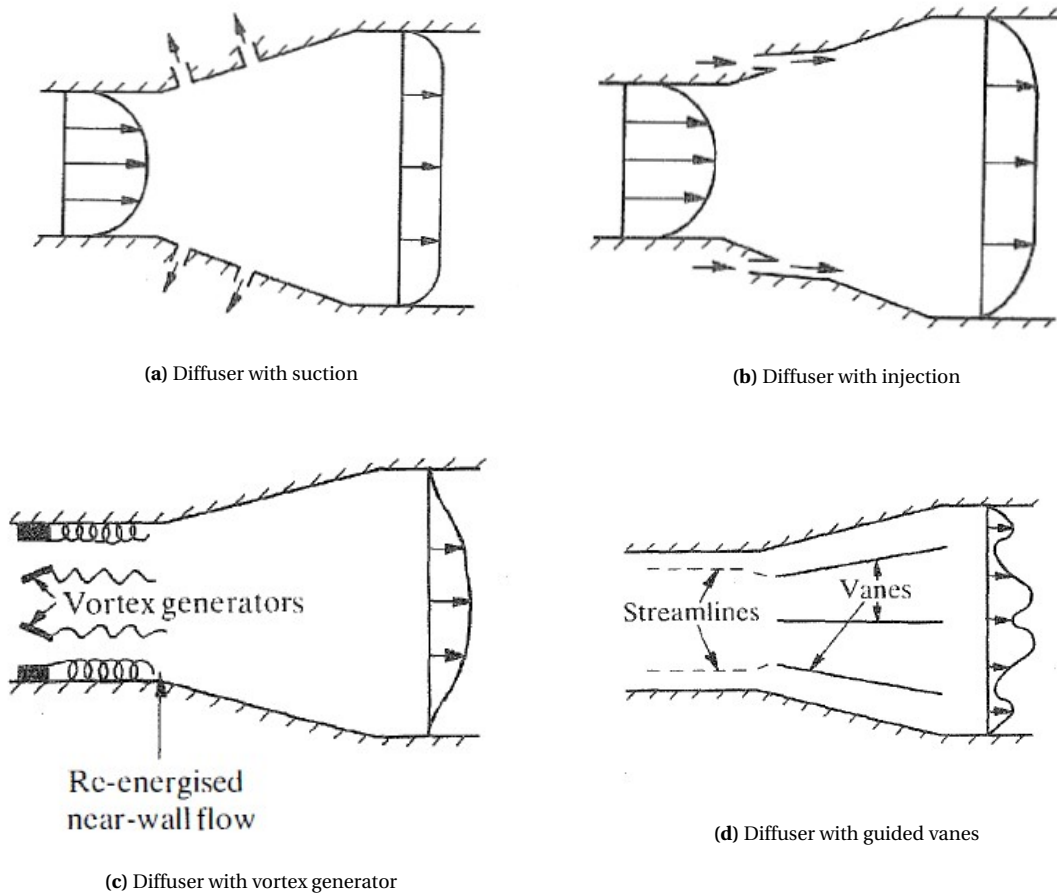
Figure 2.12: Methods of improving diffuser perfomrance

Source: *D.S. Miller (2014)*[33]

3

Experimental Methodology

3.1. Introduction

This section describes how several experiments are conducted in a controlled laboratory environment for three different sediment discharge shapes (diffusers). The objective is to investigate how these phenomena occur and also collect and compare data for future model validation, aiming to minimize the plumes environmental impact. Within these experiments, the aim is to visualize the physical processes of the plume, its trajectory, and impingement area and record it for future video image processing and analysis. Also, velocity and concentration profiles are measured along the plume's centreline at different distances from the diffuser.

Effects of external factors such as ambient currents, nodule collector relative movement, sediment pick up from the crawler tracks or possible flocculation effects have are out of the scope of these experiments.

The experiments have been carried out with the collaboration and supervision of both TU Delft and IHC Mining in the TU Delft Dredging Laboratory's existing $25\,m^3$ modular rectangular tank. This tank has been adapted with a horizontal flat table that acts as the seabed. A $2\,m^3$ mixing tank is used to prepare a mixture that is pumped by a 200 l/min centrifugal pump through the diffusers into the flume.

Section 3.2 explains in detail the used experimental setup, including the diffusers that are analyzed and the type of material that is used to prepare the mixture. Section 3.4 details the instruments that are used to make all of the measurements while Section 3.3 talks about scaling factors used. Section 3.5 presents the experimental procedure that is used, and Section 3.6 shows the list of all experiments that are carried out.

A general layout of the setup is shown in Figure 3.1 and is further explained below.
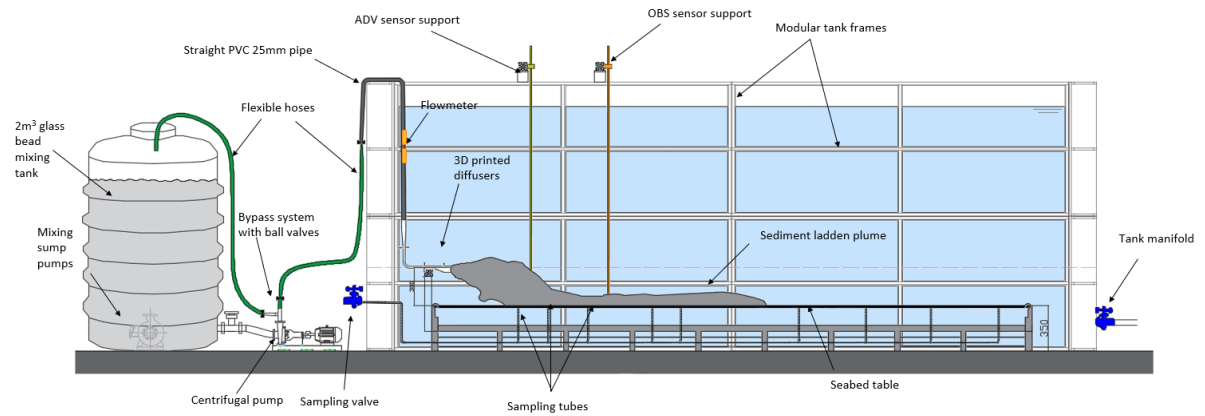
Figure 3.1: Side view of general experimental setup

3.2. Experimental Setup

3.2.1. Flume

A 25m3 rectangular modular tank with glass panels shown in Figure 3.2 is located in the TU Delft dredging laboratory. The tank measures 5.0m in length, 2.5m in width and 2 m in height. It is built with several metal frames and braces that allow for it to be filled up with water. It has transparent glass windows that allow for the possibility to record the physical processes during testing for further analysis. At the top of the modular tank, horizontal beams with sliders are installed to support the measuring instruments, giving them a possibility to move accurately from one location to another. At the back of the tank, a manifold is installed aiming to dissipate any backflow from the plume.

Figure 3.2: Rectangular modular tank

3.2.2. Seabed Table

The table is made of aluminum frames with a surface of acrylic glass panels and represents an artificial seabed boundary. It is positioned in the center of the tank, and its dimensions are 4.5m long and 1.95m wide. Underwater LED lights are installed beneath the acrylic glass panel slabs alongside with diffusive paper to increase flow visibility. The roughness of the slabs or the paper is not tested.

Additionally, 17 holes are drilled in the plexiglass slabs to allow for turbidity measurements to be carried out in different locations of the plume. These holes are connected by flexible hoses that are in turn connected to a ball valve allowing the flow to be drained and sampled outside the tank. These samples are used to measure for local Nephelometric Turbidity Units (NTU) and in turn determine turbidity measurements near the bed. The location of these "tap points" is shown in Figure 3.3.
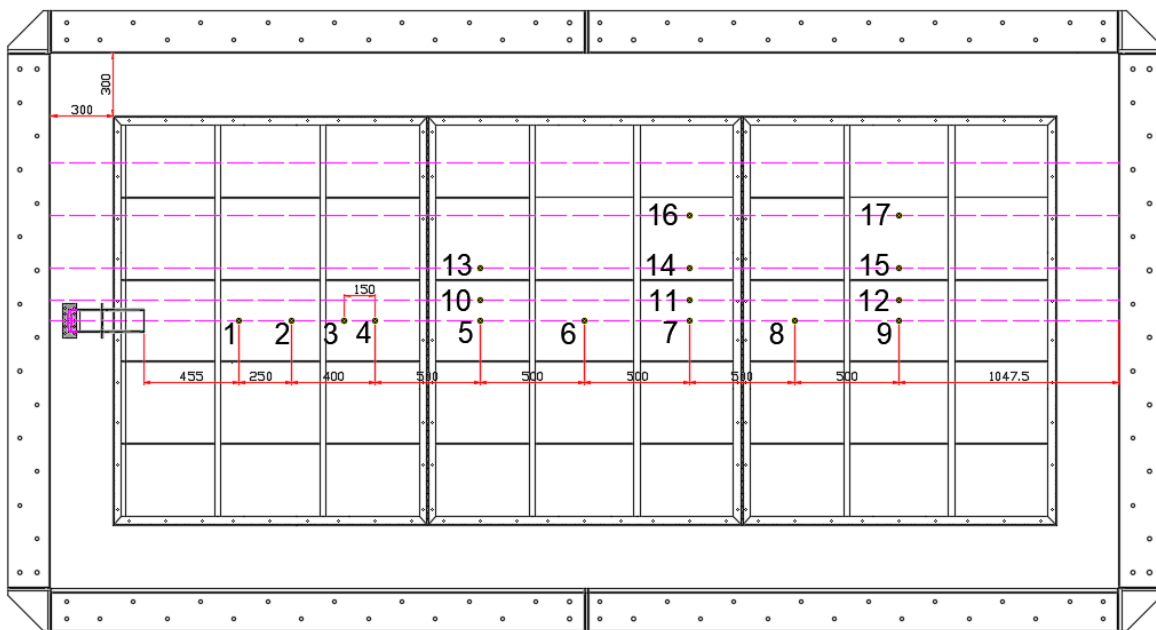
Figure 3.3: Top view table dimensions and sample extraction points

3.2.3. Mixing Tank

A 2m3 plastic tank is used to maintain the mixture ready before it is pumped into the tank. To achieve homogeneity and not allow particles to settle inside the tank, two sump pumps are placed in the mixing tank bed and are continuously pumping mixture in a loop. The temperature is monitored and maintained close to the temperature inside the water tank. An OBS turbidity sensor is placed near the mixing tanks outlet to have a measurement of the concentration that is pumped inside the tank. Flow velocity is controlled by employing a ball valve by-pass system. By calibrating the valves in the by-pass, the target flow is reached while pumping the excess mixture and entrapped air back into the mixing tank.

3.2.4. Diffusers

A total of three diffusers are designed and tested based on the scaling factor of 1:15 and on input parameters defined by IHC Mining. As shown in Figure 3.1 the mixture is first pumped through a vertical 25mm PVC pipe. To transition from the circular section to a slotted 100mm section a transition diffuser shown in Figure 3.4a is used. After the transition diffuser, the vertical flow is modified into a horizontal flow employing a 90° bend shown in Figure 3.4b. These first two components are maintained constant while the three studied diffusers are tested to determine the most efficient one.
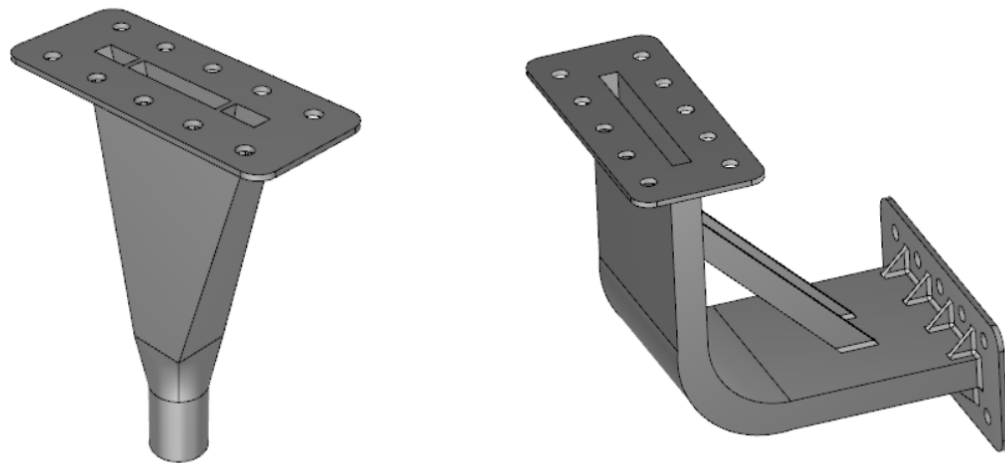
(a) Transition from 25mm pipe to 100mm slot

(b) 90° bend element

(c) Transition components

Figure 3.4: Transition components for all diffusers

All components have been 3D printed from Nylon PA12, which is characterized for its strength, excellent mechanical properties, and durability. All of the diffusers have the same length and width, only their final cross-sectional area ratio differs. Their vertical top elevation is fixed at 31cm above the plexiglass slab. The horizontal position is fixed by employing an aluminum profile attached to the side of the table. The three types of diffusers that are being studied are the Slotted, Vaned and Unvaned diffusers.

Slotted Diffuser

The Slotted diffuser in principle is not a diffuser, but an extension of the outlet in consideration for the nodule collector. It is vital to carry out experiments with this generic shape since it allows for proper benchmarking on any possible improvements. Dimensions of this diffuser have been scaled down based on information from IHC Mining, and a set of 3D and 2D drawings are shown in Figure 3.5
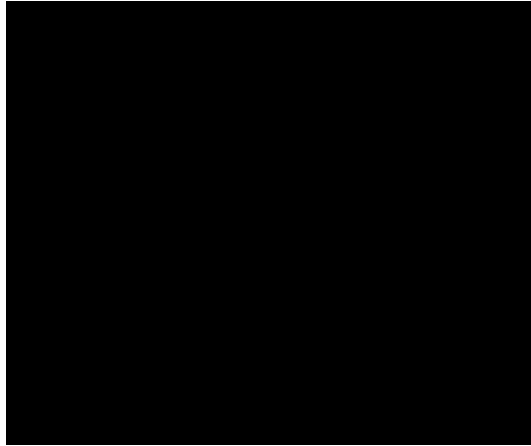
(a) 2D Drawings
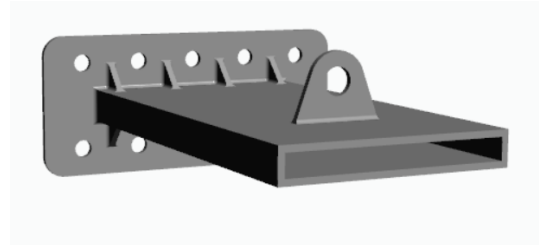
(b) 3D Drawing

Figure 3.5: Slotted Diffuser

Unvaned Diffuser

This diffuser has an area ratio of 4 and a length over width ratio of 7. Based on the literature of the Miller[33] and Figure 2.10, we can expect some stall and flow separation leading to significant changes in pressure recovery and outlet velocity distribution. This diffuser is theorized to have a suboptimal behavior and has been designed this way to have a more visible difference with the Vaned diffuser.

The unvaned diffuser design is shown in Figure 3.6.
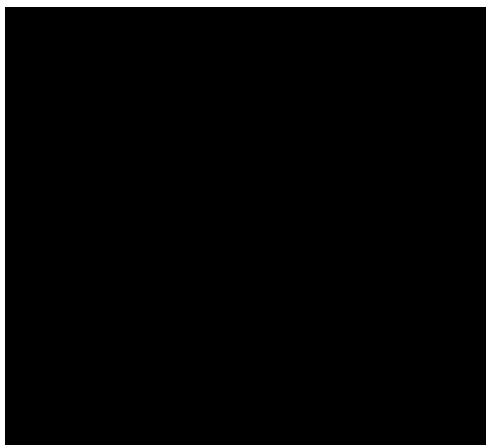
(a) 2D Drawings
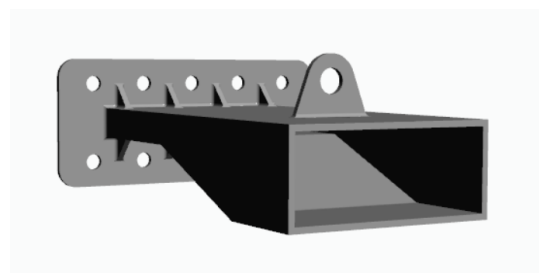
(b) 3D Drawing

Figure 3.6: Unvaned Diffuser

Vaned Diffuser

The vaned diffuser design is duplicated from the unvaned diffuser, however, as its name states it differences itself in the incorporation of vanes inside the diffuser aiming to improve pressure recovery, stability, and outlet flow distribution. A total of 2 vanes are installed with angles according to recommendations from the Miller book looking to guide the flow. Also, the lower bends of the diffuser are concave trying to reduce possible energy losses. The diffuser is shown in Figure 3.7 is expected to have the best performance.

(a) 2D Drawings

(b) 3D Drawing
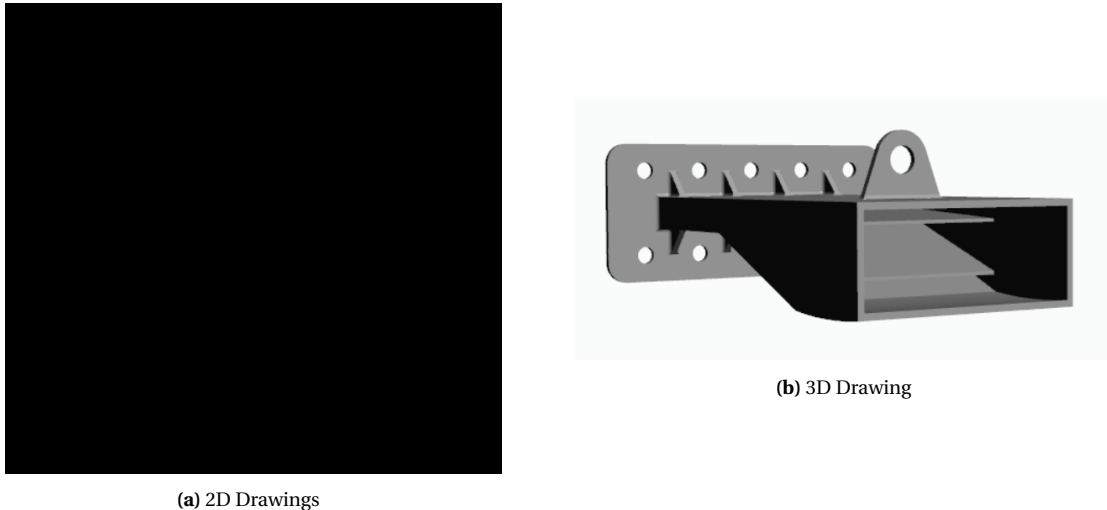
Figure 3.7: Vaned Diffuser

3.2.5. Sediment

The sediment chosen for these experiments are synthetic white, spherical glass beads produced by Holland Mineral. Synthetic glass beads have been used successfully in previous experiments (Lee et al., 2013)[28]. The chosen particle size range is of 65-105 micron due to the actual size of the flume. According to the momentum settling length scale discussed in Section 2.4.3, these particle sizes mixed with their momentum are more likely to settle inside the tank limiting the reflection on the back of the flume and allowing for a longer steady-state duration of the experiments.

Previous experiments conducted in TU Delft (Grunsven (2018)[17] and Byishimo (2018)[6]) used white silica sand. However, due to the presence of very fine particles, the water in the tank would permanently blur therefore a lengthy procedure of washing and drying was required. Glass beads did not have this problem, they have a more uniform size distribution, density and optical properties allowing for easier numerical modeling. Before every experiment, the glass particles are quickly washed once to remove possible dust that could blur the inside of the water tank.

The morphology of the glass particles observed under a microscope and a PSD curve based on a Malvern test are shown in Figure 3.8. More details about the chosen sediment are shown in Appendix E
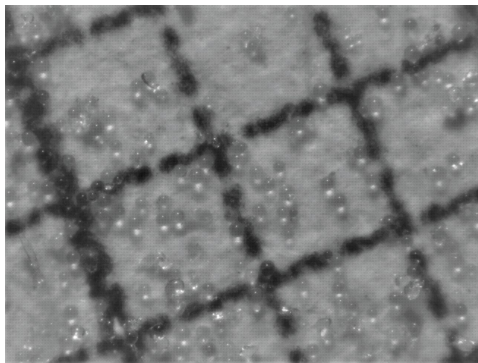
(a) Microscopic imagery
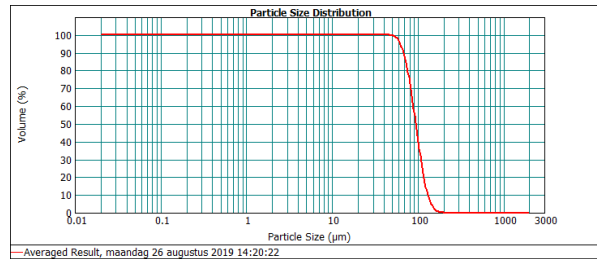
(b) Particle size distribution curve

Figure 3.8: 65-105 micron glass beads

3.3. Scaling Factor

Since setup has been scaled down by a factor of 15, all length scales dimensions are divided down by 15, and the flow velocity is divided by a factor of sqrt(15). Full-scale values such as distance from the seabed suspended sediment concentration, and outlet flow velocity is shown in Table 3.1 and have been supplied by IHC Mining. Laboratory and field values for all these parameters respective flow velocities and diffuser height are shown in Table 3.2 for both previously defined diffuser area ratios.

Table 3.1: Initial parameters supplied by IHC

Table 3.2: IHC mining field and scaled experimental values

Outlet jet velocity	V_j			
Diffuser Height	H_j			
Slot initial Length	B_{j0}			
Densimetric Froude number	Fr_0			
Reynolds number	Re			
Richardson number	Ri			

While defining the scaling factor, the Reynolds and Froude number are considered. Reynolds number is considered as the flow velocity multiplied by the diffuser height and divided by its kinematic viscosity. The Reynolds number is the same for both diffusers since as the velocity decreases for a higher area ratio; the

diffuser height increases as well maintaining it the same. The Reynolds number is calculated to be well above 2300 to assure a turbulent regime which is expected during field operations.

A densimetric Froude number above 1 is maintained in both scenarios to obtain an unstable flow generating internal hydraulic jumps inside the diffuser that produce turbulent mixing and spreading throughout the diffuser walls.

3.4. Experimental Measurements

In this section, the measuring equipment used is briefly explained, as well as the location and calibration procedures.

3.4.1. Outlet Flow Velocity

A Katronic KATflow 200 sensor placed on the round 25mm PVC pipe as shown in Figure 3.9 determines the outflow velocity in the setup. The KATflow 200 is a hand-held ultrasonic flowmeter for non-invasive flow measurement of liquids in filled pipes. It is mounted on the external surface of the PVC pipe and generates and receives ultrasonic signals which allow the measurement of the flow rate.

This instrument records in real-time the flow that is measured inside the PVC pipe, allowing for any corrections if necessary by adjusting the ball valves in the bypass system.
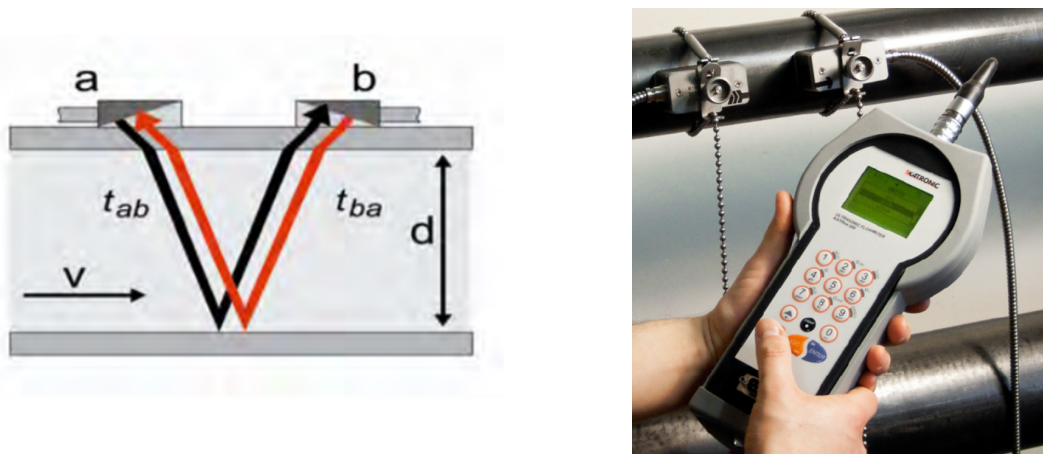
Figure 3.9: Katronic KATflow 200

Source: *UFM*[31]

3.4.2. Velocity Profile Measurements

An Acoustic Doppler Velocimeter (ADV) Vectrino Profiler from Nortek is used to determine the velocity profiles in different locations of the tank. The Vectrino Profiler consists of four receive transducers and a transmit transducer in the center of the stem as shown in Figure 3.10. It measures water velocity using the Doppler effect by transmitting short pairs of sound pulses, listening to their echoes, and ultimately measuring the change in pitch or frequency of the returned sound. Since sound does not reflect on water, it is necessary to have suspended sediment present in the flow.

The Vectrino Profiler can generate a profile of three-component velocities over a vertical range of 3cm, with a resolution of 1mm. It also has the option to perform bottom distance measurements.

The Vectrino Profiler is mounted over a vertical steel rod that is attached to a positioning tool on top of the
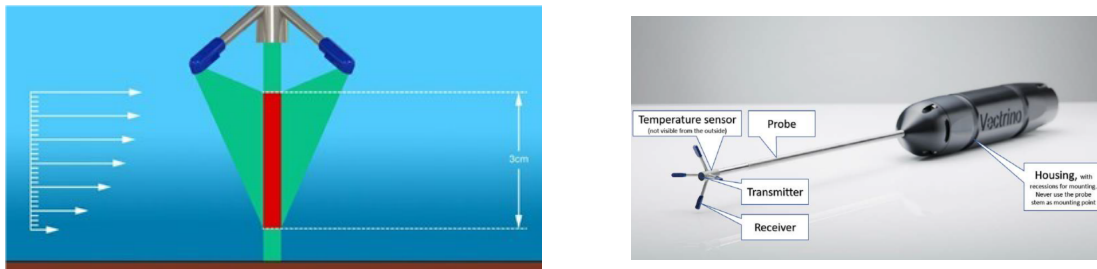
Figure 3.10: Vectrino Profiler

Source: *Nortek*[32]

modular tank's horizontal beams. The positioning tool has a hand crank pulley and a measuring tape attached that allows to move and fix the sensors vertical position. Depending on the position of the plume and the type of diffuser, one or more measurements of the Vectrino Profiler are needed to complete a full velocity profile.

3.4.3. Suspended Sediment Concentration Measurements

To measure the concentration of the glass particles in the plume two methods are used. The first method is by using Optical Back Scatter (OBS) sensors fixed to a steel rod and moving them vertically through the plume employing a positioning tool like the one used for the ADV. The second method involved measuring NTU values by extracting samples of the plume attached to the bed by using the sampling tubes and measuring them with a turbidity meter.

Optical Back Scatter Sensors (OBS)

The OBS is an optical sensor that measures turbidity and suspended solids concentrations by detecting infrared light scattered from suspended matter. For these experiments, three INFINITY-Turbi OBS sensors are supplied by NIOZ.

Two of the sensors are placed inside the modular tank with a small offset as shown below to allow for two profile measurements slightly shifted. The last OBS sensor is placed inside the reservoir tank to monitor turbidity levels in the intake of the pump. The OBS sensor positioning is shown in Figure 3.11
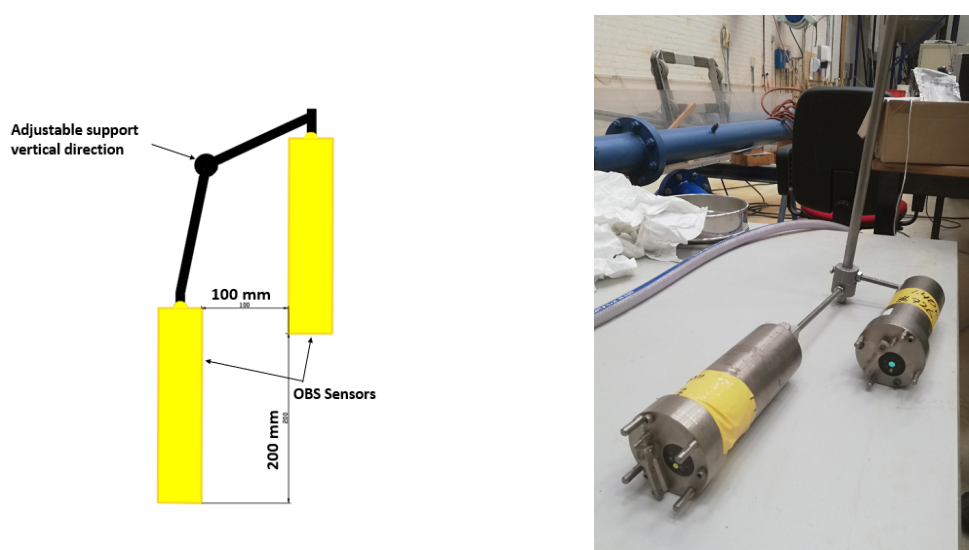
Figure 3.11: OBS sensors positioning

The sensors emit infrared light into the water column, which is reflected in contact with suspended particles. A series of photodiodes positioned around the emitter detects the light reflectance (backscatter), and an empirical calibration is used to convert sensor output voltage into suspended-sediment concentration.

The response of the OBS sensors strongly depends on the size, composition, and shape of the suspended particles. Hence, each sensor must be calibrated using sediment from the site of interest.

The calibration procedure started by preparing a known volume of tap water with a known amount of suspended sediment inside a dark bucket as shown in Figure 3.12. The mixture is maintained homogeneous through a small rotor while turbidity measurements are made for a total of 45 seconds.
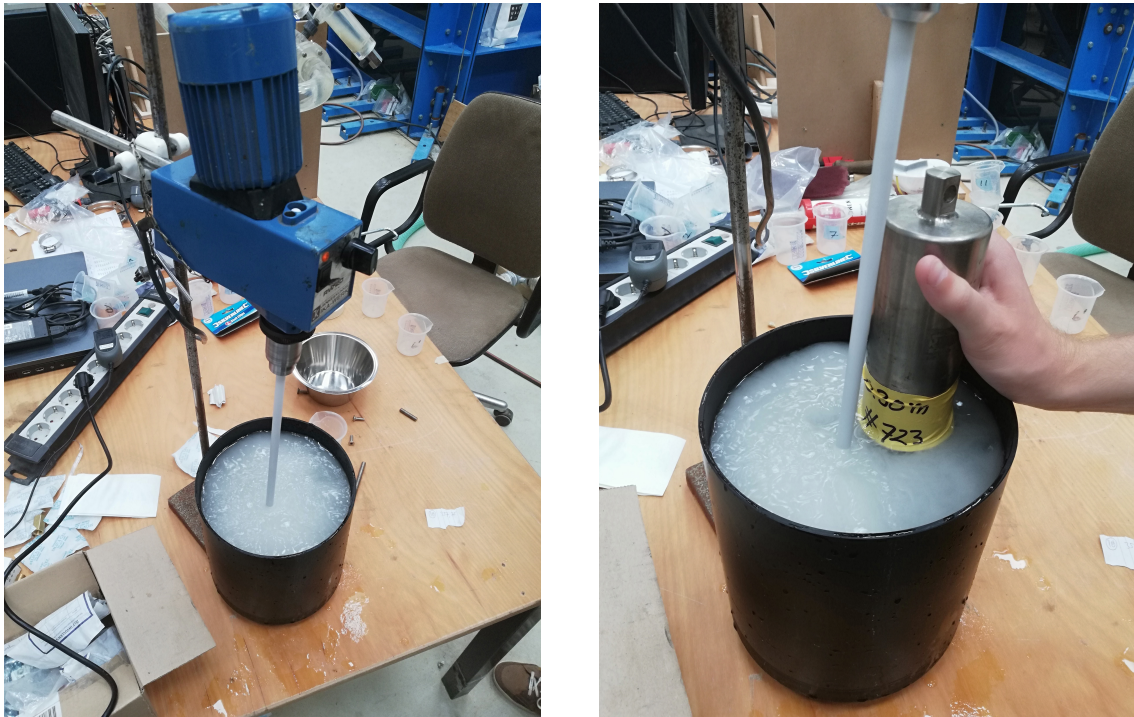
Figure 3.12: OBS sensors calibration procedure

After each measurement, the bucket is emptied and then filled with fresh tap water and material to entail fewer measurement errors. Finally, the data is extracted from every sensor, and the sensors outputs are plotted against the amount of suspended sediment used. A total of 16 measurements for different SSC are done for a range between 0-3% concentration. Each one of the sensors is calibrated separately. The calibration curves are in Figure 3.13.
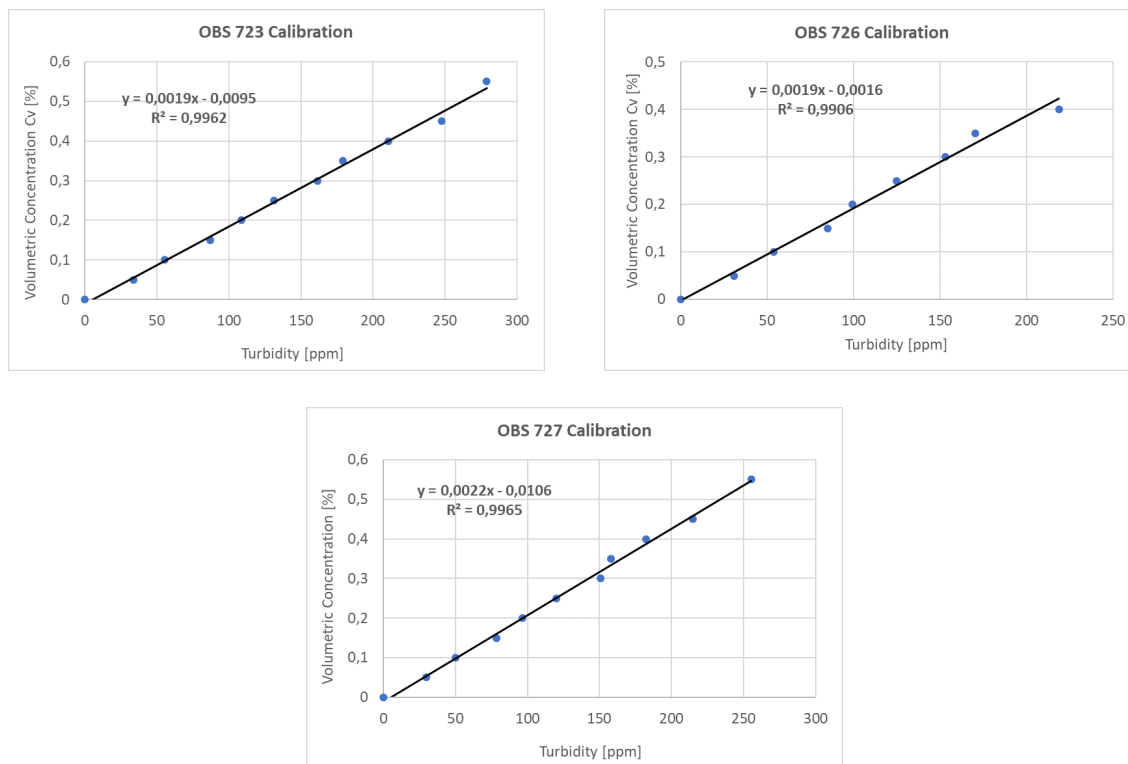
Figure 3.13: Calibration curve OBS sensors

Direct turbidity measurements near bed

Local near-bed suspended sediments concentration measurements are carried out once for every diffuser. Measurements are done once the plume had started to reach a steady-state. One by one, the tube's end valve is opened for approximately 30 seconds in order to flush the tube clean of any sediment accumulation. After this, the samples are taken and stored until the end of the experiment to perform the turbidity measurements.

For the turbidity measurements on the bed, a turbidity meter AL450T-IR is used. Its operating principle consists of filling the transparent vails with the extracted sample and placing them inside the turbidity meter chamber. Infrared lights are emitted, which are reflected by the turbidity of the sample displaying the NTU measurements. Vails are cleaned inside and outside to remove any dust, fingerprints, or water drops to reduce possible errors.

A total of 17 samples are taken from different positions, as shown in Figure 3.3. From these samples, two separate vials are filled and measured three times to obtain an average NTU value.

A calibration curve is formed similar to what is done during the OBS calibration, to convert the NTU into volumetric concentration shown in Figure 3.14.
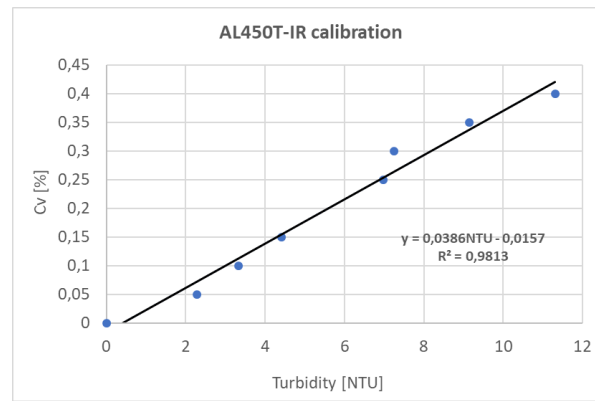
Figure 3.14: Calibration curve AL450T-IR

3.4.4. Horizontal Plume Video Imagery

During the experiments, cameras are used to capture the sediment-laden plume impinging on the flatbed and to follow the development of the resulting turbidity density current over time. Videos are collected on both side view and top view for future processing such as time-averaged contour plumes, dimensions, and current front speeds.

The side view videos are collected using an Optronic CR600x2 digital high-speed camera that can operate at a resolution of 1280 x 1024 pixels, a frame rate of 500 fps and that allows recordings with exposure times as little as one microsecond. All these settings may be configured to increase the recording period or reduce the files sizes. For these experiments, a resolution of 1280 x 600 pixels is used at a frame rate of 50 fps and an exposure time of 1/250 seconds. The camera is positioned in a fixed location for all experiments and recordings of approximately 50 seconds are made after a steady-state could be observed.

For the top view, a GoPro camera is mounted on the horizontal slider on top of the tank. The GoPro is submerged, facing downwards and continuously recorded during the full duration of the experiments. This recording allows viewing the radial distribution of the plume and its footprint.

Higher contrast between the particles inside the plume and the water is obtained by reducing the natural lighting. This is done by limiting the daylight inside the tank by using a tent made of blackout curtains. The only lighting available inside the tent is from the LED lights of the bed table.
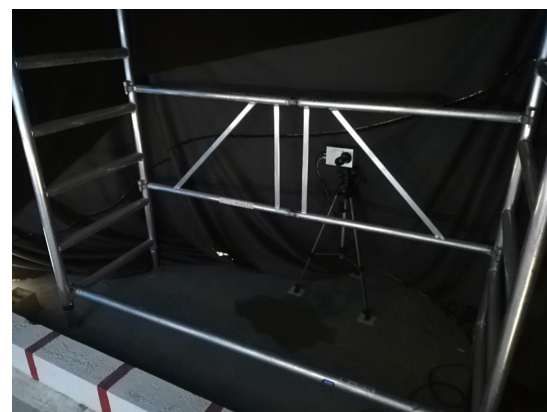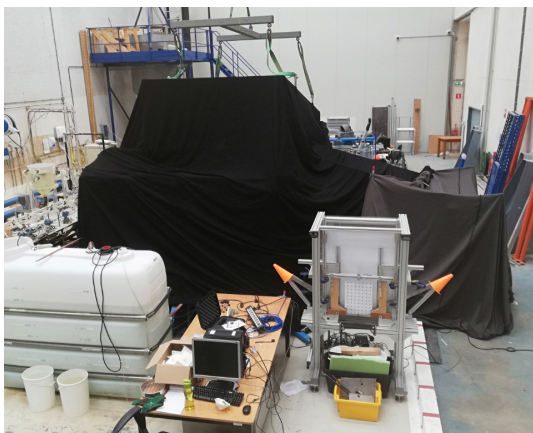
Figure 3.15: Video Imagery Setup

3.5. Experimental Procedure

Before performing any experiment, the water tank is checked to be filled up to a fixed point and in calm water conditions. The temperature of the reservoir and water tank is checked to be within a difference below 1 C° . The material is poured inside the reservoir and mixed for 5 minutes before starting any experiment.

As previously mentioned the experiments consists of visual imagery and profile measurements for three different diffusers. For the visual imagery, experiments are carried out with the blackout curtains in place, and both the high-speed camera and the GoPro are used to record. Additionally, the OBS sensors measure at position C4 of Figure 3.16 to determine turbidity measurements in a fixed position.
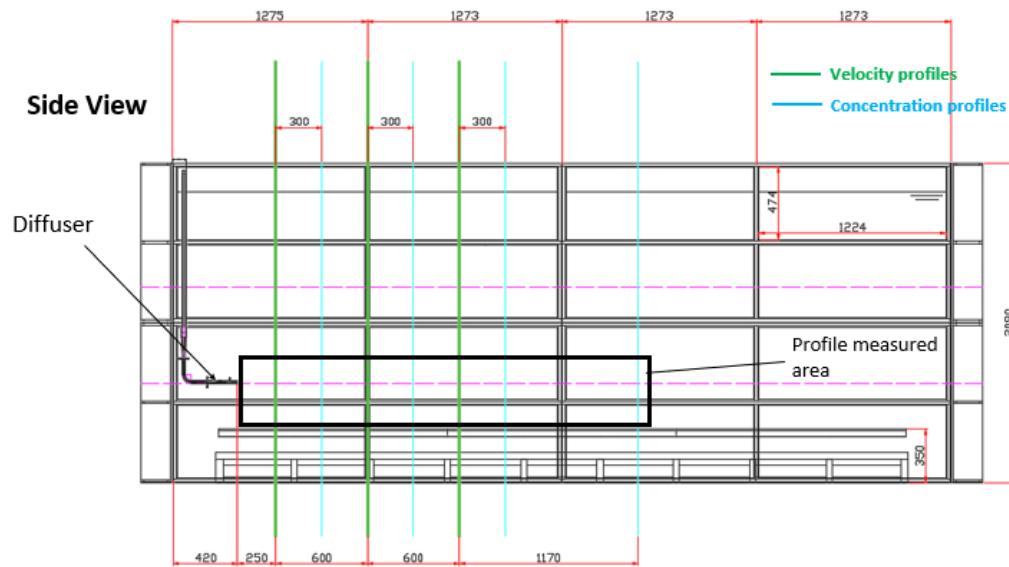
(a) Side view
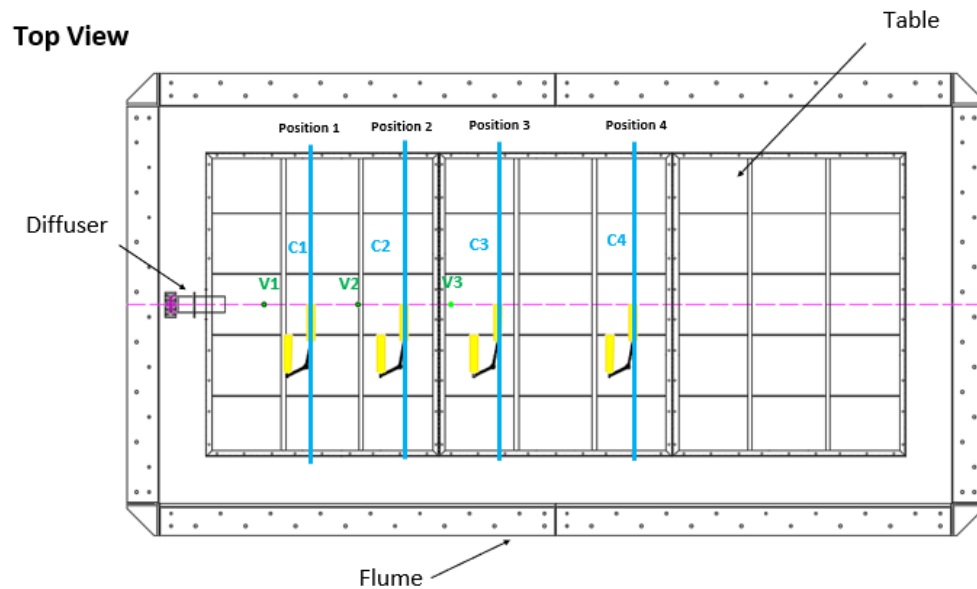
(b) Top view

Figure 3.16: Profile locations

Once the visual experiments are finished, the blackout tent is removed, and the profile measurements are done. As shown in Figure 3.16, the profile measurements are done in the plume centerline at three different locations. Both velocity and concentrations profiles are separated by 300mm and are measured simultaneously during the experiments. The duration of every experiment run lasts approximately 25-30 min; this time is enough to obtain measurements every 3 cm and generate a full profile during one single run. The location of the profile measurements is identical for all diffusers.

After every experiment is finalized all data is collected and stored according to the experiment number and both reservoir and water tank are cleaned with a submerged vacuum cleaner. Finally, the sensors positioning tool is moved, and the sediment for the next experiment is prepared by weighing and washing it to remove any superficial dust.

Once all of the experiments of a particular diffuser are finalized, the tank is emptied and cleaned, and the diffuser is changed into the next one.

3.6. Experimental Scenarios

A total of 19 experiments are carried out to obtain the relevant data for all 3 diffusers. For each diffuser, three velocity and three concentration profiles are measured at the locations discussed above. Both velocity and concentration profiles are measured simultaneously, one in front of the other, during a full experiment. A repeat experiment is carried out once for every diffuser to determine resemblance of results.

Additionally, two visualization experiments are carried out per diffuser, one with increased concentration and one with default concentration. Finally, the last experiment is carried out only with the slotted diffuser with a lower velocity aiming to compare all scenarios with similar momentum values.

For simplicity reasons, the flow velocity has been rounded up to 40 L/min for all conditions except for the lower momentum experiment, which it has been lowered down to 20 L/min. The suspended sediment concentrations have been lowered to 25 g/L for all experiments except for high concentration experiments which have 75 g/L.

A summary of all the experiments that are carried out is presented in Table 3.3.

Table 3.3: Summary of experiment list

#	Date	Experiment number	Type of experiment	Flow Velocity (lts/min)	SSC (g/lts)	Location	Deposition Profile	High Speed Camera	GoPro
1	05/06/2019	Slot_Visual1_20190605	Visual Experiment	40	25	Location 4	-	Yes	Yes
2	06/06/2019	Slot_Visual2_20190606	Visual Experiment / Lower momentum	20	25	Location 4	-	Yes	Yes
3	07/06/2019	Slot_ProfileL1_20190607	Profile Measurement	40	25	Location 1	-	-	Yes
4	23/07/2019	Slot_ProfileL1(2)_20190723	Profile Measurement	40	25	Location 1	-	-	-
5	12/06/2019	Slot_ProfileL2_20190612	Profile Measurement	40	25	Location 2	-	-	-
6	13/06/2019	Slot_ProfileL3_20190613	Profile Measurement	40	25	Location 3	Yes	-	-
7	14/06/2019	Slot_Visual3_20190614	Visual Experiment / High Concentration	40	75	Location 4	-	-	Yes
8	19/06/2019	Vaned_Visual1_20190619	Visual Experiment	40	25	Location 4	-	Yes	Yes
9	20/06/2019	Vaned_Visual2_20190620	Visual Experiment	40	75	Location 4	-	Yes	Yes
10	21/06/2019	Vaned_ProfileL1_20190621	Profile Measurements	40	25	Location 1	-	-	Yes
11	24/06/2019	Vaned_ProfileL2_20190624	Profile Measurements	40	25	Location 2	-	-	-
12	26/06/2019	Vaned_ProfileL2_20190626	Profile Measurements	40	25	Location 2	-	-	-
13	25/06/2019	Vaned_ProfileL3_20190525	Profile Measurements	40	25	Location 3	Yes	-	-
14	11/07/2019	Unvaned_Visual1_20190711	Visual Experiment	40	25	Location 4	-	Yes	Yes
15	12/07/2019	Unvaned_Visual2_20190712	Visual Experiment / High Concentration	40	75	Location 4	-	Yes	Yes
16	15/07/2019	Unvaned_ProfileL1_20190715	Profile Measurements	40	25	Location 1	-	-	Yes
17	17/07/2019	Unvaned_ProfileL1_20190717	Profile Measurements	40	25	Location 1	-	-	-
18	18/07/2019	Unvaned_ProfileL2_20190718	Profile Measurements	40	25	Location 2	-	-	-
19	19/07/2019	Unvaned_ProfileL3_20190719	Profile Measurements	40	25	Location 3	Yes	-	-

4

Experiment Results

4.1. Introduction

In this chapter, a description of the horizontal offset jets is done through experimental results. From these experiments, results for video imagery, sediment deposition, velocity profiles, and turbidity measurements have been obtained for all testing conditions on all three different diffusers. This chapter focuses on presenting and interpreting results after they have been processed and finally summarizing them to have a point of comparison between all diffusers for further analysis in Chapter 5.

The initial conditions at the exit of the diffuser are noted to have a significant influence on the flow development downstream. In Section 4.2 the measured inlet conditions are presented for all experiments. The inlet conditions include the flow rate at which the plume is pumped into the flume from the mixing tank, as well as an attempt to measure the turbidity at the mixing tank's outlet.

Section 4.3 shows an analysis after the visualization experiments from the side view for the high-speed camera as well as a deposition footprint analysis for the top view camera. This section also shows results for the measured front propagation; its time to arrive to the OBS sensors and the turbidity current concentration.

Section 4.4 shows the experimental results for the velocity profiles measured. It describes how the data processing is carried out and graphs are plotted to enable comparison between all diffusers. Similarly section 4.5 shows the turbidity profiles, along with the obtained measurements from the near-bed tap points.

Finally, section 4.6 shows a deposition profile along the centerline for all three diffusers based on measurements obtained by the ADV profiler.

4.2. Inlet Conditions

The exit condition of a jet plays a vital role in the downstream jet development. Therefore, it is of paramount importance to know the jet's initial momentum, density, and suspended sediment concentration. Having all these variables constant for all experiments allows for a fair comparison between all the tested diffusers.

As mentioned in Chapter 3, the inlet conditions measured are the flow rate by employing a KATflow 200 (flowmeter). While an OBS sensor measured the inlet concentration.

4.2.1. Inlet Flow Rate

As mentioned in Chapter 3, the mixture's flow rate is regulated by a ball-valve bypass system in the outlet of the pump. Since the mixing tank is continuously emptying and the KatFlow signal fluctuates a small variation is expected as shown in Figure 4.1. However as can be observed in Table 4.1, the time-averaged flow rate for all experiments is quite close to the targeted 40 lts/min, with a maximum coefficient of variation of 8% which shows a quite acceptable behavior. A graph of the time dependent flow rate has been plotted for all experiments in Appendix A
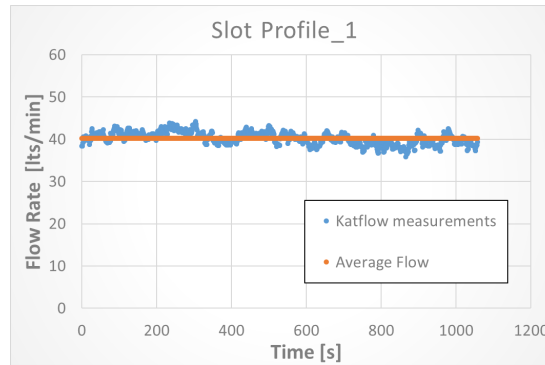
Figure 4.1: Katflow measurements time series

Table 4.1: Flow rate measurements for all experiments

Diffuser	Experiment	Average Flow (lts/min)	C.V.
Slot	Visual1	40.6	7,6%
	Profile1	40,2	5,7%
	Outlet(2)	38,7	2,0%
	Outlet(2)	38,7	2,0%
	Profile1(2)	39,9	2,7%
	Profile2(2)	39,7	3,2%
	Profile3	38,9	3,5%
Vaned	Visual1	39,5	2,3%
	Visual2	41,0	6,6%
	Profile1	40,0	2,2%
	Profile2	40,4	2,4%
	Outlet(2)	40,2	5,4%
	Profile2(2)	39,7	3,2%
	Profile3	39,5	1,9%
Unvaned	Visual1	40,4	2,8%
	Visual2	42,0	3,3%
	Profile1	38,9	2,7%
	Outlet(2)	38,4	3,2%
	Profile1(2)	39,4	3,0%
	Profile2	40,3	2,5%
	Profile3	41,5	2,6%

4.2.2. Inlet Suspended Sediment Concentration

An OBS sensor is placed inside the mixing tank, next to the exit hose, and is used to measure the concentration provided into the the bypass, and thus the diffusers. For all tests, a high variability and lower than expected turbidity measurements have been found. An example of such measurements for the Slot diffuser are shown in Figure 4.2
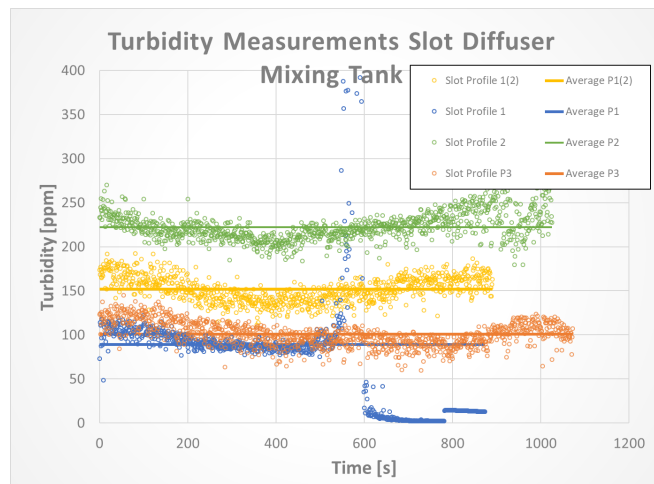
Figure 4.2: OBS measurements in mixing tank

Argued reasons for this high variability is attributed to the aggressive mixing that is present near the sensor that may have altered some measurements. Also, it is possible that the influence of the color of the mixing tank and the present lighting may have also affected. There is evidence found during the calibration experiments for the glass bead particles, that above 1% Cv values the readings are not trustworthy.

For these reasons, the data set of the OBS sensor that is inside the mixing tank is no longer considered. Nevertheless, all the experiments maintained the same procedure of cleaning, weighing, and mixing of the sediment. For all experiments the same mixing pumps and the same proportions of materials are used; therefore they have been analyzed under the assumption that the mixture inside the mixing tank is homogeneously mixed at the proposed concentration.

The measured averaged volumetric concentrations for both initial starting concentration inside the mixing tank are shown in Tables 4.2 and 4.3. For the full plotted time series refer to Appendix A.

Table 4.2: Measured average concentration in mixing tank 1% Cv_o

Start Volumetric Concentration "Cv_o" [%] = 1%			
Diffuser	**Experiment**	**Turbidity average [ppm]**	**Average measured Cv[%]**
Slot	Visual1	314,7	0,68
	Profile1	89,0	0,19
	Profile1 (2)	151,8	0,33
	Profile2	222,4	0,48
	Profile3	100,7	0,21
Vaned	Visual1	60,0	0,12
	Profile1	99,4	0,21
	Profile2	171,1	0,37
	Profile2 (2)	76,0	0,16
	Profile3	116,7	0,25
Unvaned	Visual1	302,8	0,66
	Profile1	321,0	0,70
	Profile1 (2)	333,9	0,73
	Profile2	374,1	0,82
	Profile3	252,3	0,55

Table 4.3: Measured average concentration in mixing tank 3% Cv$_o$

Start Volumetric Concentration "Cv$_o$" [%] = 3%			
Diffuser	**Experiment**	**Turbidity average [ppm]**	**Average measured Cv[%]**
Slot	Visual 3	284,6	0,62
Vaned	Visual 2	-	-
Unvaned	Visual 2	186,6	0,40

4.3. Visualization Experiments

In addition to the detailed measurements of flow velocities and sediment concentration profiles at different locations in the flume, a comprehensive imagery of the experimental plume is needed to determine its trajectory as well as its horizontal span. For this purpose, video imaging is used on both side and top view as shown in Figure 4.3. During video imagery, turbidity measurements are done with the OBS at a fixed position to determine how fast the front of the plume propagated. All visualization experiments are done in a duration of 10 minutes to limit the effects of the backflow that is generated by the plume hitting the sides and the back of the tank.

(a) Side view imagery with high-speed camera

(b) Top view imagery with GoPro camera
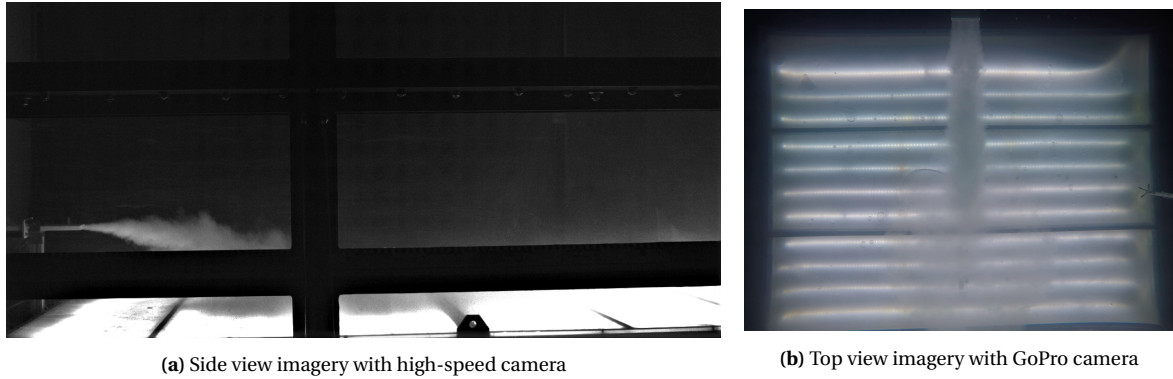
Figure 4.3: Video imagery experiments

4.3.1. Side View

As previously mentioned in Chapter 3.4.4, the side view visualization experiments are done with an Optronic CR600-2X High-Speed Camera located at a fixed location for all experiments. It is not possible to obtain a fully unobstructed view of the plume as it impinges and develops due to the flume's braces and metal framing. However, this imaging allows to infer specific physical properties such as the behavior of the plume at the outlet, particle fallout, the transition between jet and plume and it also allows us to determine an approximate area of impingement. Images extracted from the side view video are scaled into a 2D drawing through which approximate transition lengths and impingement points are determined. The transition length from jet to plume is determined by measuring the distance at which the plume starts to lower and have an irregular shape.

Experiments visual observations show that the flow out of the pipe is turbulent for all cases which was expected based on the calculated Reynolds number. For all cases, comparable behavior is observed in which the horizontal offset jet behaves as a free jet initially, and substantial entrainment can take place before the jet impacts on the seabed due to the negative buoyancy. Ultimately, the flow becomes a wall jet or weak wall plume, depending on the decaying of the velocity and concentration along the way.

(a) Slot diffuser, Low concentration

(b) Slot diffuser, High concentration

(c) Vaned diffuser, Low concentration

(d) Vaned diffuser, High concentration

(e) Unvaned diffuser, Low concentration

(f) Unvaned diffuser, High concentration
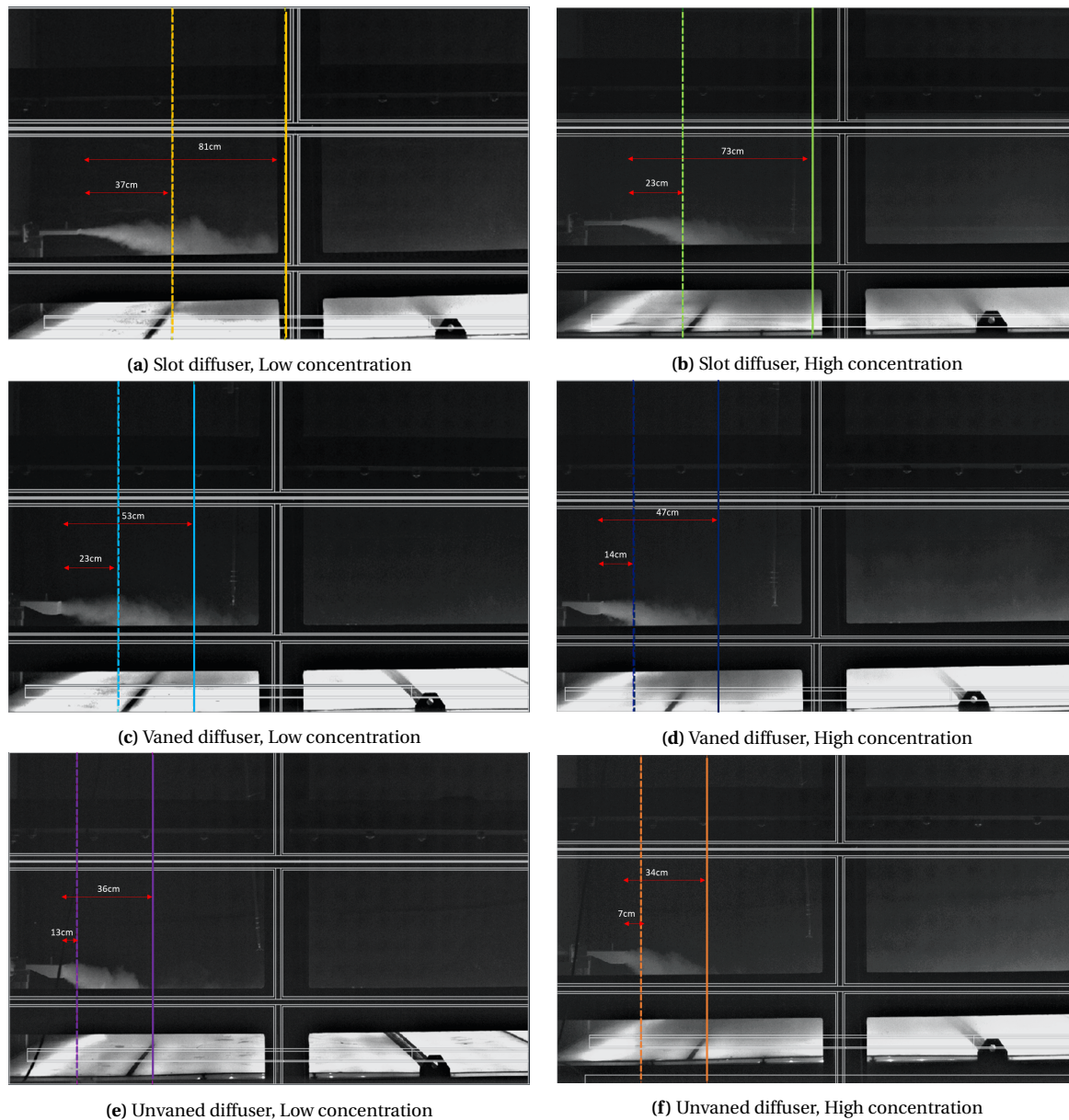
Figure 4.4: Plume transition (dashed line) and impingement point (solid line) for all diffusers

Figure 4.4 shows all the measured jet to plume transition length as well as an approximate impingement point for all visualization experiments. As expected, the slot diffuser has higher initial momentum compared to the other diffusers, stretching out the transition from jet to plume to a larger distance from the source than the other diffusers and impinging at a higher vertical velocity as well. The Slot diffuser evidenced a more severe radial spreading and reflection of the turbidity currents at the sidewalls. Furthermore, the height at which the suspended sediment was observed after impingement was higher compared to the other diffusers. All cases show that both the impingement point and measured plume transition decrease their distance as the volumetric concentration is increased. This is expected behavior since their density differences for both plumes increases, their buoyancy increases, and thus, their Momentum-Buoyancy Length scale decreases.

Figure 4.4 also shows the Unvaned diffuser has lower distances for its impingement point. However, the Unvaned diffuser showed a higher variation in its plume contour proving to have a higher time dependency in its shape, oscillating back and forth from its position.

4.3.2. Top View

For offset jets such as these, as soon as the plume reaches the bed, it impinges generating turbidity currents. When this happens, the plume radially spreads and continues flowing, generating both deposition and erosion. The intensity of this spreading can be seen higher for the slot diffuser thus it is inferred that a higher momentum at the source generates a higher turbidity current on the bed. Within this process also some larger particles start settling closer to the source, whereas the smaller particles are carried for longer distances before depositing on the table.

To compare how this "radial spreading" process is carried out, the top view video images captured with the GoPro have been used. By using video-post processing tools, a footprint area on the table produced by the sediment deposition is calculated every 2 min for the duration of the experiment. The video post-processing is done by separating the footprint from the background light and generating a contour line based on a threshold value. Post-processing is carried out by averaging the pixels of a total of 24 frames (1 second) and subtracting the pixels of the background image. Once this difference is obtained it is transformed into a greyscale image and then scaled down to obtain the highest contrast. A similar approach has been done by Grunsven et al. (2018)[17]. for their vertical plume experiments.

Once the final greyscale image is available, an additional function is incorporated to convert the image into a binary black-white image. This is done by replacing all pixels in the input image with luminance higher than the original threshold value with the value 1 (white) and replacing all other pixels with the value 0 (black).

Since it is not possible to remove the original lighting generated by the LED light strips, the final shape of the footprint is obtained by approximately joining the generated contour manually inside a scaled AutoCAD drawing. An example of this procedure is shown in Figure 4.5.This procedure is repeated for all three diffusers at both high and low concentrations in 120, 240, 360, 480, and 600 seconds after the experiment starts. All calculated contours may be found in Appendix B.
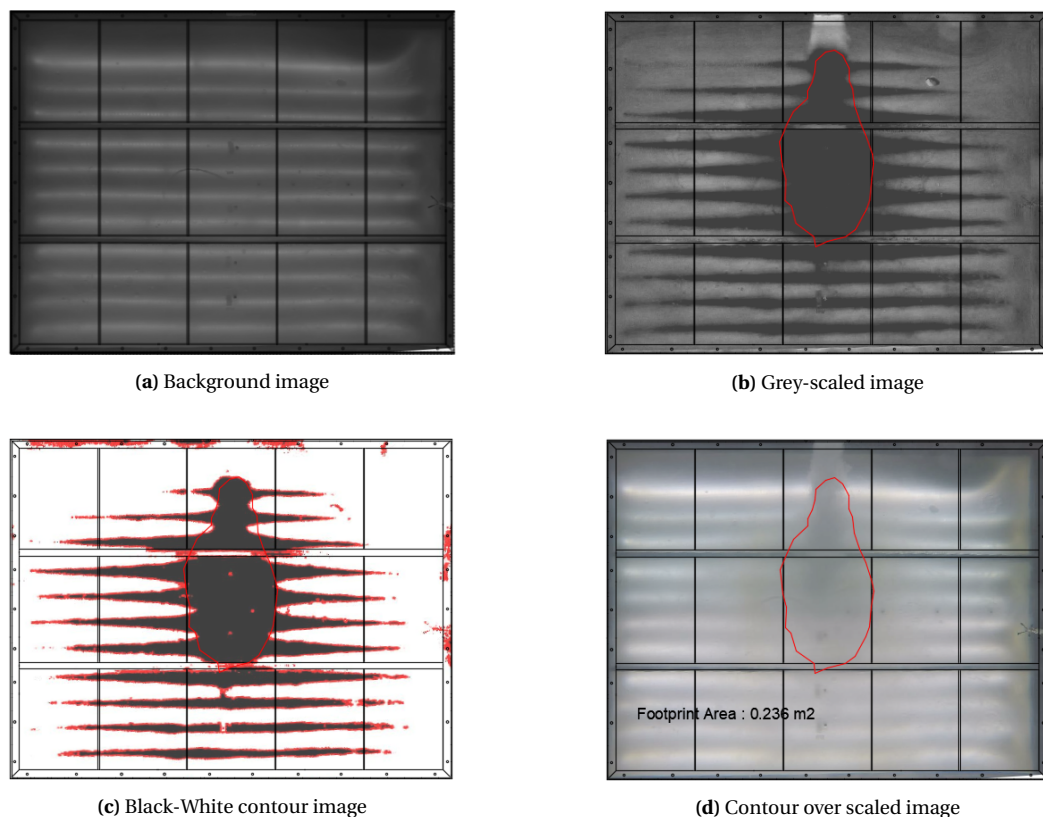

(a) Background image

(b) Grey-scaled image

(c) Black-White contour image

(d) Contour over scaled image

Figure 4.5: Top footprint contour calcualation procedure

One of the main limitations of this experiment is the fact that due to the properties of the material used, there is no flocculation, cohesion, nor interlocking between particles. On the contrary, since they are spherical particles, they tend to slide or roll down, allowing for a lower amount of material to amass resulting in a larger footprint. However since all experiments have been done with the same material and conditions, then a fair qualitative comparison in terms of deposition can be made.

A summary of the results of the generated footprint in shape and location for all visual experiments are shown in Figure 4.6, while Figure 4.7 shows the deposited area size over time.
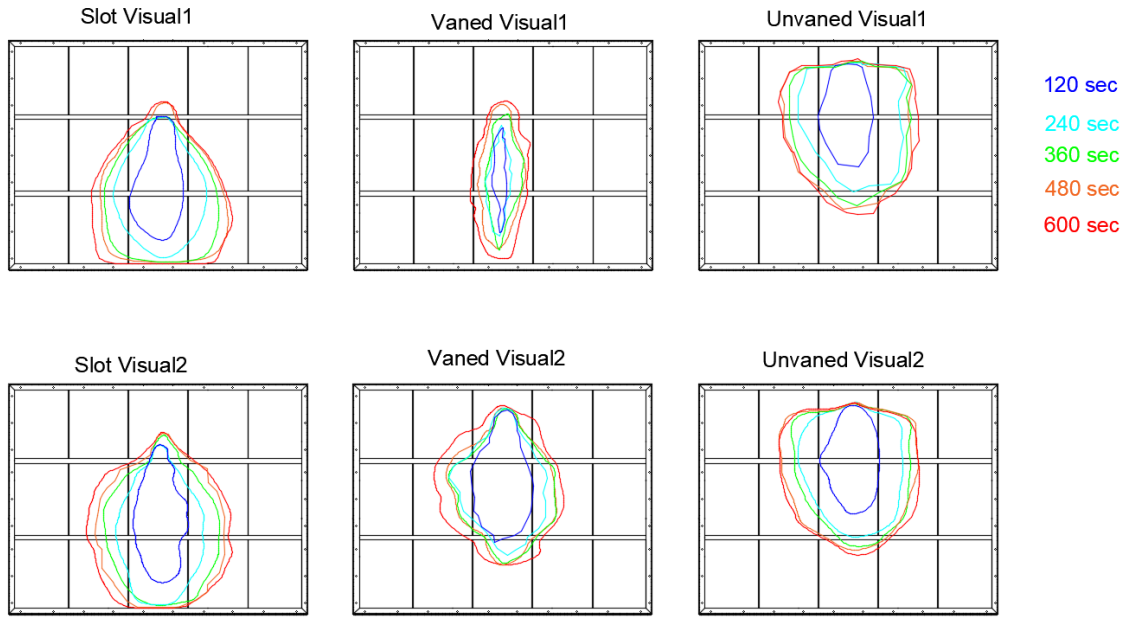
Figure 4.6: Top view footprint spreading for all diffusers

Figure 4.6 allows comparing the generated footprints for all diffusers through time visually. General remarks such as how the footprint is spreading can be observed. The Unvaned diffuser plume settles closer to the source compared to the other diffusers. The Vaned diffuser plume has the lowest footprint area leading to believe that the material has spread out more evenly, while the Slotted diffuser generates the largest area at a higher distance from the source confirming that it is the less ideal scenario. An additional limitation was the video area filmed. Especially for the Slot diffuser, this reduces the area that is measured since it is out of the camera frame.
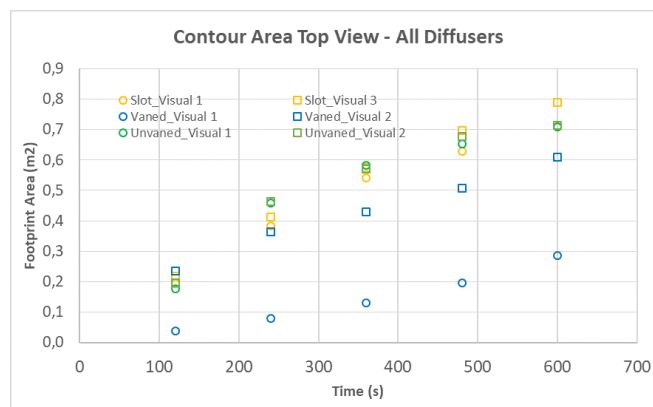
Figure 4.7: Top view footprint contour square meters for all diffusers

4.3.3. Front Velocity and Concentration

The OBS sensors are placed as shown in Figure 4.8 to determine the concentration and the time needed for the plume to arrive at the end of the tank
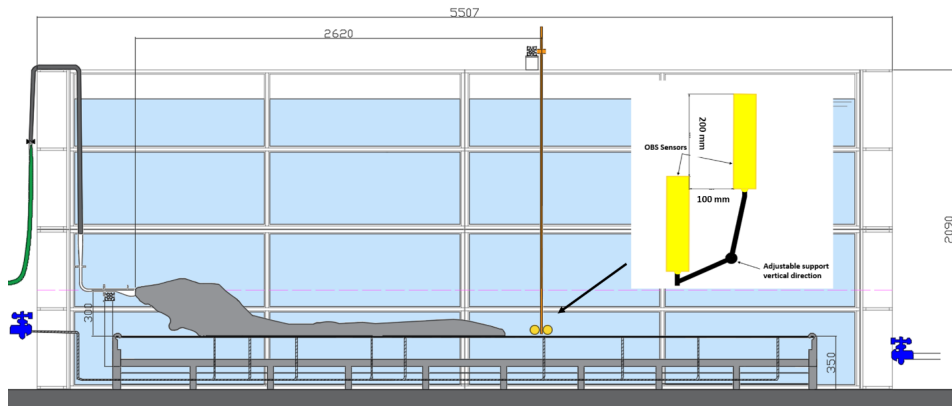
Figure 4.8: OBS sensor placement for front velocity measurements

The OBS sensors recorded the experiment from start to finish at distance of 2620mm from the source and 50mm above the bed. The time the experiment starts is documented and a time-concentration graph is plotted, as shown in Figure 4.9. The total duration of 600 seconds is plotted to show the time the turbidity current reaches the sensor as well as the measured and average concentration values for both centerline and offset sensor. All other graphs have been moved to Appendix B and a summary of the results are shown in Tables 4.4 and 4.5.
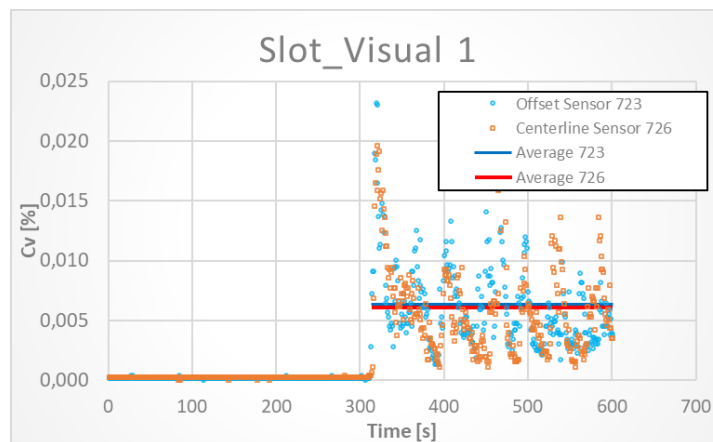

Figure 4.9: Slot Visual 1 offset and centerline OBS sensor concentration-time series

Initially, it was expected to have higher and faster reading in the centreline sensors since this is where the Gaussian maxima are located, however, after viewing the results we can observe that this varies slightly depending on each experiment. A possible explanation of this is the time dependence of the horizontal jet not yet reaching a steady state. Also, the offset sensor is placed before the centreline sensor; thus, the Gaussian maxima is higher in the centreline of the offset location, allowing the distribution spread values to be higher. The differences between the concentration measurements between both sensors are quite low. However, the time the plume arrives the sensors varies quite heavily in some cases. Here it is expected to have the plume of the Slot diffuser to reach sooner since a higher momentum is pushing the turbidity current.

Tables 4.4 and 4.5 show that the plume reaches sooner for all other diffusers compared to the Slot diffuser. It can be argued that this may occur because the plume has a higher concentration of particles that may hinder the propagation of the plume.

Table 4.4: Front velocity, average concentration and time measurements for 1% initial concentration

Start Volumetric Concentration "Cv_o" [%] = 1%				
Diffuser Type	**Centerline Sensor (726)**		**Offset Sensor (723)**	
	Time (s)	Cv_{avr}(%)	Time (s)	Cv_{avr}(%)
Slot	314	0,006	313	0,006
Vaned	230	0,003	126	0,003
Unvaned	48	0,002	249	0,002

Table 4.5: Front velocity, average concentration and time measurements for 3% initial concentration

Start Volumetric Concentration "Cv_o" [%] = 3%				
Diffuser Type	**Centerline Sensor (726)**		**Offset Sensor (723)**	
	Time (s)	Cv_{avr}(%)	Time (s)	Cv_{avr}(%)
Slot	226	0,006	220	0,006
Vaned	107	0,005	205	0,005
Unvaned	96	0,003	296	0,003

4.4. Velocity Profiles

A total of four velocity profiles for every diffuser is measured to be able to compare and observe how the flow diminishes over the length in the flume. Three of the velocity profiles are measured in the plume's centreline at fixed locations and one of them at the source. Additionally, a repeat experiment is carried out to determine if there is much variability between the two profiles in the same location.

Measurements are done using an ADV profiler at a sampling rate of 30 Hz over a total of 45 seconds. Increments of 30mm with a 30x1mm grid size started from the bed and ended where the plume is no longer observed. After each experiment, the data is processed, and the Doppler correlation signal between transmitting and receiving pulses is filtered with a threshold value of 70% according to recommendations of Nortek. Finally, the average time value is obtained for every 1mm throughout the profile. Additionally, an average of 10mm is calculated and plotted to smoothen the velocity profile curve. All diffuser's averaged measurements have been plotted in Figure 4.10 to compare the measured horizontal velocities. Individual velocity profiles (both measured and averaged) for all diffusers are presented in Appendix C.

Figure 4.10 shows that the horizontal measured velocity of the slot diffuser is higher than those of the other diffusers in every location. Again, this is what was expected due to its lower cross-section area and higher momentum. Differences are noticed in the velocity profiles between the Vaned and the Unvaned diffuser, particularly in Profile 1. These profiles were expected be quite similar since both diffusers have the same area ratio. An explanation for this difference may be attributable to scaling factors. The vanes located in the Vaned diffuser may further reduce the cross-section area, increasing its outlet velocity and forward momentum. Since the Unvaned diffuser has its impingement point closer, it is only logical that their velocity profiles may look different as well. Figure 4.11 plots the velocity profiles normalized with respect to each profiles maximum velocity (V/Vm). This figure shows how the velocity profile develops over the length of the plume. It clearly shows a behavior similar to that of an offset jet, as shown in Section 2.3.1. In all cases, it can be observed how the velocity profile has a Gaussian distribution in resemblance to free jet theory. However, a main difference with the free jet theory is that the maximum velocity continues to sag down as the plume advances towards the impingement point. After the impingement point, the other profiles can be seen as a decaying wall jet that reduces its velocity as it distances from the impingement point due to deposition, water entrainment, and shear stresses.

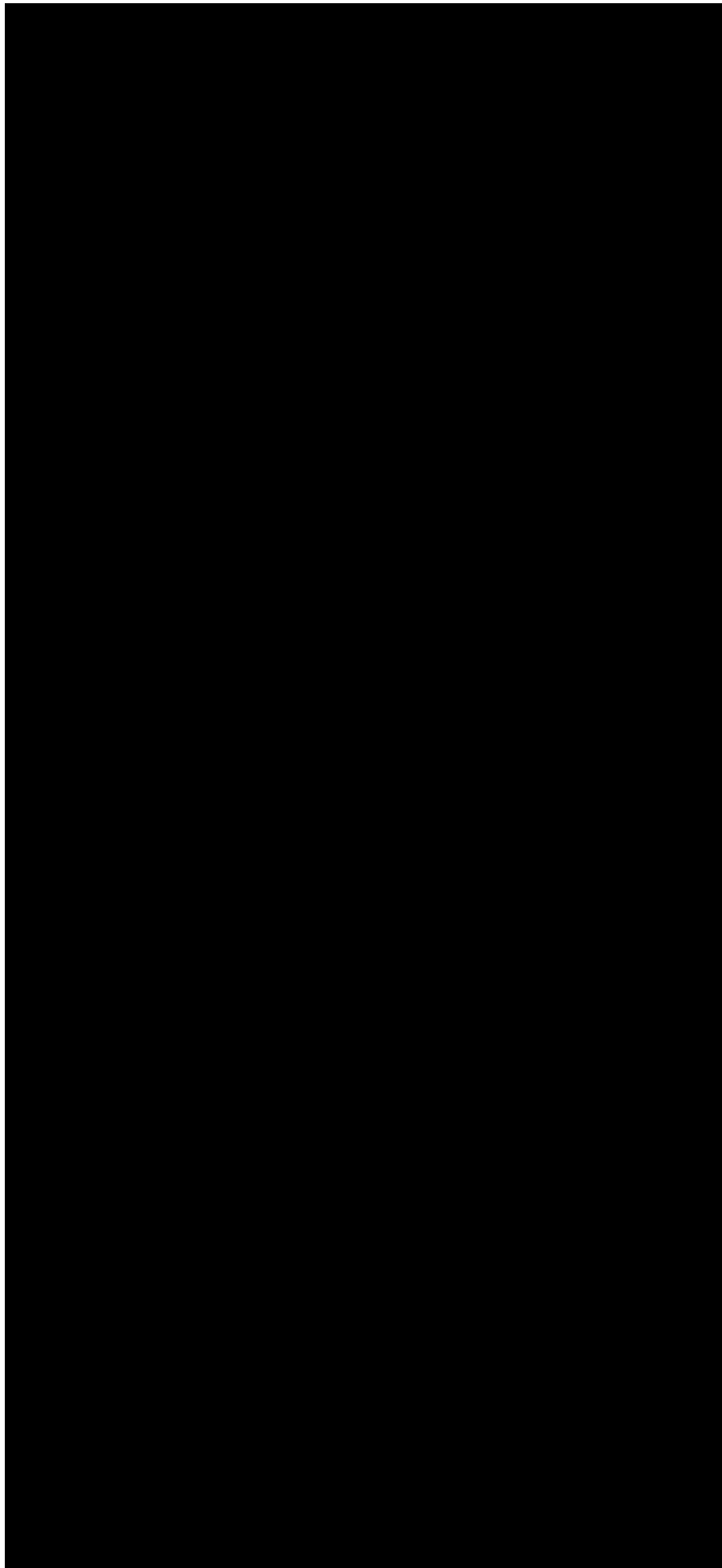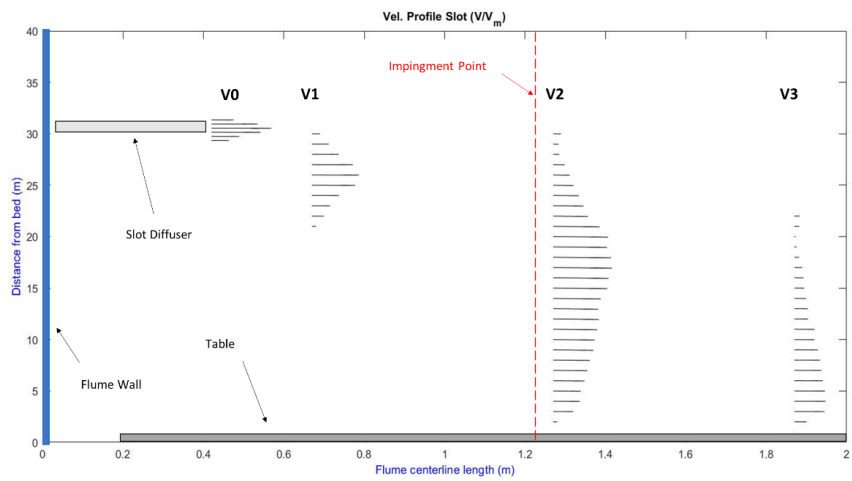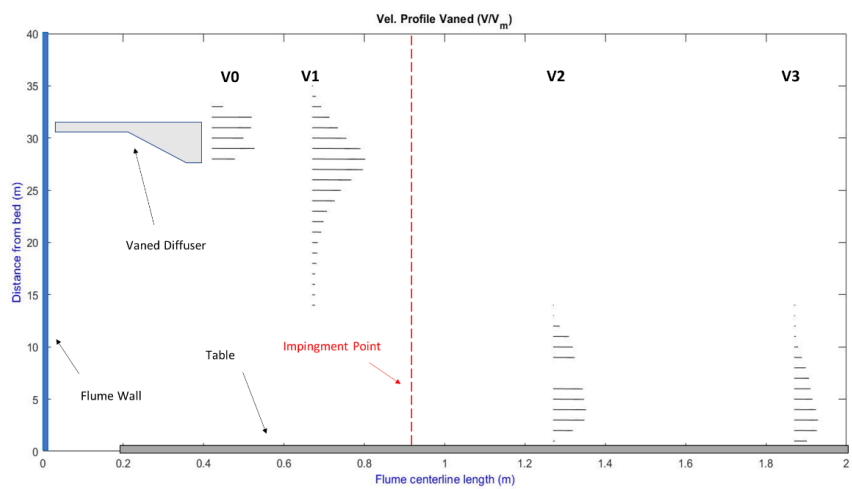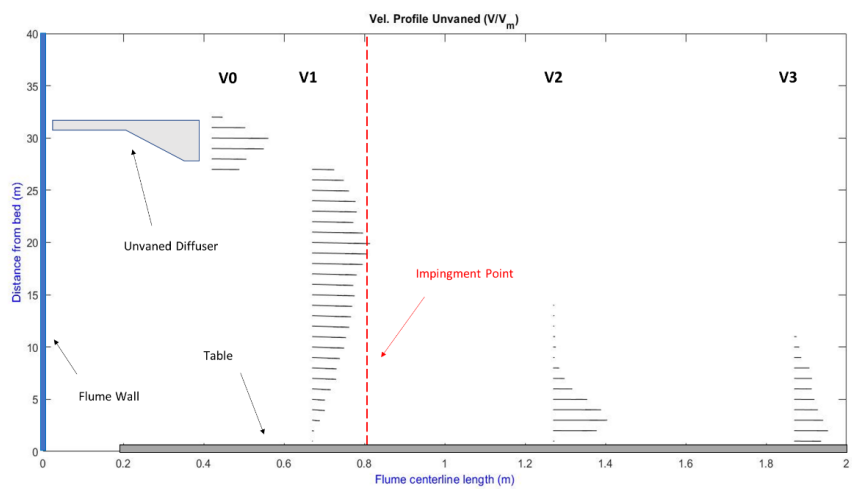**Figure 4.10:** Profile locations

(a) Normalized velocity profiles slot diffuser

(b) Normalized velocity profile Vaned diffuser

(c) Normalized velocity profile Unvaned diffuser

Figure 4.11: Normalized velocity profiles for all diffusers

4.5. Turbidity Measurements

4.5.1. Concentration Profiles

Turbidity measurements at three different locations have been done inside the flume with two OBS sensors, positioned as shown in Figure 3.11. These sensors record measurements continuously at 1 Hz frequency throughout the entire experiment. These point measurements are done simultaneously with the ADV profiler in increments of 3cm and are maintained for 45 seconds trying to capture a steady state. After the whole plume's profile has been measured, the sensors are retrieved, and the data is extracted for processing. It is important to record the exact time the measurements are made since this is used to filter the data that is of interest.

The processing procedure is quite straightforward. The data set has to be filtered according to the exact time when the measurements are made. After this, a time average of 30 seconds is done to obtain a turbidity average measurement. Measurements are then converted to volumetric concentration according to the calibration curve found in Section 3.4.3. Finally, these averaged point measurements are plotted to form a profile, as shown in Figure 4.12. The full concentration profiles for all locations and all diffusers along with the repeat experiments can be found in Appendix D.
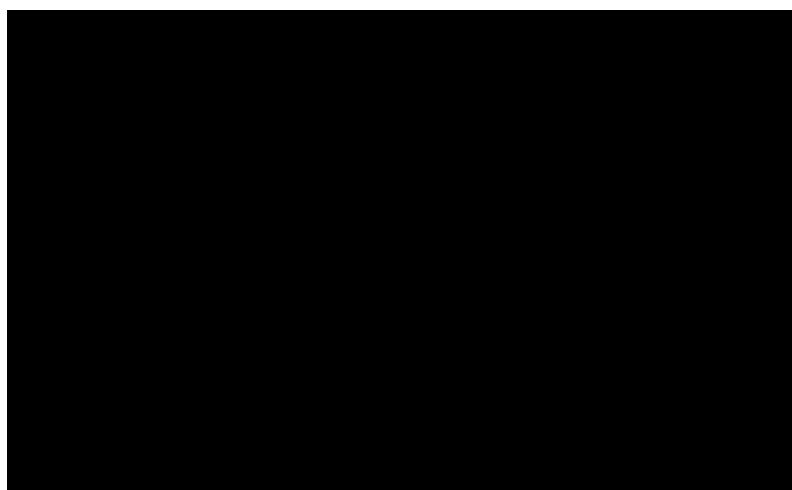

Figure 4.12: Concentration profile Unvaned diffuser profile 2

For comparison purposes, the volumetric concentrations maximum and average values for all diffusers in both sensors can be found in Tables 4.6 - 4.8.

In general, compared with the velocity profiles after impingement in the wall-jet regime, the maximum points of the concentration profiles seem much closer to the bed and the overall profiles are asymmetric vertically with a steeper slope towards the bottom. This jet behavior is in accordance to offset jet theory discussed in Chapter 2. The measurements show a higher concentration for the slot diffuser in all locations as is expected because of its larger settling length scale compared to both Vaned and Unvaned diffusers. For all diffusers, the plume dilutes as it spreads towards the end of the tank because of its water entrainment reducing the measured concentration. If the initial concentration is considered constant at 1%, values range between up to 10-12 times in dilution for the first profile and up 100 times dilution in the last profile.

The main limitation with this type of measurement technique is that measurements might have been affected by the possible reverse flow on the side and back of the walls. All measurements for the OBS sensors show a non-stable high time-dependent behavior; therefore, measurements may not be considered as accurate as hoped. Time plot for the OBS sensors is displayed in Appendix D where readings for the duration of the experiment and background measurement for 10 min prior to starting are plotted.

4.5.2. Near Bed Turbidity Measurements

As mentioned in Section 3.4.3, near-bed turbidity measurements are done on one experiment for all diffusers extracting samples throughout Poly-Flo tubes located at the bed according to Figure 4.13. The procedure for

Table 4.6: Maximum and average concentration Profile 1

Profile 1 (x = 0.55m)				
Diffuser Type	**Centerline Sensor (726)**		**Offset Sensor (723)**	
	Cv_{max}(%)	Cv_{avr}(%)	Cv_{max}(%)	Cv_{avr}(%)
Slot	0,108	0,038	0,000	0,000
Vaned	0,072	0,037	0,025	0,003
Unvaned	0,094	0,026	0,106	0,029

Table 4.7: Maximum and average concentration Profile 2

Profile 2 (x = 1.15m)				
Diffuser Type	**Centerline Sensor (726)**		**Offset Sensor (723)**	
	Cv_{max}(%)	Cv_{avr}(%)	Cv_{max}(%)	Cv_{avr}(%)
Slot	0,094	0,027	0,078	0,025
Vaned	0,060	0,018	0,018	0,005
Unvaned	0,032	0,010	0,035	0,012

Table 4.8: Maximum and average concentration Profile 3

Profile 3 (x = 1.75m)				
Diffuser Type	**Centerline Sensor (726)**		**Offset Sensor (723)**	
	Cv_{max}(%)	Cv_{avr}(%)	Cv_{max}(%)	Cv_{avr}(%)
Slot	0,029	0,007	0,038	0,015
Vaned	0,021	0,008	0,007	0,003
Unvaned	0,004	0,001	0,009	0,003

sample recollection was allowing the plume to develop for approximately 3-4 min. Before taking the sample, the valve is opened for 30 seconds in order to flush any existing material. Then samples are taken in order from the 1st tap point until the 17th one. After the sampling is done, measurements are made through the turbidimeter.

Ideally, a longitudinal profile and 2 cross-sections are measured. The OBS sensors for the different profiles are located close to some of the tap points, as shown in Figure 4.13 therefore comparable results are expected. However, after reviewing the results, these measurements seem somewhat unreliable. The centreline concentration measurements for all profiles do not vary much as would be expected as the distance from the origin increases. Also, some high measurements are obtained evidencing differences between the OBS measurements and what has been observed visually.

Unreliable results can be attributed to the used material properties. In the turbidity meter, an artificial light source emits a known intensity of light through a sample where the suspended particles scatter or absorb the light. This measuring technique was successfully used in other researches, such as Byishimo (2018)[6]. Their material was not transparent glass beads but instead a Silica Sand that would blur the water allowing for more precise measurements of turbidity. The full measured profiles are shown in Appendix D for all diffusers.
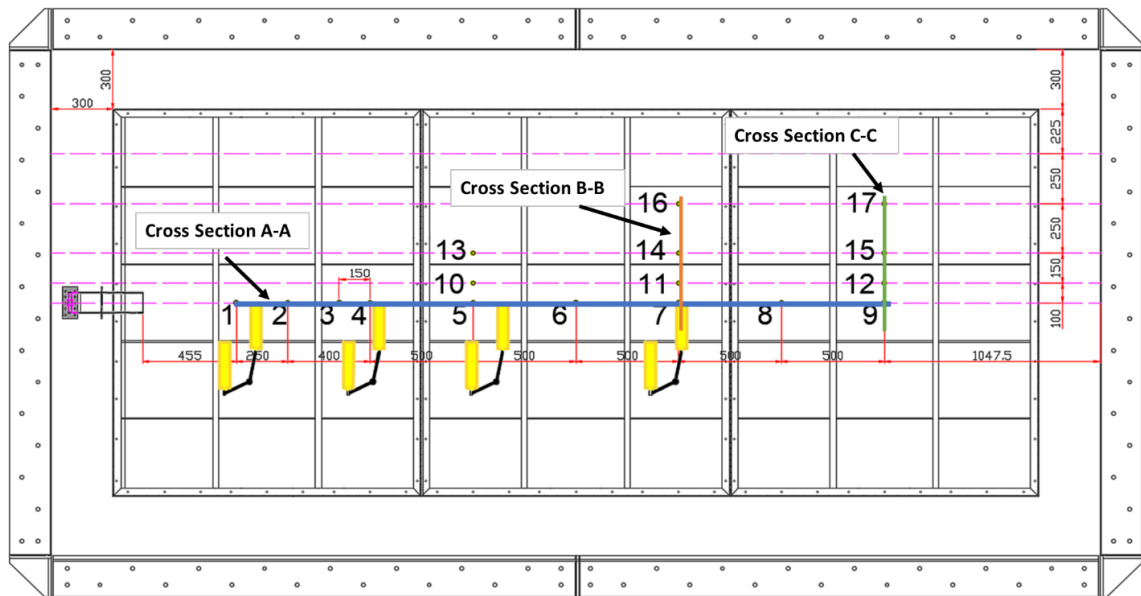
Figure 4.13: Near bed turbidity measurements cross sections

4.6. Bed Deposition

The bed deposition measurements are carried out utilizing the bottom distance check function of the Vectrino Profiler. Measurements are done once a total of 1m3 of the mixture is pumped into the flume. Once the sediment has settled, the ADV is fixed a specific height and measurements are made. A total of 16 measurements are made along the diffusers centreline.

As jet flow increases, the magnitude of the maximum deposition rate gradually decreases, but the deposition profile shifts to more downstream (Lee, 2013)[28]. Particles with smaller settling velocities would be transported further downstream, and so the location of maximum deposition rate increases, and the deposition rate pattern becomes flatter. Results have been tabulated in a non-dimensional height z/z_{max} for all diffusers in Table 4.9 where z_{max} is each diffusers maximum measured deposition height.

Measurements agree with what is visually observed and commented in Section 4.3. The slot diffuser shows a broader spread all over the length of the flume while the Vaned and Unvaned diffusers footprint is closer to the source. Out of the three diffusers, the Unvaned diffuser showed a higher deposition closest to the source. The deposition distribution is plotted in Figure 4.14.

Table 4.9: Non-dimensional deposition height for all diffusers in centerline

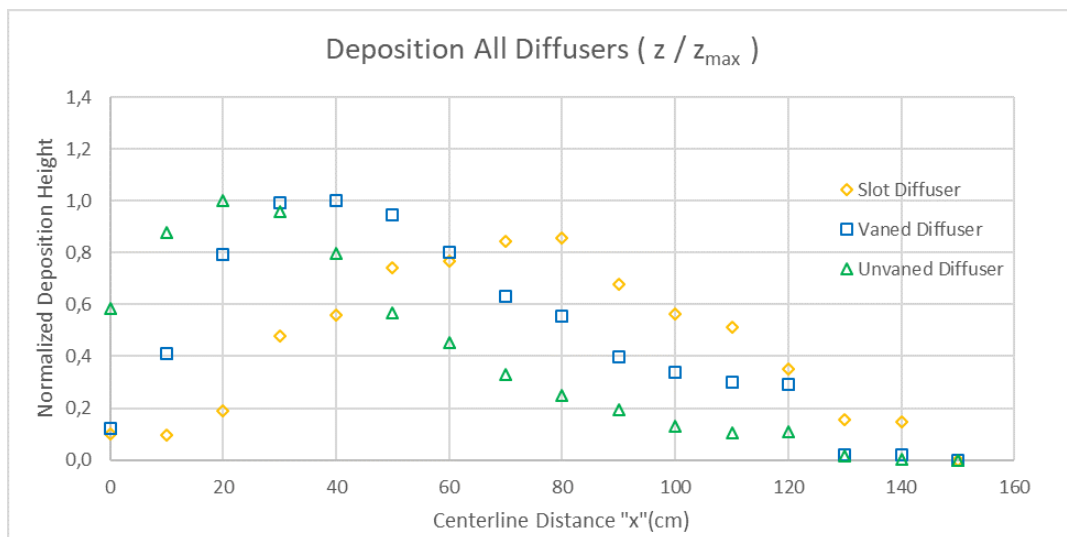| Normalized Deposition Height (z / zmax)			
Distance x (cm)	*Slot*	*Vaned*	*Unvaned*
0	0,12	0,12	0,58
10	0,11	0,41	0,88
20	0,22	0,79	1,00
30	0,56	0,99	0,96
40	0,65	1,00	0,80
50	0,87	0,94	0,57
60	0,90	0,80	0,45
70	0,99	0,63	0,33
80	1,00	0,56	0,25
90	0,79	0,40	0,19
100	0,66	0,34	0,13
110	0,60	0,30	0,11
120	0,41	0,29	0,11
130	0,18	0,02	0,02
140	0,17	0,02	0,00
150	0,00	0,00	0,00

Figure 4.14: Deposition profile in centerline for all diffusers

5

Analysis of Experiments

5.1. Introduction

On the previous chapter, the behavior of the plume for different outlet shapes was recorded, and both velocity and concentration measurements were made along its centreline. The observed plume had a behavior similar to that of an offset jet where first an entrainment area can be distinguished followed by an impingement zone and finally a wall jet propagation area.

This chapter discusses the obtained experimental results and compares them with calculations based on dimensional analysis and integral models that have been calculated for free jets. Also, some critical physical processes that are observed have been commented on.

Section 5.2 discusses the key physical processes that are observed during the experiments, dividing them into three different areas; the diffuser outlet, the impingement area, and the turbidity current.

Section 5.3 gives a brief overview of why a dimensional analysis and an integral model approach is used. Section 5.4 compares some of the measured results with a dimensional analysis that is reviewed during the literature study. The transition from jet to plume is measured through the visualization experiments and can be compared with other research based on a Momentum-Buoyancy length scale. The impingement point is estimated and is compared based on dimensional analysis found on literature for sediment-laden plumes.

Finaly, in Section 5.5 the measured velocity profiles are compared to calculations of a integral model for free jets. Also, the self-similarity of the profiles is studied as the values are fitted into Gaussian distribution curves. Concentration profiles have not been checked since the data points are scarce.

5.2. Key Physical Processes

A conceptual model has been made based on key physical processes that are observed during the experiments. These processes all interact with one another, and they are divided into three areas, as shown in Figure 5.1.

First, it is essential to determine all of the sediment properties as well as the ambient conditions. As previously explained, ambient conditions such as currents and stratification are not considered in these experiments. However, ambient conditions such as water temperature, outlet material, or the sediment density, size, and shape are important for determining the model's main variables effectively.
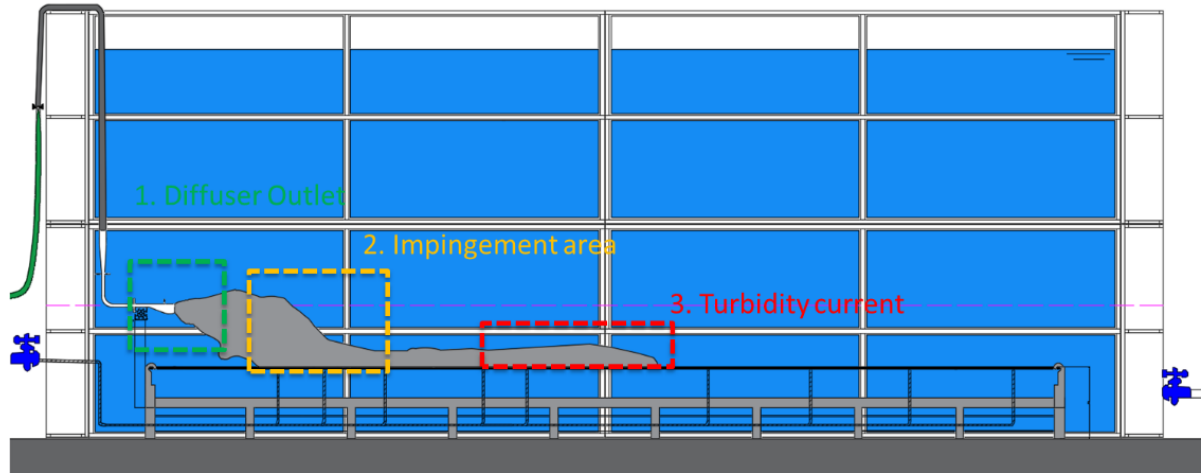
Figure 5.1: Conceptual model areas of interest

Based on the ambient conditions, the main initial variables inside the model may be calculated. These variables are the mixture density, suspended sediment concentration, and the flow velocity, which depends on the diffuser shape as well. Also, it is quite important to determine the measured distance from the bed since it affects the plume's behavior. If the distance from the bed to the diffuser is too low, it is possible to have low-pressure areas beneath the diffuser that prompt the Coanda effect. For these experiments, the diffuser is set horizontally; however, an important variable that alters the plume's behavior is the diffuser angle. Finally, an entrainment coefficient is determined based on previous assumptions adopted on literature (Fischer, 1979)[16] which allows determining the plume's spreading.

The first stage of the conceptual model is at the diffuser. Here it is essential to know about the initial buoyancy and momentum conditions since these control most of the plume's behavior. Once the plume spreads throughout the diffuser, its properties change and undergo mixing due to jet turbulence and water entrainment. This mixing process spreads out the plume radially and reduces the plumes velocity profile. Since it is a sediment-laden plume as well, it is important to also take into consideration possible settling of particles and their resuspension due to water entrainment.

The next stage is the impingement area. Because of the plume's negative buoyancy and the presence of the boundary condition, the jet impinges against the table top. Once this happens, a layer that starts to deposit and spread out radially. After a steady-state is reached, a bed of sediment develops, and erosion and resuspension of particles start to occur. Impingement of an offset jet generates a wall jet in every direction radially. Not only in a forward direction but also a backflow and side flows have been observed during the experiments.

Finally, a turbidity current is generated due to the radial spread of the plume after its impingement. This turbidity current is shown and has been measured as a wall jet profile which decays as it advances due to shear stresses in the bed and further water entrainment. All these key physical processes and their interaction with each other can be summarized in the flowchart shown in Figure 5.2.
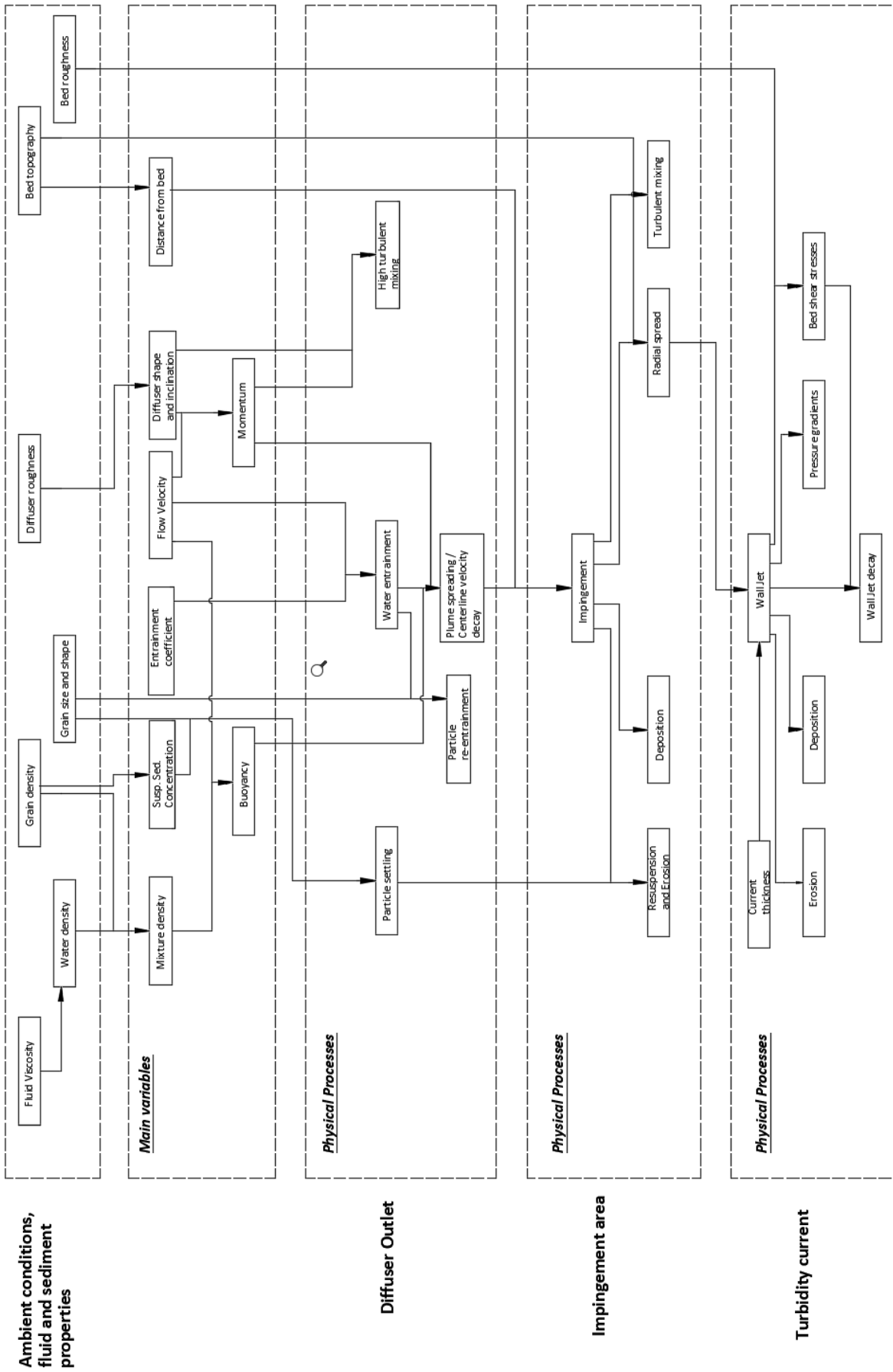
Figure 5.2: Key physical processes flowchart

5.3. Offset Jet Modelling

No dimensional analysis nor integral models that include all variables present during the experiments such as buoyancy, momentum, particle fallout, and bed distance were found. Therefore the ideal scenario is to use a CFD scheme to numerically solve the governing equations with a determined set of boundary conditions. This CFD model would allow determining the velocity and concentration fields for different locations and different outlet shapes, considering a turbulent model with certain entrainment assumptions. As argued in Chapter 2, this is often computationally expensive, and the correct model applications and interpretation may require substantial skill and experience. Therefore, due to time constraints, this is beyond the scope of this investigation, and available integral models have been used for comparisons purposes.

In this case, the approach that is used to predict the dispersion of the plume is by the integral jet model suggested by Lee and Chu(2003)[27]. This integral model is obtained by integrating the governing equations over the cross-section and jet trajectory by applying a boundary-layer approximation and using self-similarity properties. By doing so, this results in a system of equations for the characteristic variables (average centre-line velocity, concentration, jet width, and location) that have been described in Chapter 2.

Also, it is crucial to classify asymptotic flow regimes to be able to determine empirical coefficients such as the spreading coefficient (β) or the dilution coefficient (λ). These flow regimes are defined by the length scales which measure the importance of momentum to buoyancy, momentum to ambient flow or buoyancy to ambient flow. The Momentum-Buoyancy length scale does this classification. According to Papanicolau and List(1988)[44], flows behave like a jet for $z/L_m < 1$ and a plume for $5 > z/L_m$ and a transition zone in between. This can help resolve the differences in the experimental constants defined by other studies of jets and plumes.

Also, some dimensional analysis based on length scales can be used to try to determine the impingement area. According to experiments realized by Lee(2013)[28] for sediment-laden plumes, the maximum deposition is measured approximately at 0,94 l_m (Momentum-settling length scale). Since these experiments were conducted measuring the deposition in bins, no additional spreading of the material due to impingement can be foreseen. Therefore the area of the most amount of deposition is likely the impingement region.

Comparisons with experimental results and these integral models and dimensional analysis are further described below.

5.4. Dimensional Analysis

5.4.1. Jet to Plume Transition

As explained in Chapter 2, the jet to plume transition may be calculated by using a momentum-buoyancy length scale. Table 5.1 shows the calculation for this length scale for all diffusers for both concentrations that are tested in the visualization experiments. As shown in Section 2.2.5, the distance of transition between plume and jet that could be observed in the recorded images is measured. The momentum-buoyancy length scale is calculated with Equation 2.10.

Table 5.1 shows values for $1L_m$ and $5L_m$. According to Papanicolau and List(1988)[44] the measured values are the middle standing in a transition between plume and jet. It is also interesting to note that a plume-like behavior is expected to be reached at a distance after where the impingement takes place for all diffusers with low initial concentration.

Table 5.1: Jet to plume transition calculations

		Initial Concentration "C_{vo}" [%] = 1%			Initial Concentration "C_{vo}" [%] = 3%			
Water density	ρ_a	1000			1000			kg/m^3
Discharge density	ρ_0	1015,5			1049,5			kg/m^3
Specific gravity	g'	0,152			0,486			m/s^2

Jet transition distance	L_m	0,23	0,10	0,09	0,11	0,05	0,040	m
Plume transition distance	$5L_m$	1,15	0,52	0,44	0,53	0,24	0,2	m
Measured Jet to Plume transition		0,37	0,23	0,13	0,23	0,13	0,07	m

5.4.2. Impingement Points

Video imagery in Chapter 4 is used to approximate the plume's impingement point for both concentrations. It can be immediately seen that for a higher concentration impingement occurs closer to the diffuser. Table 5.2 and 5.3 show the particle settling velocity in still water and the respective momentum-settling length scale for all diffusers. According to the experiments that were conducted by Lee(2013)[28], the highest sedimentation is obtained at $\approx 0,94 l_m$. This can be inferred as the impingement point since the conducted experiments by Lee did not consider any particle displacement after they reached the table storing particles within a container as soon as they reached the bottom.

Table 5.2: Settling velocity for sediment d_{50}

d_{50}	95	microns
ν	1E-06	m^2/s
g	9,81	m/s^2
ρ_s	2,55	ton/m^3
ρ_a	1	ton/m^3
ω_a	0,0076	m/s

Table 5.3: Momentum-settling velocity length scales

		Slot	Vaned / Unvaned	
Initial Momentum	M_o	3,84E-04	9,60E-05	m^4/s^2
Sedimentiation length scale	l_m	2,57	1,29	m

This dimensional analysis is used to compare the approximately measured impingement points with the momentum-settling length scale. In all cases, the estimation obtained exceeded measurements by a factor of 2 or 3; therefore, this estimation is not considered suitable. A possible reason for this is that the length scale only considers momentum and does not include effects of density which by now we know that bends the plumes trajectory towards the bed or their experiments where carried out with very low concentration values.

5.5. Integral Modelling

5.5.1. Cross Sectional Velocity Profile

The vertical streamwise velocity profiles at various downstream locations for all diffusers has been shown in Figure 4.10. The transition of the profile from a Gaussian distribution to ultimately becoming a wall-jet type is clearly illustrated.

The self-similar property of buoyant jets in a still environment allows researchers to compare experimental and numerical results of plumes of different Q_0, M_0 and B_0. Therefore, the velocity profiles before the impingement points have been nondimensionalized as U/U_c versus $(y_c - y)/B_f$, and as $U = U_c$ versus $z/z_{uc/2}$ after the impingement points to see how measurements fit into a nondimensional distribution. The U_c is the maximum mean velocity magnitude at the vertical section, y_c is the corresponding coordinate of the maximum point, B_f the distance from the maximum point to the location where the velocity is e^{-1} of the maximum, and $z_{uc/2}$ is the distance from the bed to the point at the section at which $U = U_{c/2}$ and the velocity gradient is negative.

Figure 5.3 shows measurements for all profiles before the impingement point. This figure shows clearly how the fit into a gaussian distribution with small exceptions in Unvaned V1 and Slot V2. Since these two profiles are close to the impingement point, the velocity profile stretches out abandoning the gaussian profile.
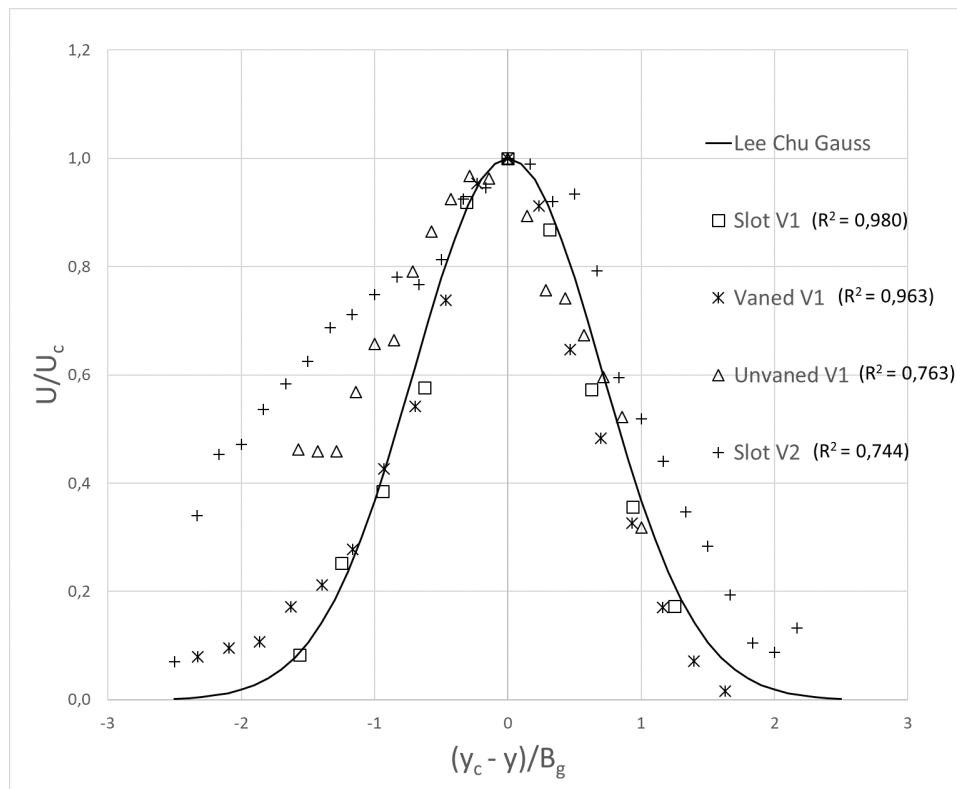

Figure 5.3: Nondimensionalized velocity profiles before impingement

Figure 5.4 shows measurements for all profiles after the impingement point. This figure shows how the distribution is more towards a Verhoff profile in agreement with Law and Herlina (2002)[22]. These profiles continue to diminish as the distance with the diffuser increases following what is discussed in Chapter 2.
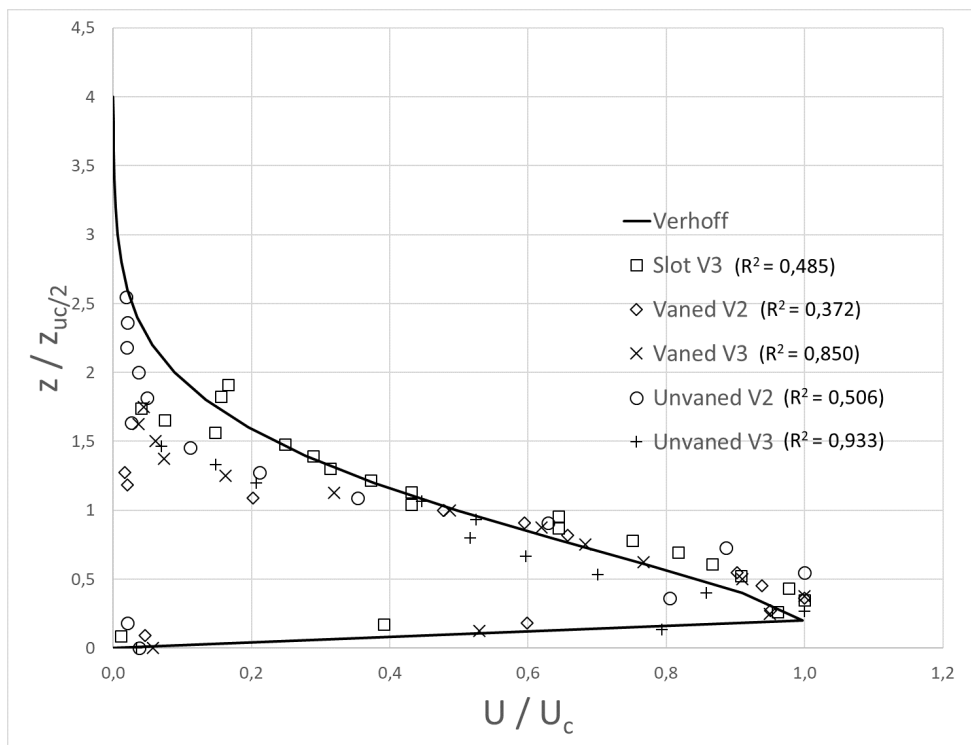

Figure 5.4: Nondimensionalized velocity profiles after impingement

5.5.2. Centerline Maxima Decay

It is well accepted that $U_c(x)$ in the zone of established flow (ZEF) of a submerged round and slot jet follows the x^{-1} decay (Fischer et al., 1979; Lee and Chu, 2003). The variation of the normalized centerline maximum (U_c/U_{max}) streamwise velocity component, with the normalized downstream distance (x/D) is presented in Figure 5.5. The decay is calculated according to the decay velocity profile in Lee and Chu (2003) shown in Equation 2.14.

The centerline velocity U_c in the zone of established flow (x=D > 6.2) shows good agreement for the slot diffuser at the first location. For the other diffusers, it approaches more the decay line found in Lee and Chu for a round jet. It is found that the centreline velocity of the offset jet decays much faster than free jet for the measured profiles.
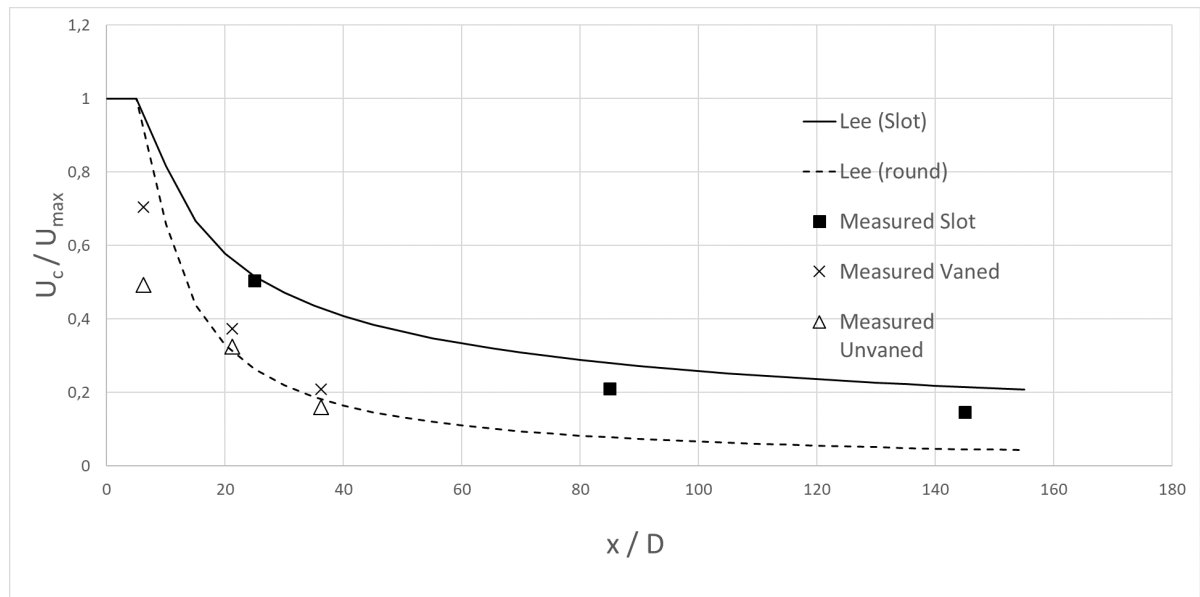
Figure 5.5: Maxima velocity decay

6

Conclusion and Recommendations

The consequences of a full-scale deep-sea mining operation on the ecosystem are still unknown. The primary concern is the disturbance and long-term unknown effects that these operations may have in the benthic layer by the generation of sediment plumes from the mining sediment wastes and other effluents (SWOE). This investigation is an example of how the industry is currently working on the design of equipment and mining processes for reducing the generated sediment plumes.

Horizontal particle-laden jets have received little attention from researchers over the years. Previous deep-mining studies have been concerned mostly with jets in a vertical direction. The behavior of particle motion in the turbulent jet flow can be quite different from the previous single-phase or vertical studies due to combined effects of gravity, resistance drag, and particle inertia acting in different directions. Despite its importance and wide application, there have been only a few studies of a horizontal buoyant jet laden with sediments; these studies are limited mainly to bed deposition measurements and have been designed mostly for round jets. There is no generally accepted theory for predicting the mixing of particle-laden water jets and insufficient data is available to verify and relate existing simplified jet integral models.

The main research objective shown in Chapter 1 is to provide a set of experimental data mainly for numerical model validation in a controlled environment at a small laboratory scale. For this purpose, a total of 19 experiments are carried out. Three different diffusers are tested using a single type of synthetic spherical glass particle, allowing to obtain valuable insight towards the plume's propagation and its dynamics after it impinged with the surface. Generated plume's near-field spreading is studied by using video imagery. Velocity and concentration profiles at the outlet and three different distances are successfully measured and are ready to validate IHC in house numerical models.

The most important parameter that was varied for the visualization experiments, was the initial concentration and the initial momentum for the different types of diffusers. Reducing the plume's initial momentum while maintaining its density difference reduces the transition from jet to plume, allowing for gentler deposition over the surface and resuspending less material. All experiments show similar behavior of an offset jet which transfers into a wall jet after its impingement.

It is important to mention that these results are based on scaled experiments and some uncertainties mainly about the quantification of the inlet density are present. Some differences between small scale and full-scale experiments may be perceivable due to the materials physical properties where no cohesion is present and where the roundness of the particles may tend to make them roll by their inertia. For these reasons, and the lack of ambient conditions, the full field-scale results could deviate; hence, similar work should be done full scale.

6.1. Ideal Diffuser Selection

To determine an ideal diffuser, first, it is necessary to determine what would be the ideal behavior of the plume. Having a close impingement does not necessarily indicate good behavior if the high momentum generates a large turbidity current that may spread further. Also, if external ambient conditions are considered, it may not necessarily be the case that a low velocity is ideal due to currents or the crawler movement being able to spread the plume faster.

For these specific experiments, the ideal plume behavior shall be to consider which plume settles closer to the origin, generates lower turbidity currents downstream and spreads the least amount possible to the sides. The measured velocity field is considered as a critical factor as well as the final deposition measurements to determine the selection of the optimal diffuser.

It is quite straight foward to determine that the generic Slot diffuser generates the worst outcome as was hypothesized from the beginning. Both visual experiments and velocity and concentration profiles show that the Slot has higher measurements in the near field and generates a broader spread of the plume once it impinges due to the high amount of momentum at which it leaves the diffuser. Also, the normalized deposition pattern shows it reaching lengths much larger compared to the other diffusers.

In a controlled experimental environment, the plume behaves best as it is diffused since it obtains lower values of momentum, thus having a faster transition to a plume behavior and allowing particles to settle faster. In the cases of the Vaned and Unvaned diffuser, the same area ratio has been used; thus, a very similar behavior is expected. The vanes primary purposes are to "guide" the flow and reduce energy losses that would, in turn, generate flow reversal causing an uneven velocity field and more of a time-dependant behaviour.

The velocity profiles, concentration profiles, and the deposition profile show a better behavior for the Unvaned diffuser. All measured profiles show lower values at all locations, and the normalized deposition profile shows that at the end of the experiment, most of the sediment deposits closer. These differences may be attributed to the loss in the cross-section due to the vanes giving a higher diffusion to the Unvaned diffuser. However, there is a possibility that differences due to scaling factors may have to be considered in these experiments. At higher Froude numbers, the absence of vanes may significantly modify the behavior of the plume, making it more turbulent and time-dependant having adverse effects on the plume's spread. Therefore, taking all these considerations, the Vaned diffuser is considered as the optimum condition for the nodule collector's outlet.

It is wishful that these experimental results can provide usefull data as reference for this environmental issue, and support the development and validation of future numerical models concerned with the turbulent transport of mass and momentum offset jets for different diffuser shapes. Based on the analysis of obtained results for all conducted experiments the following conclusions and recommendations have been made below.

6.2. Conclusions

The contributions and findings to the study of horizontal sediment plumes for the deep-sea mining nodule collector are as follows:

- The behavior of the plume is that of a well-studied offset jet that experiences some particle fallout during its jet phase before impingement. For horizontal jets sufficiently far from the seabed, the jet behaves as a free jet initially, then substantial entrainment can take place before the jet impacts on the seabed due to the negative buoyancy. Ultimately, the flow becomes a wall jet or weak wall plume, depending on the decaying of the velocity and concentration along the way.

- Self-similarity of the velocity profiles was studied. It is found that the cross-sectional velocity component profiles at various downstream locations followed the transition from an axisymmetric Gaussian, to an asymmetric Gaussian with a much wider lower spread, and finally to the wall-jet pattern for all diffusers.

- For higher concentrations such as those studied in the visualization experiments, the settling of particles is observed to drag the jet to spread with a downward-bending mean trajectory forcing a sooner impingement compared to the lower concentration scenarios in all reviewed cases.

- Reviewed literature suggests that different spread angles for the jet can define the lateral extent of the sediment fallout region. However, it is observed that after impingement, the jet spreads radially in all directions.

- Lowering the momentum of the jet by diffusing the outlet gave better results in terms of drawing the impingement point and the deposition profiles nearer to the diffuser. Also, the measured velocity and concentration profiles considerably decreased.

- The Unvaned diffuser gives better overall performance out of the tested diffusers. However, this may be attributable to scaling law factors. In full scale, it may be possible to observe flow separation and a more time-dependent behavior if no vanes are present; therefore, the Vaned diffuser is considered the optimal choice.

- Integral models of free jets are similar in the jet and the transition region and may be viewed as a fair approximation; however, after impingement, the profiles do not follow the free jet theory. Therefore CFD modeling should be applied for each diffuser to determine the near-field spreading of horizontal plumes and their velocity and concentration decay.

6.3. Recommendations

Based on the present study, the following suggestions are recommended for future research.

- Glass bead particles are chosen based on their size, availability, narrow particle size distribution, easy handling and based on the size of the existing setup. However, this material differs substantially from the actual sediment that is found on the ocean floor. Its shape and non-cohesive properties suggest that results may vary due to possible flocculation or particle locking present in the actual sediment. Therefore it is recommended to carry out the next experiments with a cohesive and non-spherical material.

- Many environmental conditions are neglected due to the simplification of the experiments. Both ambient currents and the collector movement is bound to affect the behavior of the plume. A recommendation is to include movement within the basin to simulate these ambient currents for further experiments.

- LED lights used for improving the contrast in the plume during the visualization experiments were visible during the top view analysis. It is recommended to find an alternative to diffuse this light homogeneously through the table.

- In this study, only the final diffuser shapes have been varied. A recommendation for future studies is to include a possible inclination angle or a height variation for the diffuser as well. An inclination upwards

may stretch the plume's trajectory allowing for more water entrainment, reducing the momentum at the impingement point. It is also possible that an inclination towards the bed may generate the plume to settle closer to the diffuser.
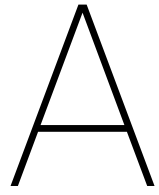
- The experimental setup used in this investigation left some uncertainties whether the mixing of the sediment is homogenous inside the mixing tank. A recommendation for further experiments would be to use more than 2 mixing pumps and reduce the height of the mixing tank. Another alternative is to change the mixing process into a particle feeder such as the hourglass used in Lee (2013).

- The turbidity sensors that are employed seem to have a more robust offshore purpose and do not seem ideal for a small-scale scenario. A recommendation is to investigate alternatives to measure the concentration profiles for future experiments. A measuring technique called Planar Concentration Analysis (PCA) or Planar Laser-Induced Fluorescence (PLIF) presents a non-intrusive method that allows evaluating the depth-averaged concentration and has been used successfully in other experiments.

- Measurements for the velocity profiles are done every 3 cm however the accuracy of the measurements at the edges of a profile is lower than that in the center; therefore, it is recommended to overlap future measurements and space them every 1.5 cm.

References

[1] Nautilus Minerals (2016b). How it will all work. *http://www.nautilusminerals.com/irm/content/seafloor-production-tools.aspx?RID=333 (Accesed Janurary 2019)*, Nov 2016.

[2] M.L. Albertson, Y.B. Dai, R.A. Jensen, and H. Rouse. Diffusion of submerged jets. *Transactions of the American Society of Civil Engineers*, (115):639–664, 1950.

[3] T. Bleninger. *Sedimentation in Particle-Laden-Jets.* PhD thesis, Institute for Hydromechanics, University of Karlsruhe, Germany, 2000.

[4] C. Bourque and B.G. Newman. Reattachment of a twodimensional, incompressible jet to an adjacent flat plate. *The Aeronautical Journal*, (11(3)):59–84, 1960.

[5] N.H. Brooks. Dispersion in hydrologic and coastal environments. Technical report, Report No. KH-R-29, W. M. Keck Lab. of Hydraulics and Water Resources, Pasadena, California, 1972.

[6] P. Byishimo. Experiments and 3d cfd simulations of deep-sea mining plume dispersion and seabed interactions. Master's thesis, TU Delft, The Netherlands, 2018.

[7] G.M. Carlomagno and A. Ianiro. Thermo-fluid-dynamics of submerged jets impinging at short nozzle-to-plate distance: A review. *Experimental Thermal and Fluid Science*, (58):15–35, 2014.

[8] S.N. Chan, K.W.Y. Lee, and J.H.W. Lee. Numerical modelling of horizontal sediment-laden jets. *Environmental Fluid Mechanics*, (14):173–200, 2014.

[9] A.T. Crowe. *Inclined Negatively Buoyant Jets and Boundary Interaction.* PhD thesis, University of Canterbury, New Zealand, 2013.

[10] B. Cushman-Roisin. *Environmental Fluid Mechanics.* John Wiley Sons, Inc., 2019.

[11] A.J.S. Cuthbertson, D.D. Apsley, P.A. Davies, Lipari G., and Stansby P.K. Deposition from particle-laden, plane, turbulent, buoyant jets. *Journal of Hydraulic Engineering*, (134(8)):1110–1122, 2008.

[12] S. Dey, G.R. Kishore, C. Castro-Orgaz, and S.Z. Ali. Hydrodynamics of submerged turbulent plane offset jets. *Physics of Fluids*, (29), 2017.

[13] ECORYS. Study to investigate state of knowledge of deep sea mining. Technical report, 2014.

[14] G.G.J. Ernst, R.S.J. Sparks, S.N. Carey, and M.I. Bursik. Sedimentation from turbulent jets and plumes. *Journal of Geophysical Research*, (101):5575–5589, 1996.

[15] L.N. Fan and N.H. Brooks. Numerical solutions of turbulent buoyant jet problems. Technical report, Report No. KH-R-18, W. M. Keck Laboratory, California Institute of Technology, Pasadena, California, 1969.

[16] H.B. Fischer, J. Imberger, E.J. List, and N.H. Brook. *Mixing in Inland Coastal Waters.* Academic Press, 1979.

[17] F. Grunsven, G. Keetels, and C. Rhee. The initial spreading of turbidity plumes – dedicated laboratory experiments for model validation. In *Deep-Sea Mining: Challenges of Going Further and Deeper Advances in Marine Research and Subsea Technology Beyond Oil Gas.* UMC 2018, 2018.

[18] R. Gu. Modeling two-dimensional turbulent offset jets. *Journal of Hydraulic Engineering*, (112(11)): 617–624, 1996.

[19] P. Halbach, G. Friedrich, and U. von Stackelberg. *The Manganese nodule belt of the Pacific Ocean: geological environment, nodule formation, and mining aspects.* F. Enke, 1988. ISBN 3432963815.

[20] J. Hein, A. Koschinsky, and T. Conrad. Deep-ocean mineral deposits as a source of critical metals for high- and green-technology applications: comparison with land-based resources. *Ore Geology Reviews*, (51):1–14, 2013.

[21] J.R. Hein. Manganese nodules. *Encyclopedia of Marine Geosciences*, pages 408–412, 2016.

[22] A. Herlina and W.K. Law. An experimental study on turbulent circular wall jets. *Journal of Hydraulic Engineering*, (128):161–174, 2002.

[23] J. Hoch and L.M. Jiji. Two-dimensional turbulent offset jet-boundary interaction. *Experimental Thermal and Fluid Science*, (103):154–161, 1981.

[24] G.H. Jirka. Integral model for turbulent buoyant jets in unbounded stratified flows. part i: Single round jet. *Environmental Fluid Mechanics*, (4:1):1–56, 2004.

[25] G. Kishore and S. Dey. Hydraulics of submerged offset-jets. *Hydraulic Structures and Water System Management. 6th IAHR International Symposium on Hydraulic Structures*, pages 407–416, 2016.

[26] G.F. Lane-Serff and T.J. Moran. Sedimentation from buoyant jets. *Journal of Hydraulic Engineering*, (131(3)):166–174, 2005.

[27] J. Lee and V. Chu. *Turbulent jets and plumes - A Lagrangian Approach*. Kluwer Academic Publishers, 2003.

[28] W.Y. Lee, A.C.Y. Li, and J.H.W. Lee. Structure of a horizontal sediment-laden momentum jet. *Journal of Hydraulic Engineering*, (139(2)):124–140, 2013.

[29] E.J. List. Mechanics of turbulent buoyant jets and plumes. *HMT: the Science Applications of Heat and Mass Transfer. Reports, Reviews Computer Programs*, pages 1–68, 1982.

[30] P. Liu and K.M. Lam. Two-phase velocity measurement in a particle-laden jet. *Journal of Hydro-environment Research*, (7):18–29, 2013.

[31] Ultrasonic Flow Management). Katflow 200 operating instructions. *https://www.u-f-m.nl/wp-content/uploads/2014/09/UFM_manual_KAT flow − 200_E Nc omp.pd f (Accesed Jul y2019)*, 2014.

[32] Nortek Manuals. *The comprehensive manual for velocimeters*. Nortek AS, 2018.

[33] D. S. Miller. *Internal Flow Systems*. Mentor Graphics Corporation, 2014.

[34] K.A. Miller, Thompson K.F., P. Johnston, and D. Santillo. An overview of seabed mining including the current state of development, environmental impacts, and knowledge gaps. *Frontiers in Marine Science 4:418.*, 4(418), 2018.

[35] Blue Mining. Public report blue mining: Breakthrough solutions for mineral extraction and processing in extreme environments. Technical report, 2015.

[36] Royal IHC Mining. Reflections on deep sea mining development: More than technology alone. In *IMAM Conference*, 2017.

[37] Royal IHC Mining. Into the blue. *Insight*, (E11):20–23, 2018.

[38] B.R. Morton, G.I. Taylor, , and J.S. Turner. Turbulent gravitational convection from maintained and instantaneous sources. *Proceedings of the Royal Society of London*, (A234):1–23, 1956.

[39] M. Navarre, H. Lammens, and ESG Analysis. Opportunities of deep-sea mining and esg risks. *Amundi Discussion Papers Series*, (DP-24-2017), 2017.

[40] M. Neves, A. Neves, and T. Bleninger. Prediction on particle deposition in effluent disposal system. *Proc. 2nd Int. Conf. Marine Waste Water Discharges*, 2002.

[41] M.J. Neves and H.J.S. Fernando. Sedimentation of particles from jets discharged by ocean outfalls: a theoretical and laboratory study. *Water Science Technology*, (32(2)):133–139, 1995.

[42] H. Niner, J. Ardron, E. Escobar, M. Gianni, A. Jaeckel, D. Jones, L. Levin, C. Smith, T. Thiele, P. Turner, C. Van Dover, L. Watling, and Gjerde K. Deep-sea mining with no net loss of biodiversity—an impossible aim. *Frontier of Marine Science*, (5:53), 2018.

[43] P. Palomar, J.L. Lara, I. Losada, M. Rodrigo, and A. Alvarez. Near field brine discharge modelling. part 1: Analysis of commercial tools. *Desalination*, (290):14–27, 2012.

[44] P. Papanicolaou and E. List. Investigations of round vertical turbulent buoyant jets. *Journal of Fluid Mechanics*, (195):341–391, 1988.

[45] J.R.R. Pelfrey and J.A. Liburdy. Mean flow characteristics of a turbulent offset jet. *Journal of Fluids Engineering*, (108(1)):82–88, 1986.

[46] N. Rajaratnam and K. Subramanya. Plane turbulent reattached wall jets. *Journal of the Hydraulics Division*, (94):95–112, 1968.

[47] L.R. Reneau, J.P. Johnston, and S.J. Kline. Performance and design of straight, two dimensional diffusers. *Journal of Basic Engineering*, (89(1)):141–150, 1967.

[48] C.v. Rhee. *On the sedimentation process in a Trailing Suction Hopper Dredger*. PhD thesis, Delft University of Technology, Netherlands, 2002.

[49] P.J.W. Roberts. Turbulent entrainment: The development of the entrainment assumption, and its application to geophysical flows. *Handbook of Environmental Fluid Dynamics, Volume Two,*, pages 229–241, 2013.

[50] R. Sawyer. The flow due to a two-dimensional jet issuing parallel to a flat plate. *Journal of Fluid Mechanics*, (9(4)):543–559, 1960.

[51] D. Shao. *Desalination discharge in shallow waters*. PhD thesis, Nanyang Technological University, Singapore, 2010.

[52] D. Shao and A.W. Law. Boundary impingement and attachment of horizontal offset dense jets. *Journal of Hydro-environment Research*, (5):15–24, 2011.

[53] R.J. Sobey, A.J. Johnston, and R.D. Keane. Horizontal round buoyant jet in shallow water. *Journal of Hydraulic Engineering*, (114(8)):910–929, 1988.

[54] K. R. Sreenivas and A. K. Prasad. Vortex-dynamics model for entrainment in jets and plumes. *Physics of Fluids*, (12):2101–2107, 2000.

[55] K. Svatikova, M. de Ridder, N. Olah, and Hans Bolscher. Deep sea mining: Hitting the bottom or taking off? Technical report, Center of Expertise on Resources, 2015.

[56] J. Turner. Turbulent entrainment: The development of the entrainment assumption, and its application to geophysical flows. *Journal of Fluid Mechanics*, (173):431–471, 1986.

[57] UNCLOS. United nations convention on the law of the sea. 1982.

[58] C. Van Dover, J. Ardron, and E. Escoabar. Biodiversity loss of deep-sea mining. *Nature Geoscience*, 2017.

[59] F.M. White. *Fluid Mechanics, Seventh Edition*. McGraw-Hill, 2009.

[60] S.H. Yoon, K.C. Kim, and D.S. Kim. Mean flow characteristics of a turbulent offset jet. *KSME Journal*, (7(2)):101–112, 1993.

A

Inlet Conditions

A.1. Inlet Flow Velocity - Time Series Graphs

(a) Profile 0 (2)

(b) Profile 1

(c) Profile 1 (2)

(d) Profile 2

(e) Profile 3

(f) Visual 1

(g) Visual 3
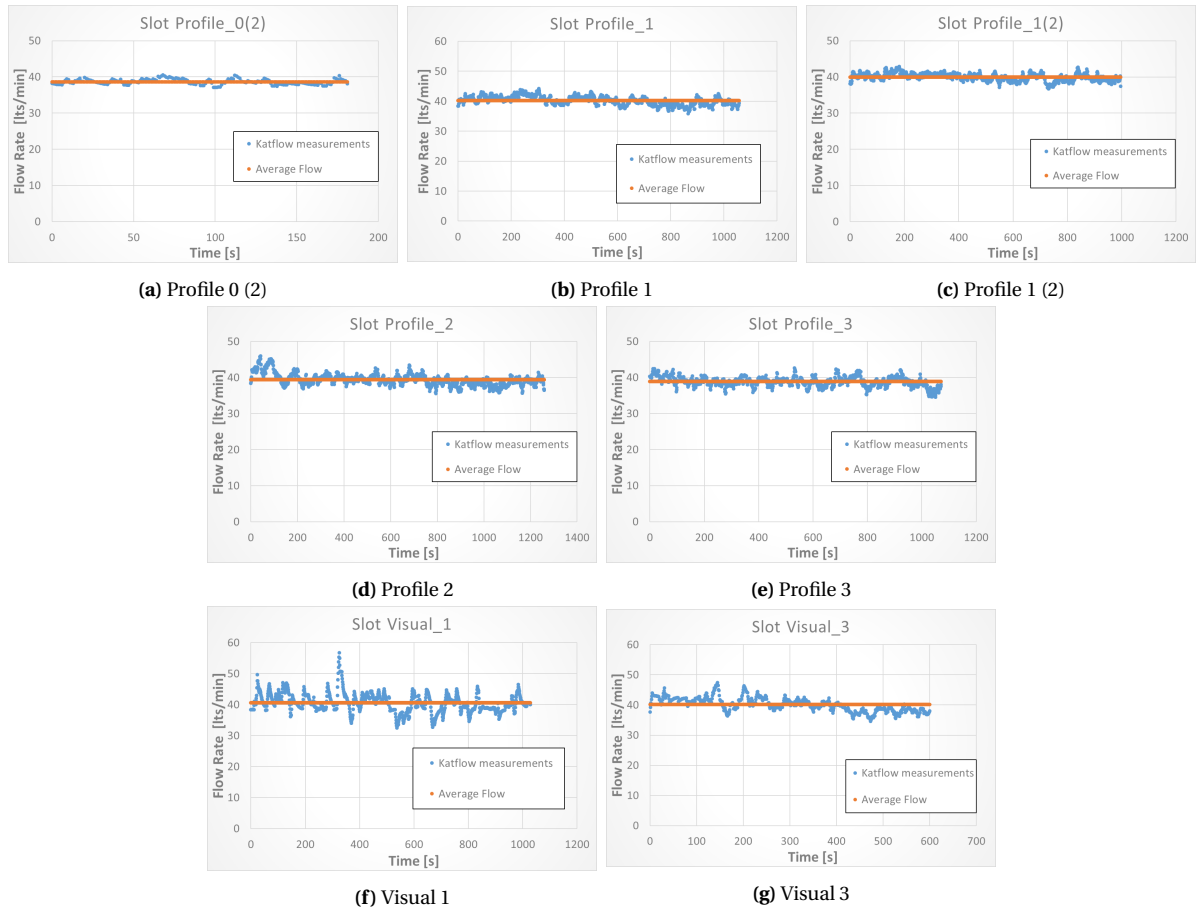
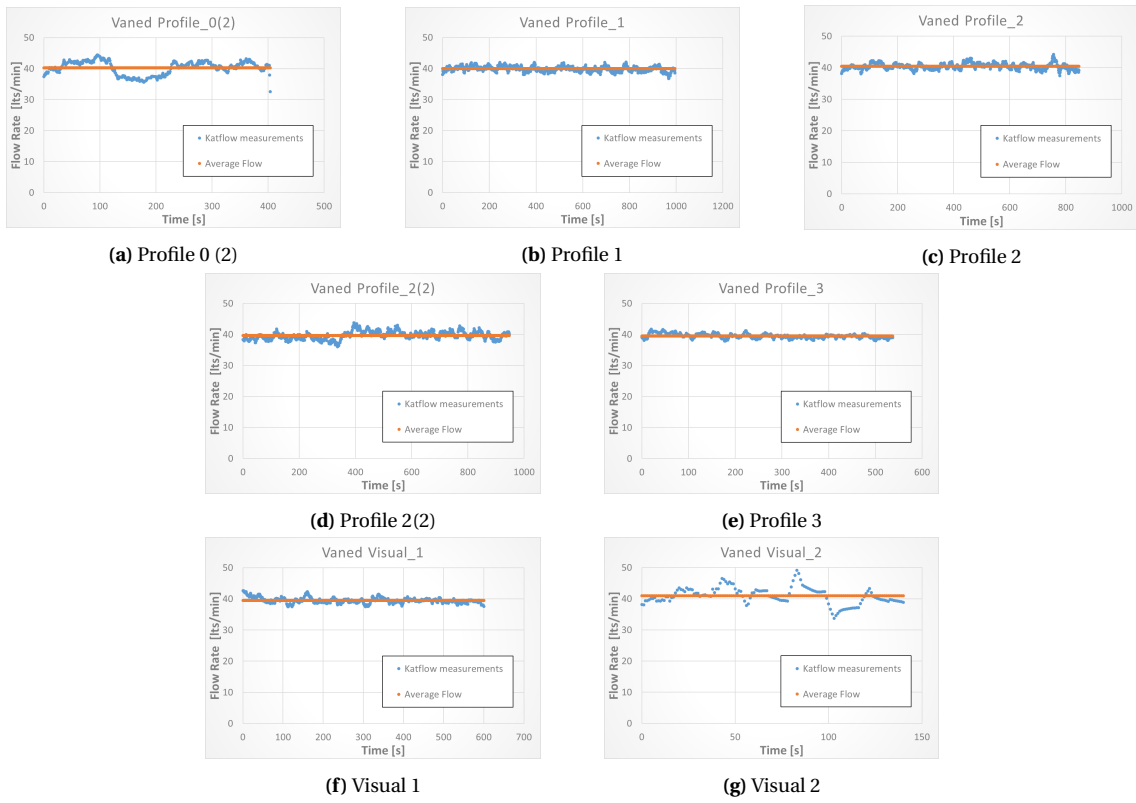**Figure A.1:** Flowmeter time series for Slot diffuser
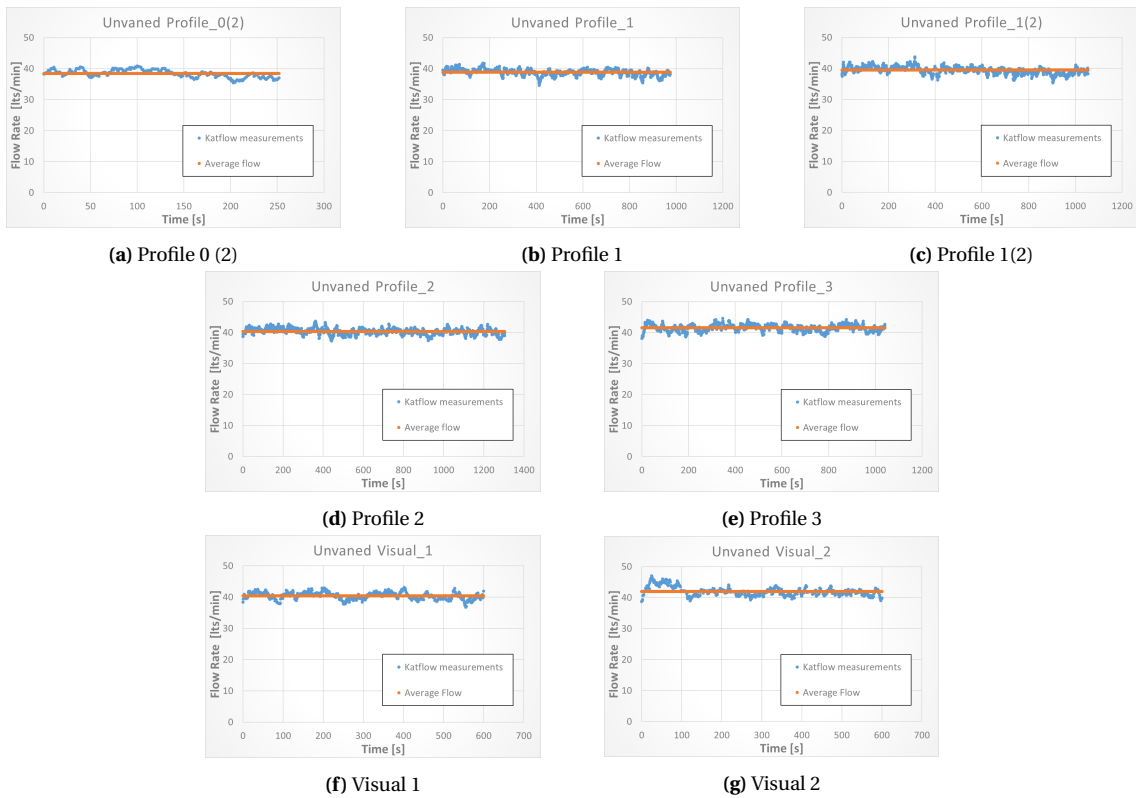
Figure A.2: Flowmeter time series for Vaned diffuser

Figure A.3: Flowmeter time series for Unvaned diffuser
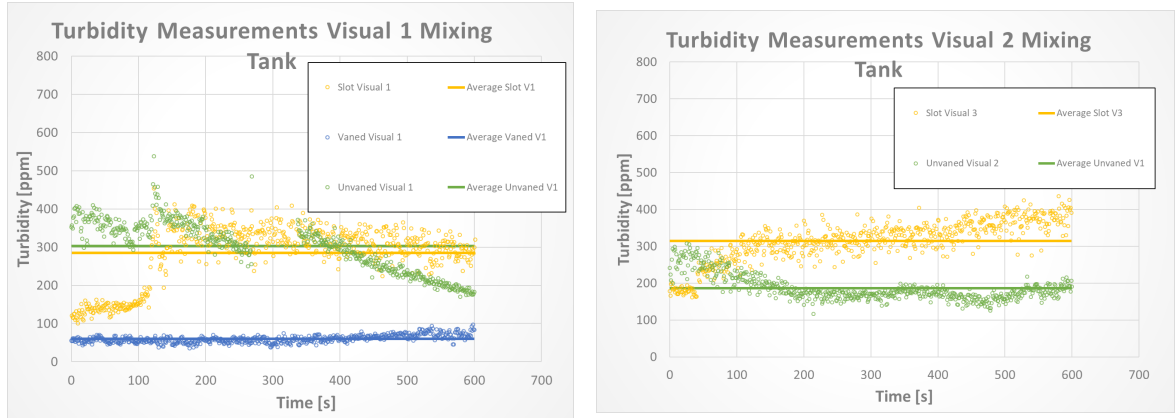
A.2. Inlet SSC - Time Series Graphs

Figure A.4: Turbidity measurements in mixing tank Visual experiments
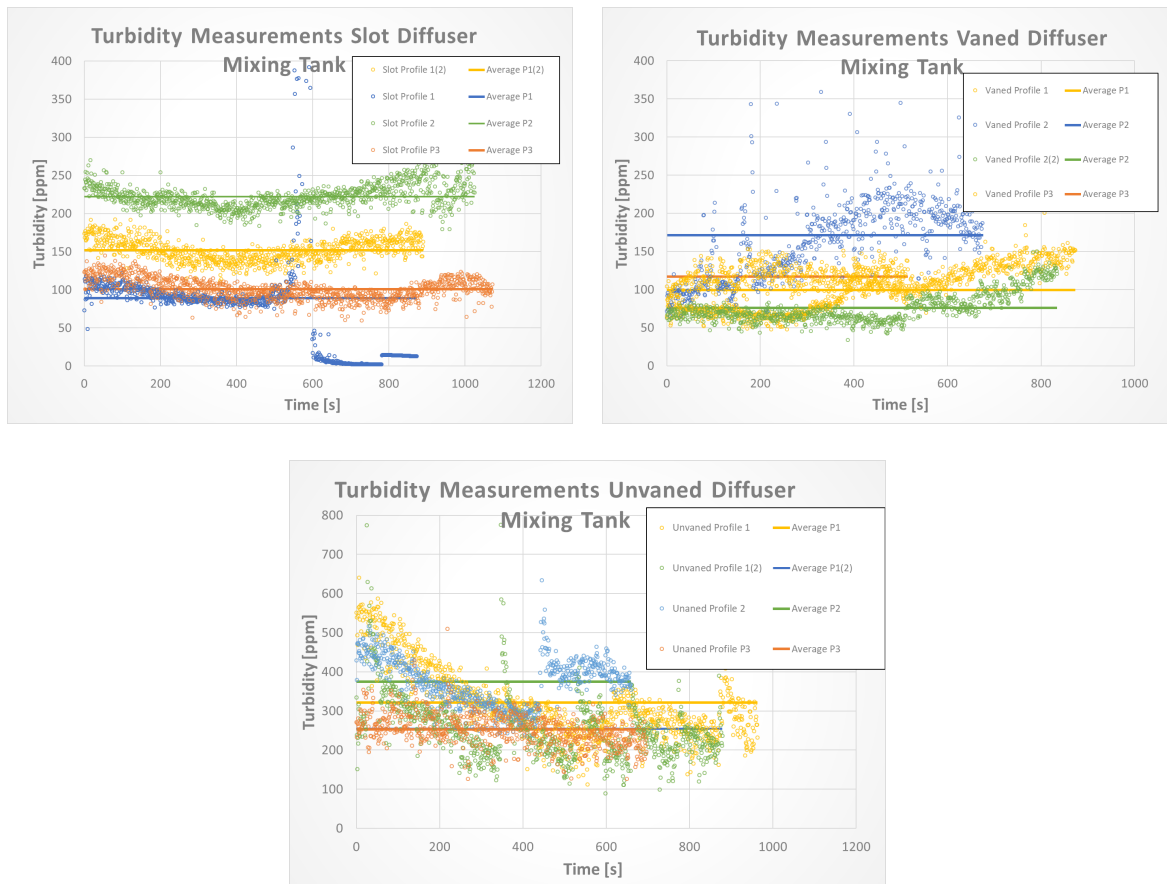
Figure A.5: Turbidity measurements in mixing tank for Concentration profiles

B

Video Imagery Results

B.1. Top Contour Images

(a) 120 s

(b) 240 s

(c) 360 s

(d) 480 s

(e) 600 s
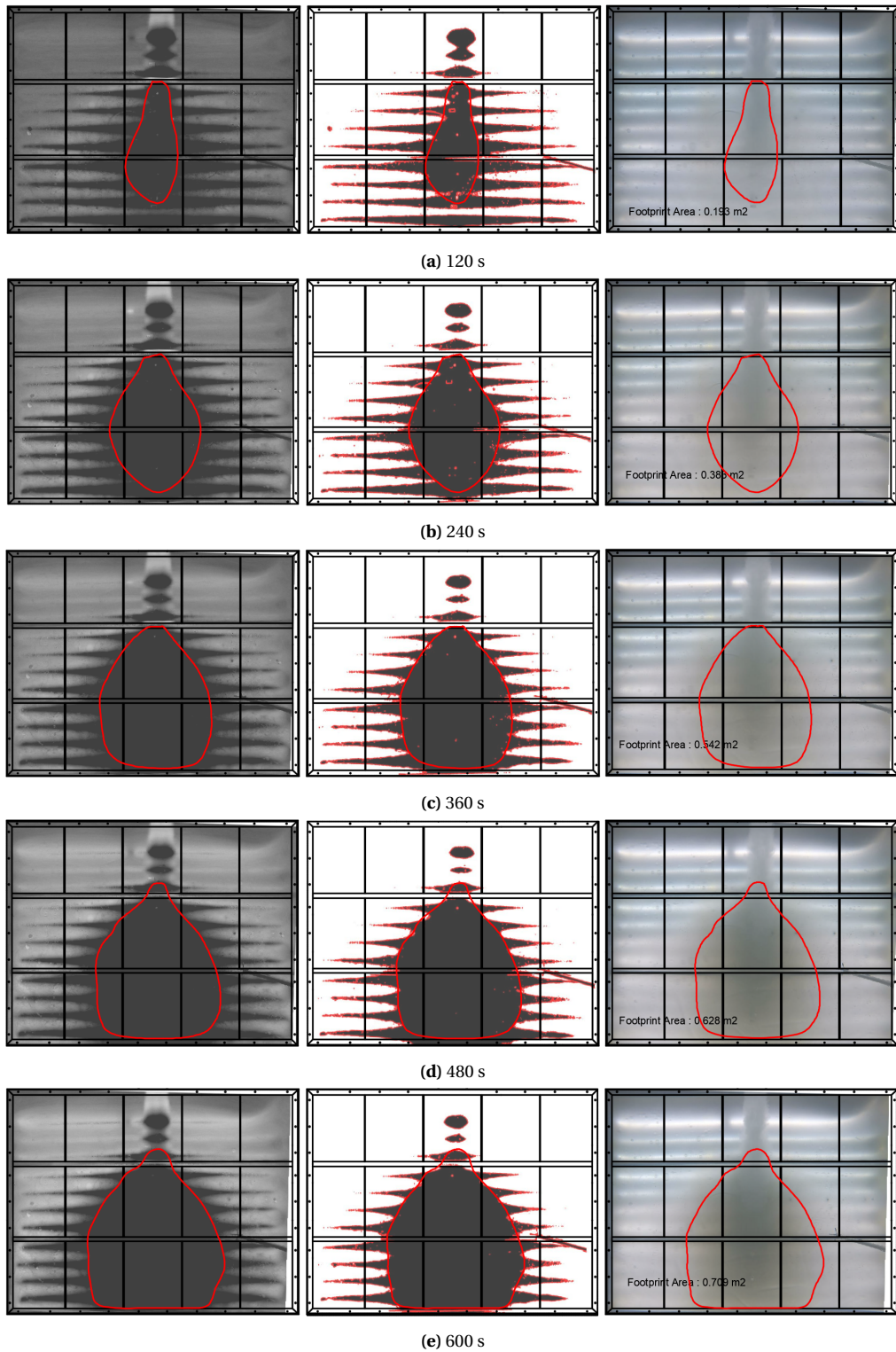
Figure B.1: Top View contours Slot diffuser low concentration

(a) 120 s

(b) 240 s

(c) 360 s

(d) 480 s

(e) 600 s
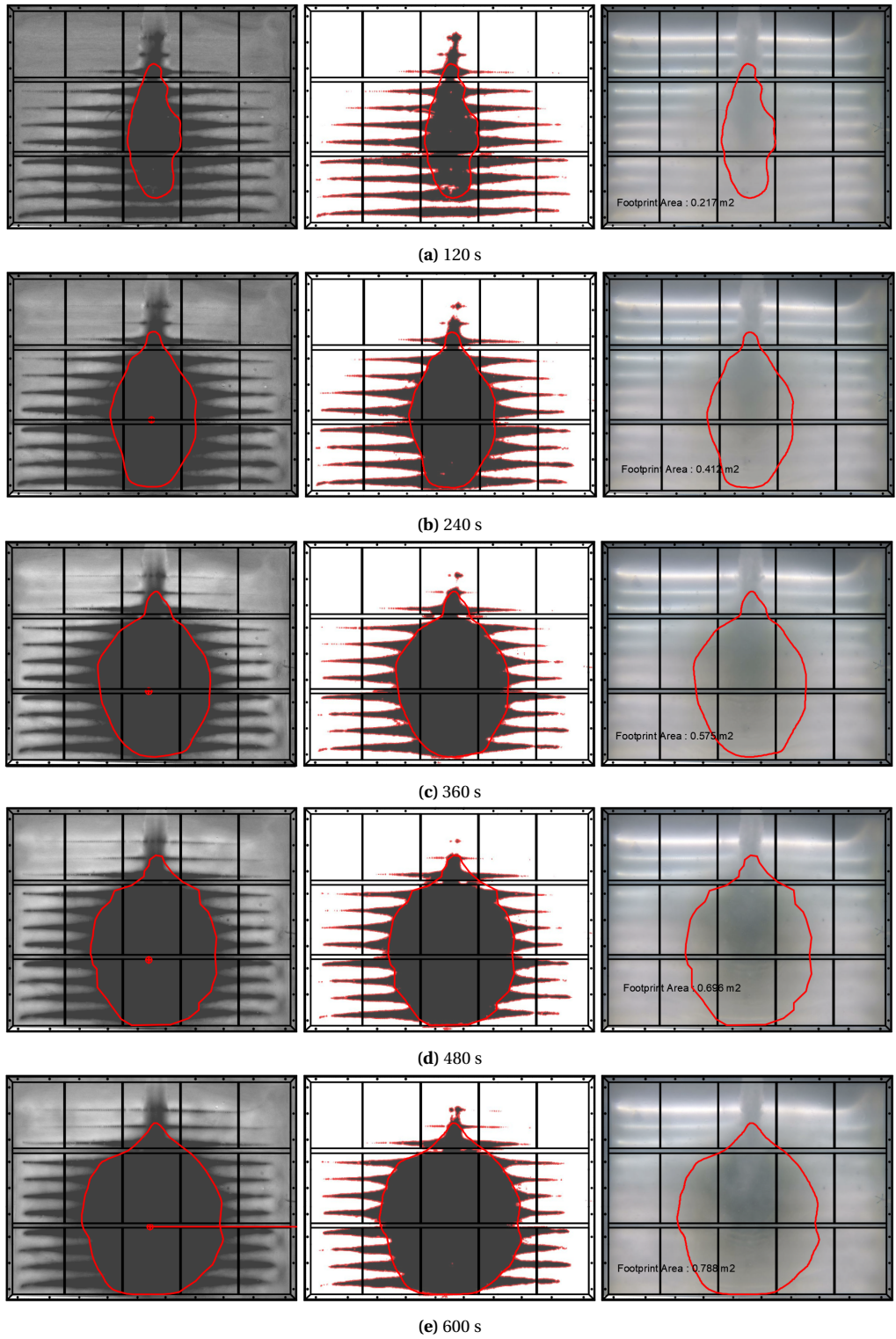
Figure B.2: Top View contours Slot diffuser high concentration

(**a**) 120 s

(**b**) 240 s

(**c**) 360 s

(**d**) 480 s

(**e**) 600 s
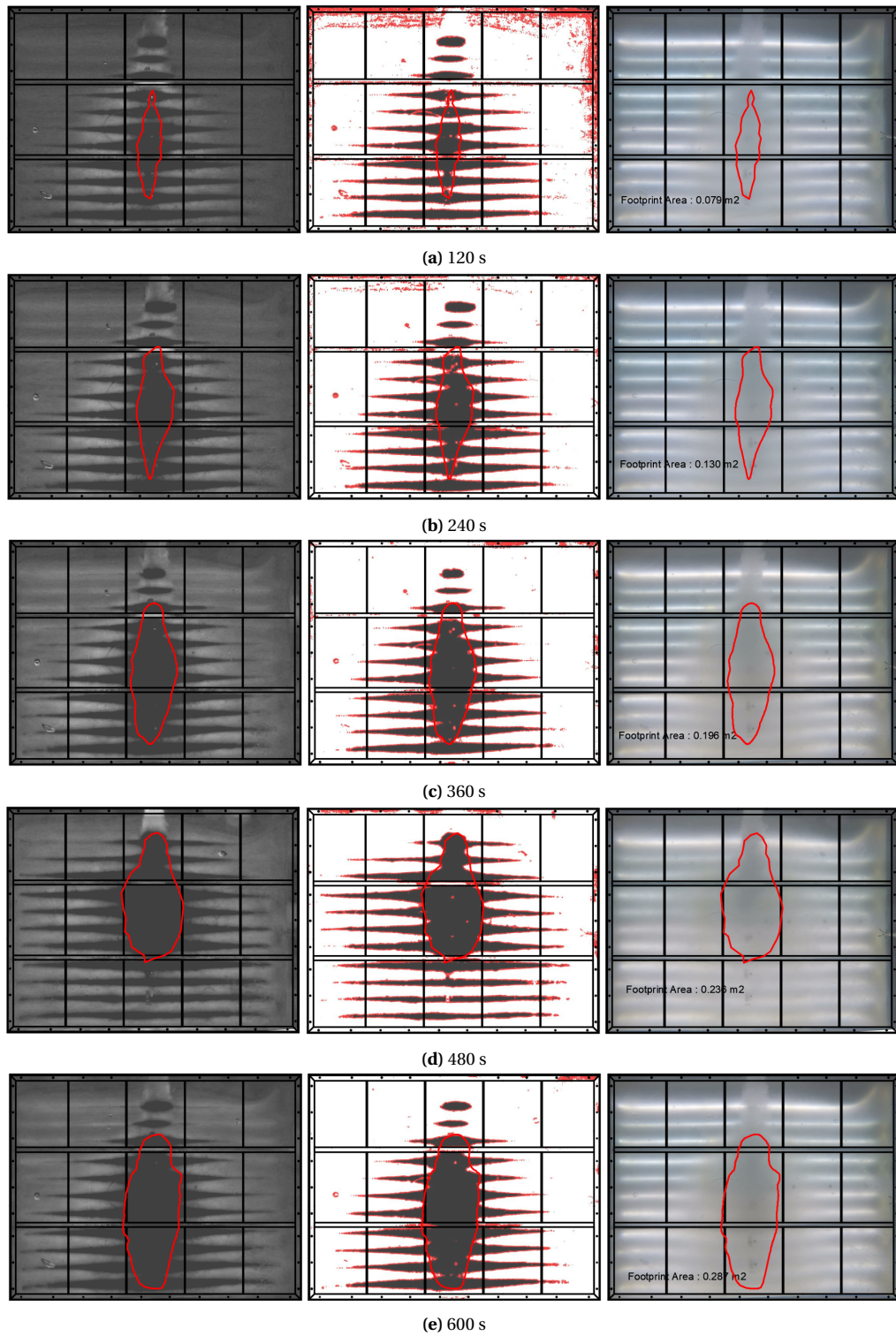
Figure B.3: Top View contours Vaned diffuser low concentration

(a) 120 s

(b) 240 s

(c) 360 s

(d) 480 s

(e) 600 s
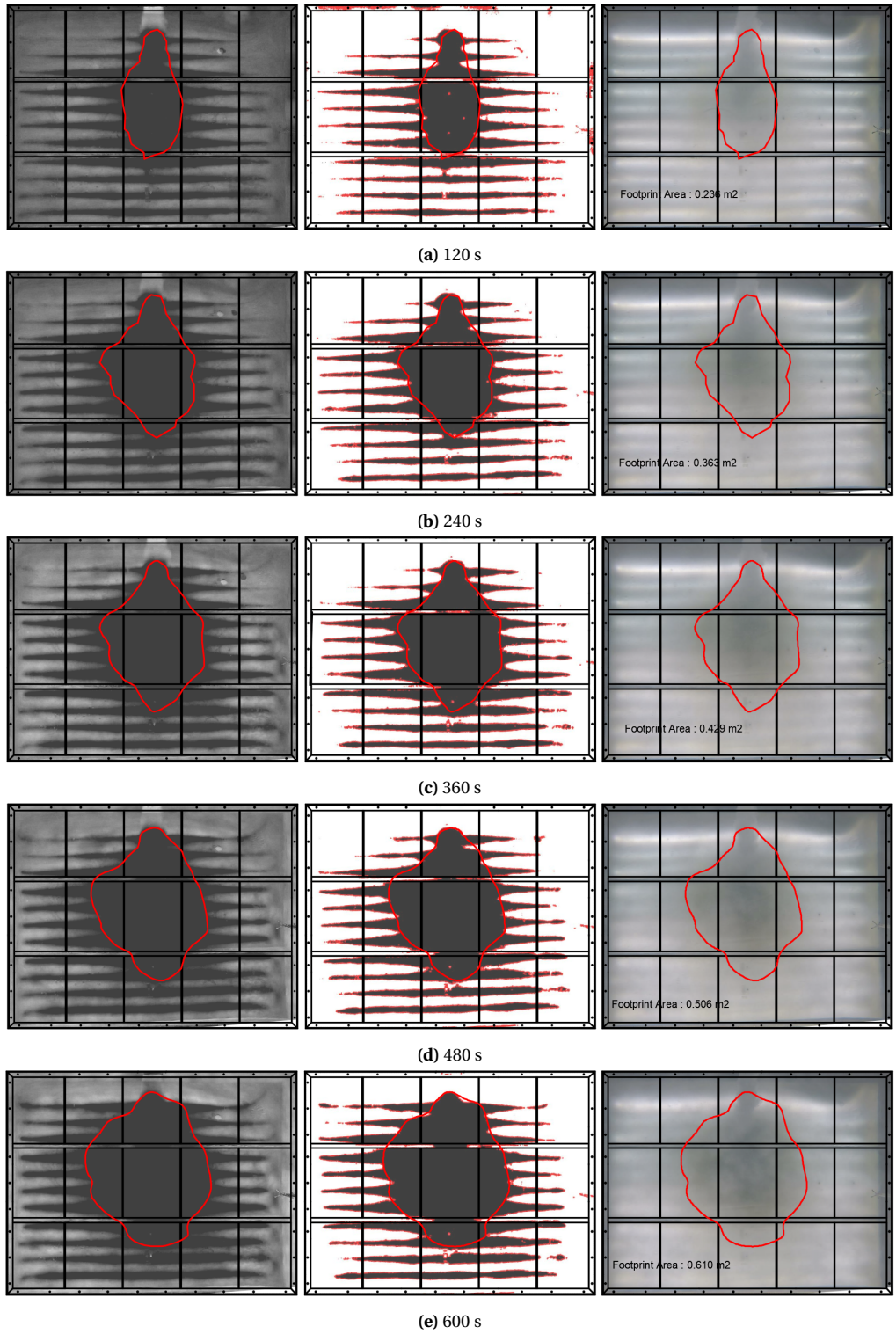
Figure B.4: Top View contours Vaned diffuser high concentration

(a) 120 s

(b) 240 s

(c) 360 s

(d) 480 s

(e) 600 s
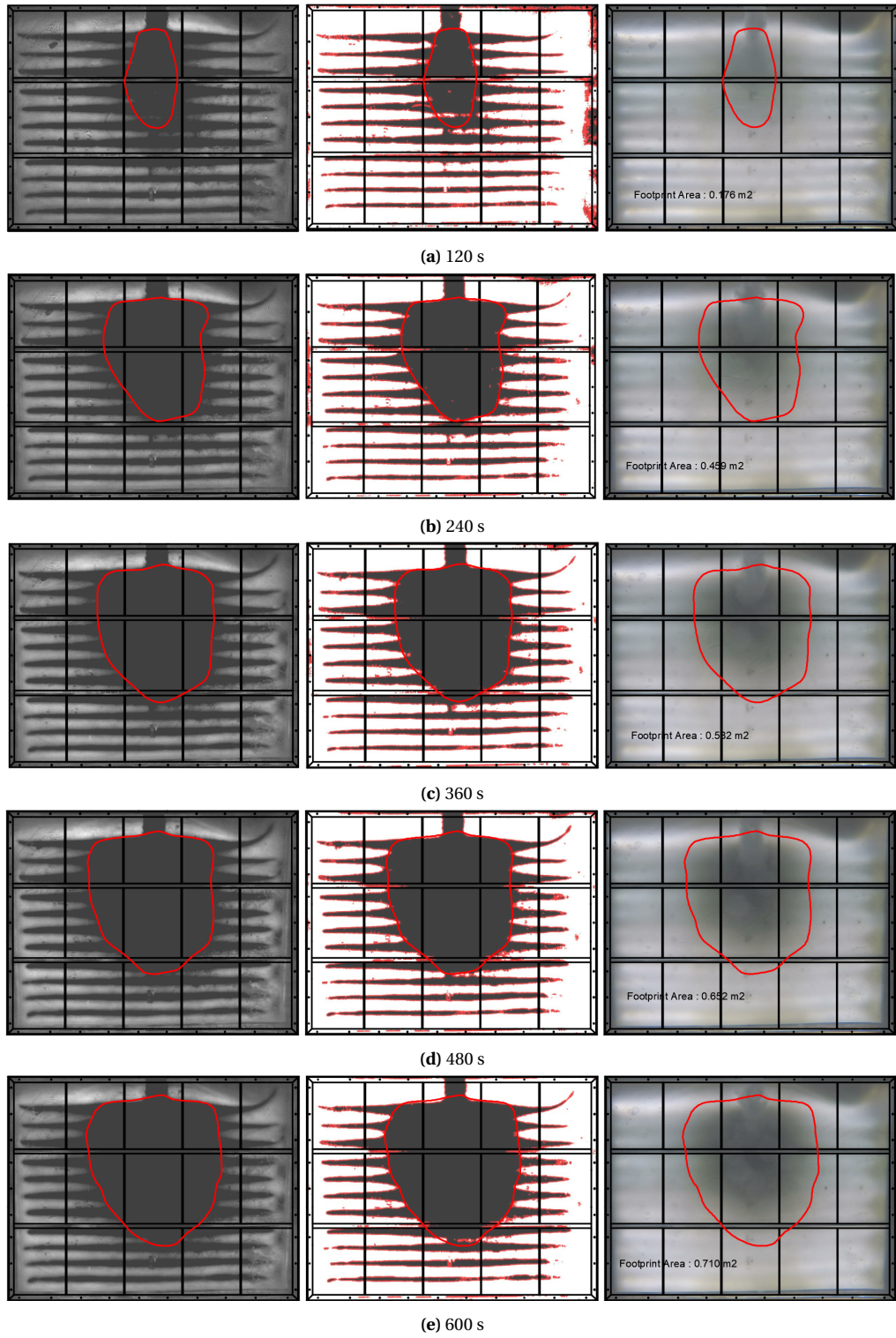
Figure B.5: Top View contours Unvaned diffuser low concentration

(a) 120 s

(b) 240 s

(c) 360 s

(d) 480 s

(e) 600 s
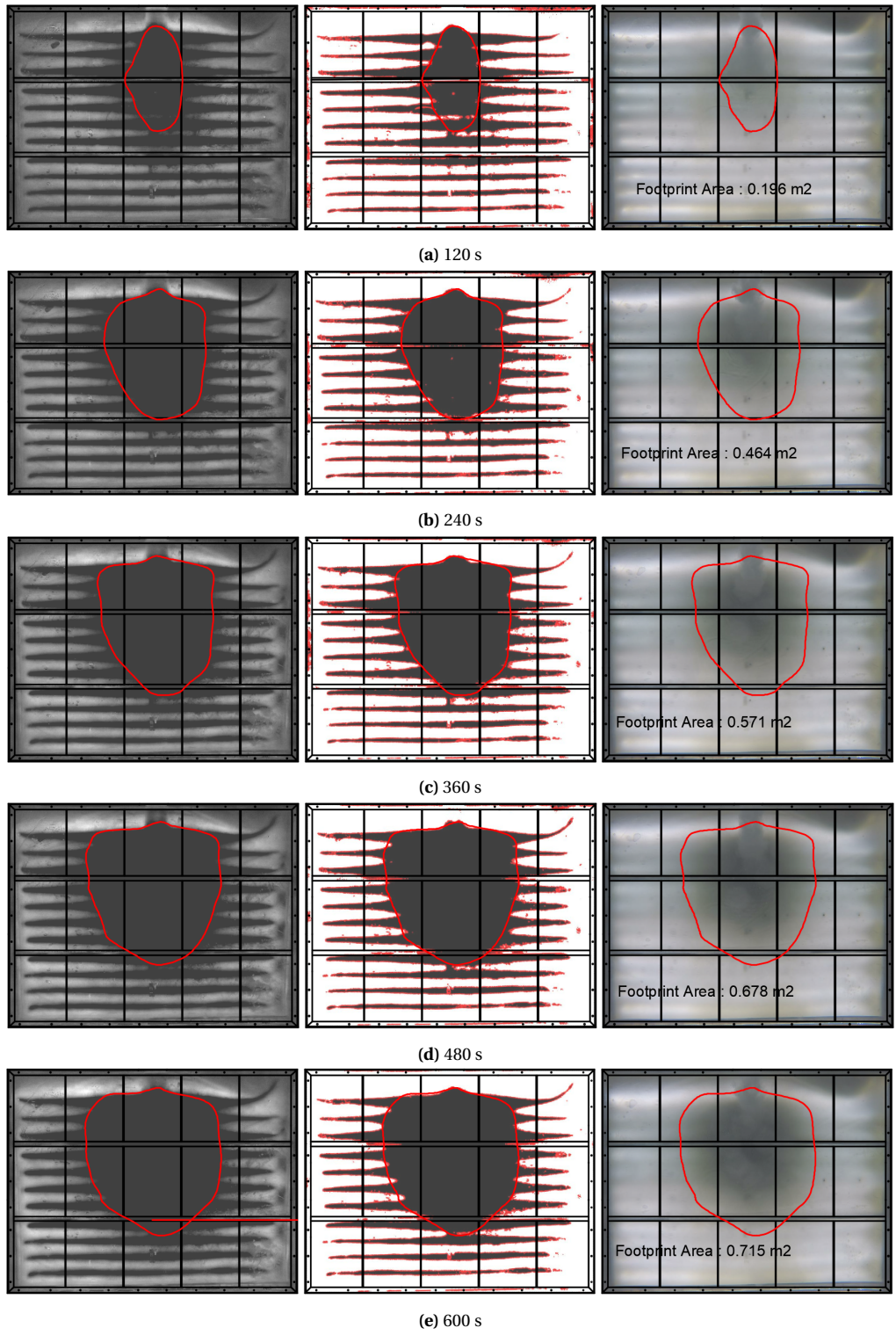
Figure B.6: Top View contours Unvaned diffuser high concentration

B.2. Front Velocity - Time Series Graphs
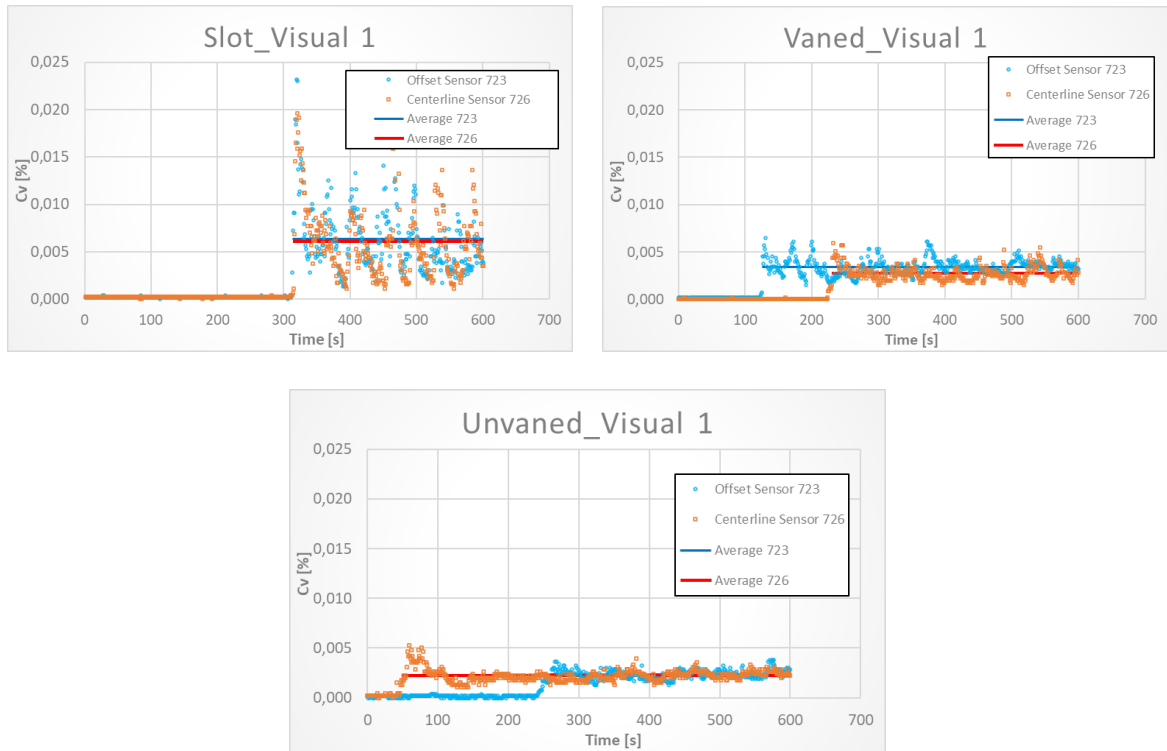
Figure B.7: Offset and centerline OBS sensor concentration-time series (Cvo = 1%)
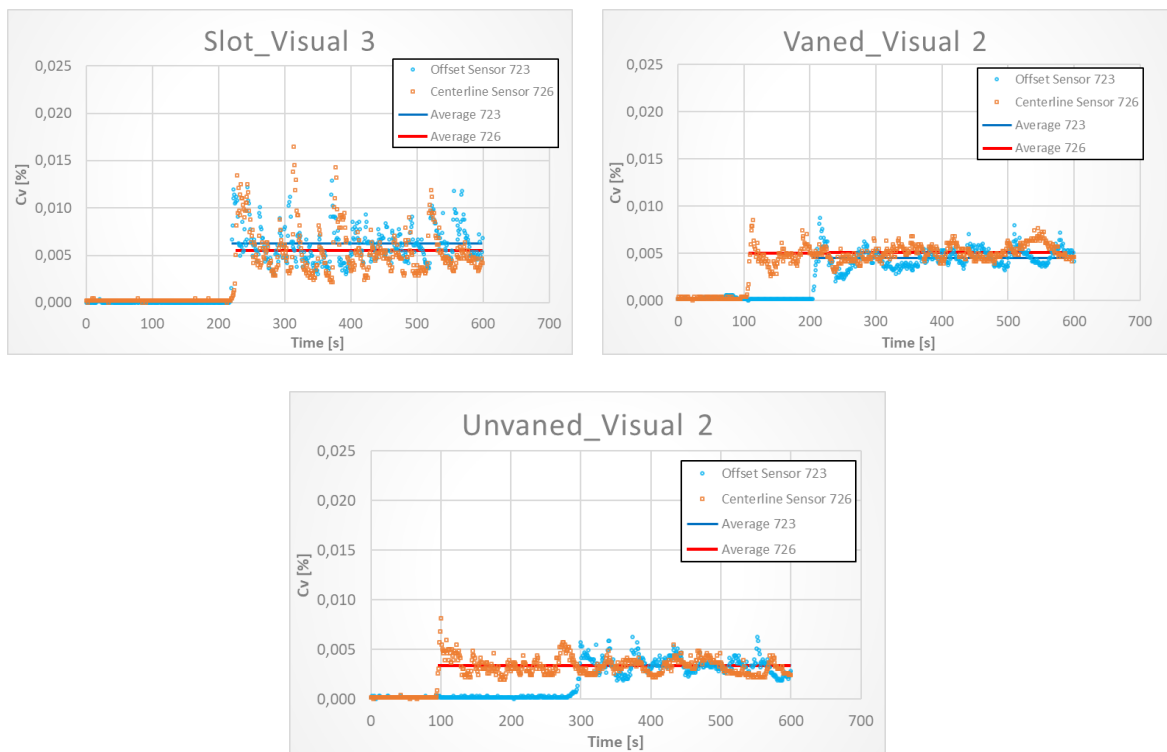

Figure B.8: Offset and centerline OBS sensor concentration-time series (Cvo = 3%)

C

Velocity Profiles
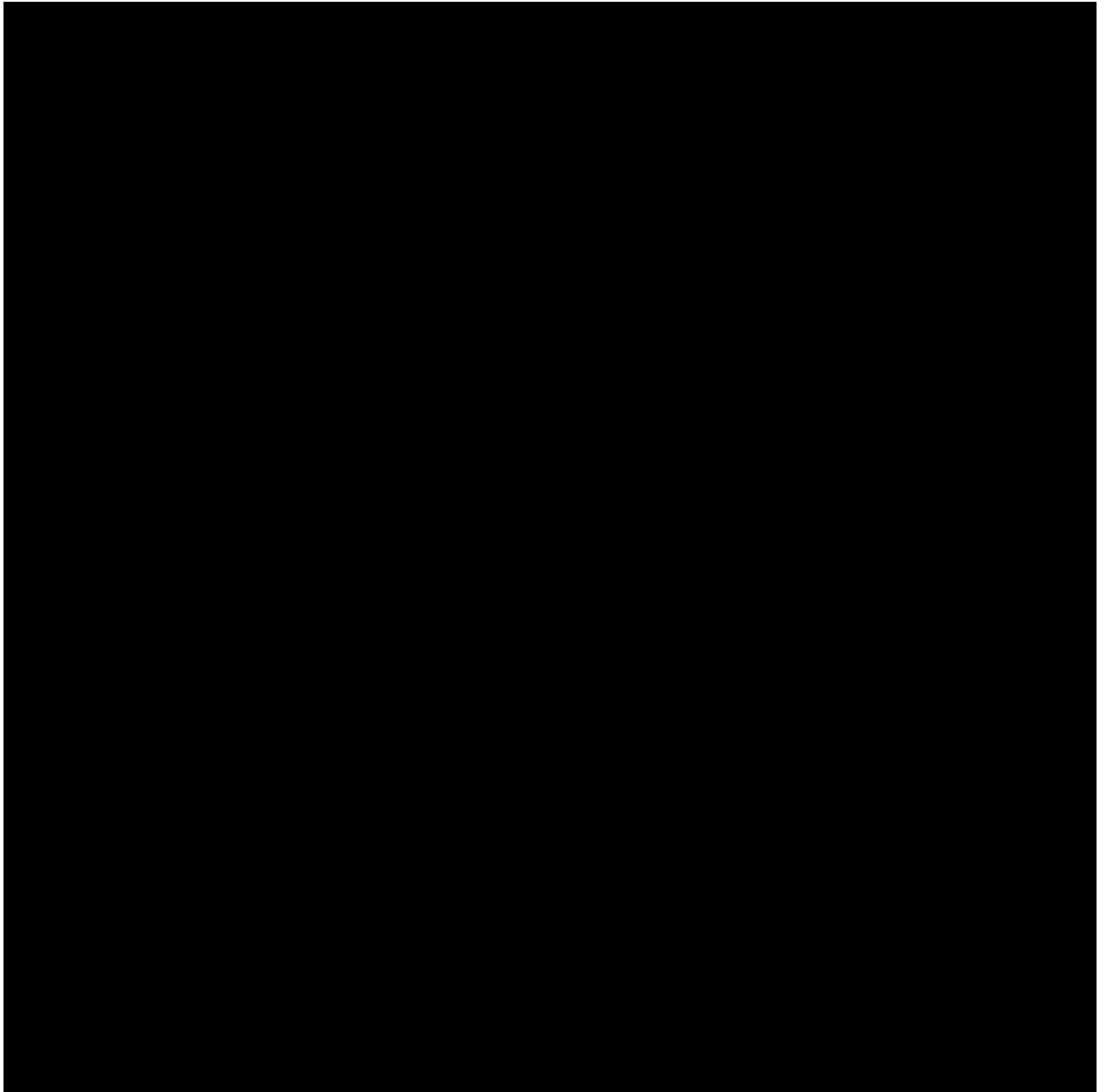
C.1. Slot Diffuser Velocity Profiles

Figure C.1: Measured and average velocity profiles Slot diffuser
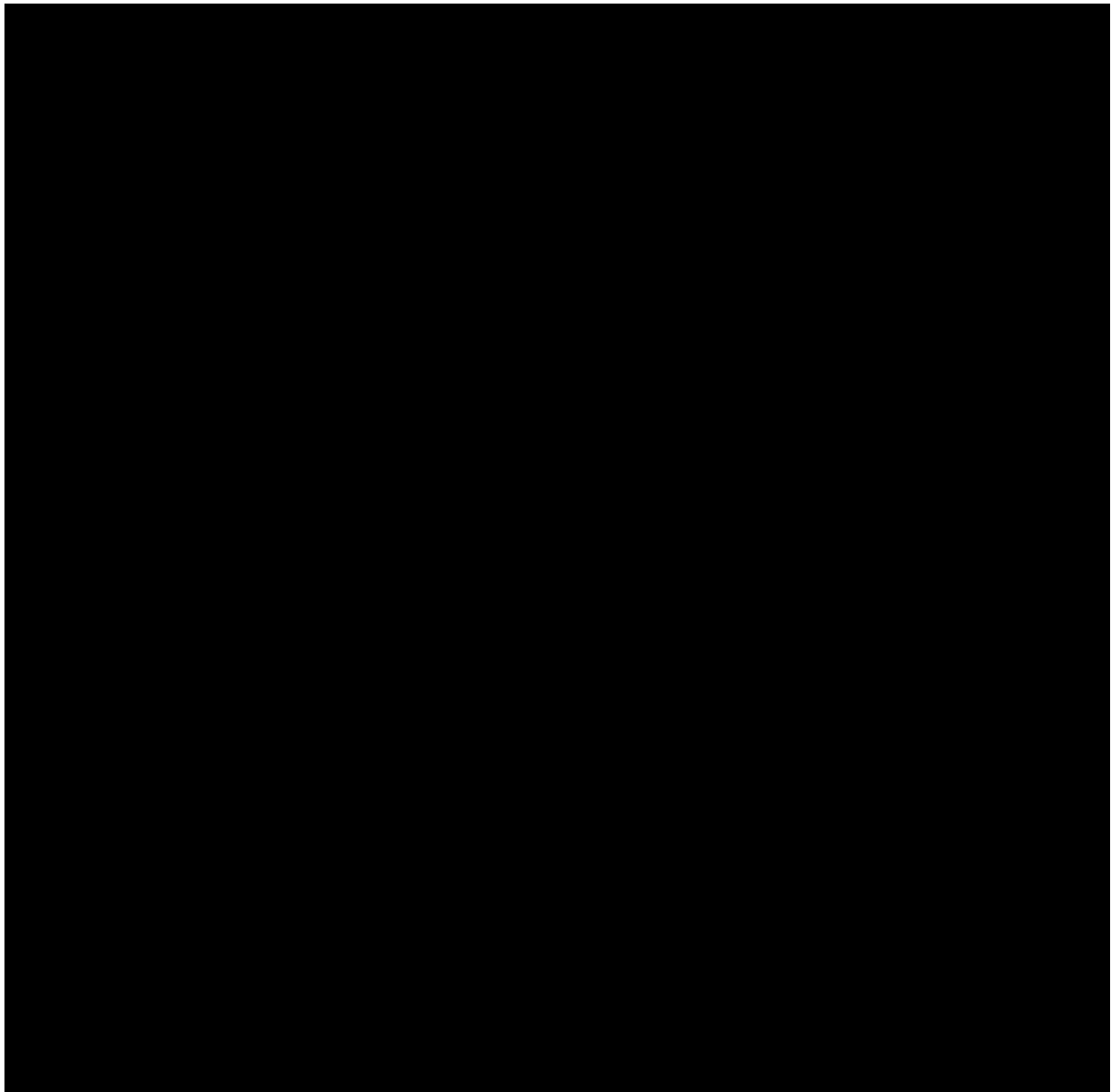
C.2. Vaned Diffuser Velocity Profiles

Figure C.2: Measured and average velocity profiles Vaned diffuser
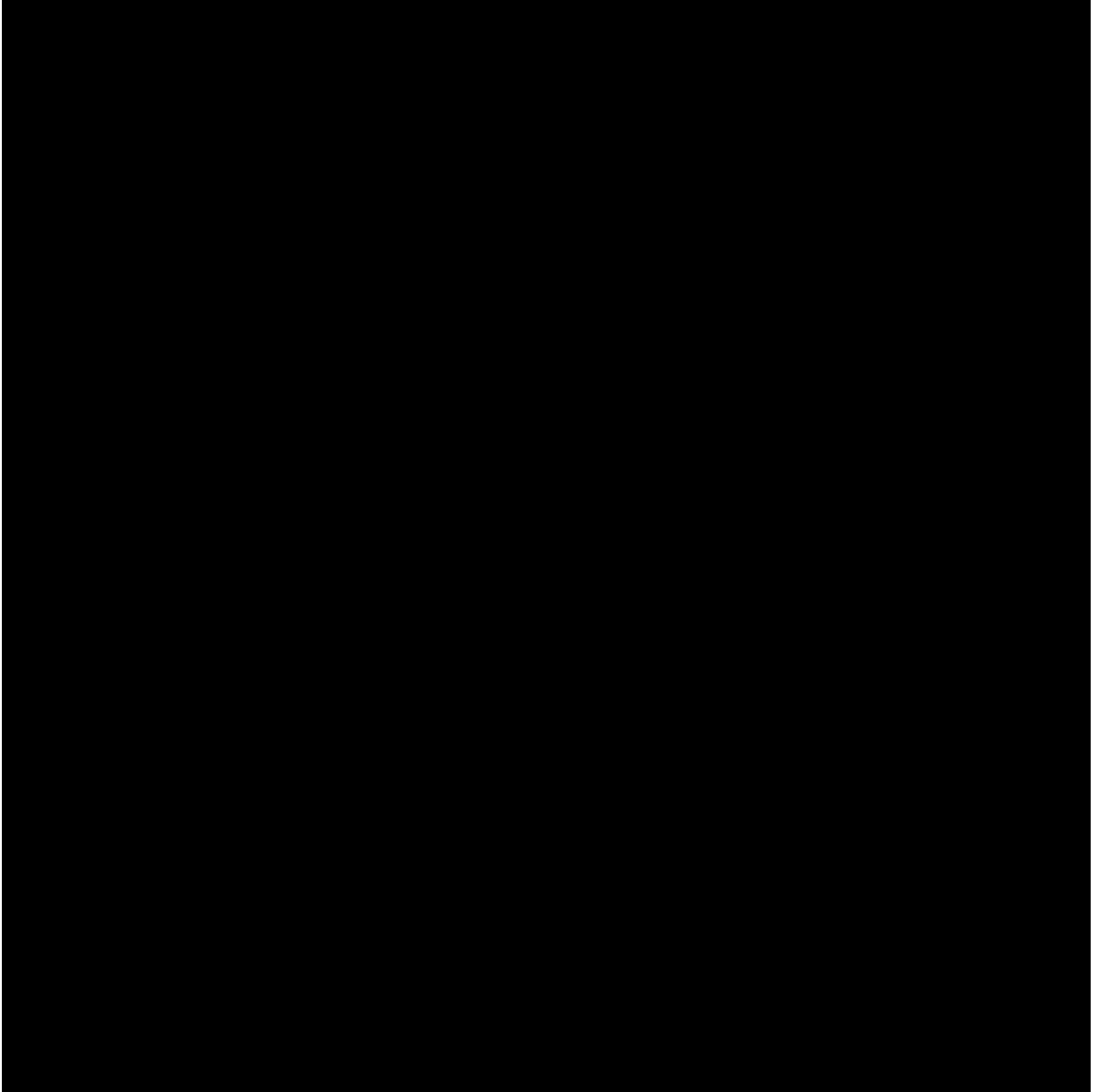
C.3. Unvaned Diffuser Velocity Profiles

Figure C.3: Measured and average velocity profiles Unvaned diffuser

D

Turbidity Measurements

D.1. Concentration Profiles

D.1.1. Slot Diffuser Concentration Profiles

Figure D.1: Measured concentration profiles Slot diffuser)
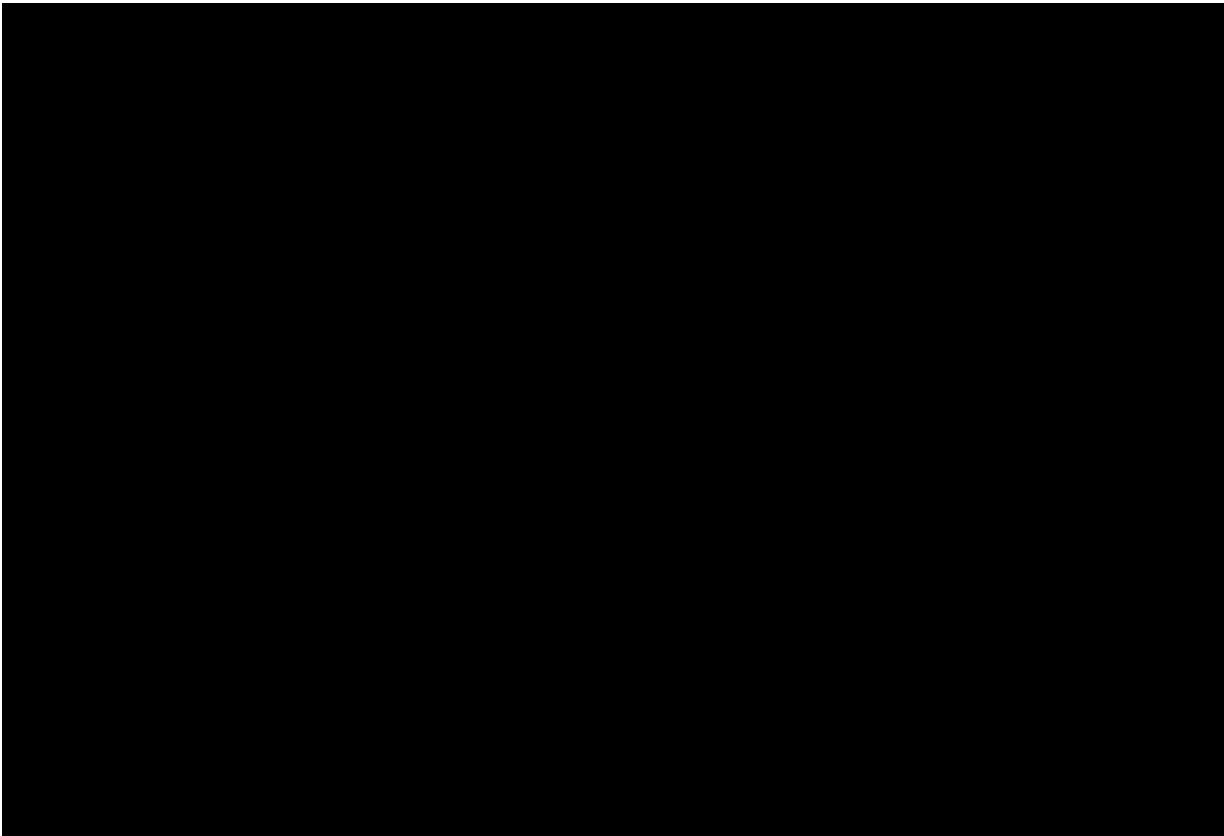
D.1.2. Vaned Diffuser Concentration Profiles

Figure D.2: Measured concentration profiles Vaned diffuser)
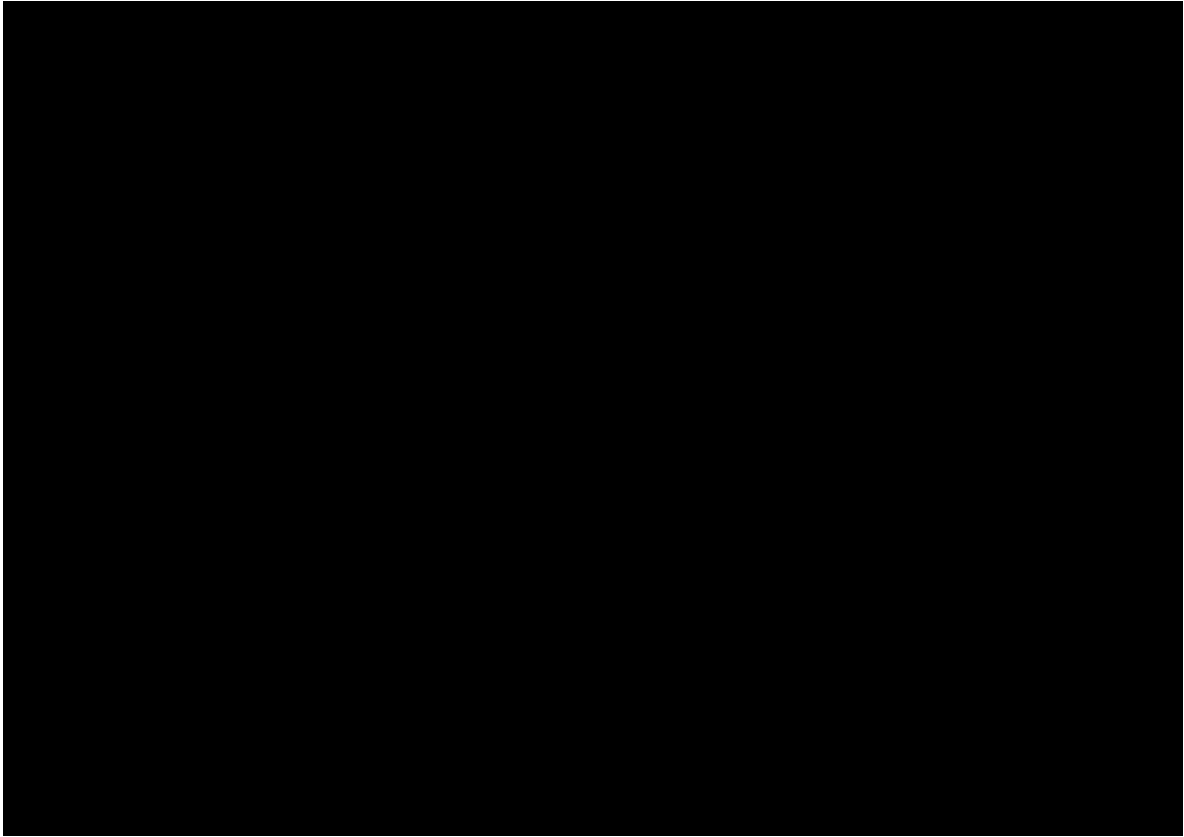
D.1.3. Unvaned Diffuser Concentration Profiles

Figure D.3: Measured concentration profiles Unvaned diffuser)

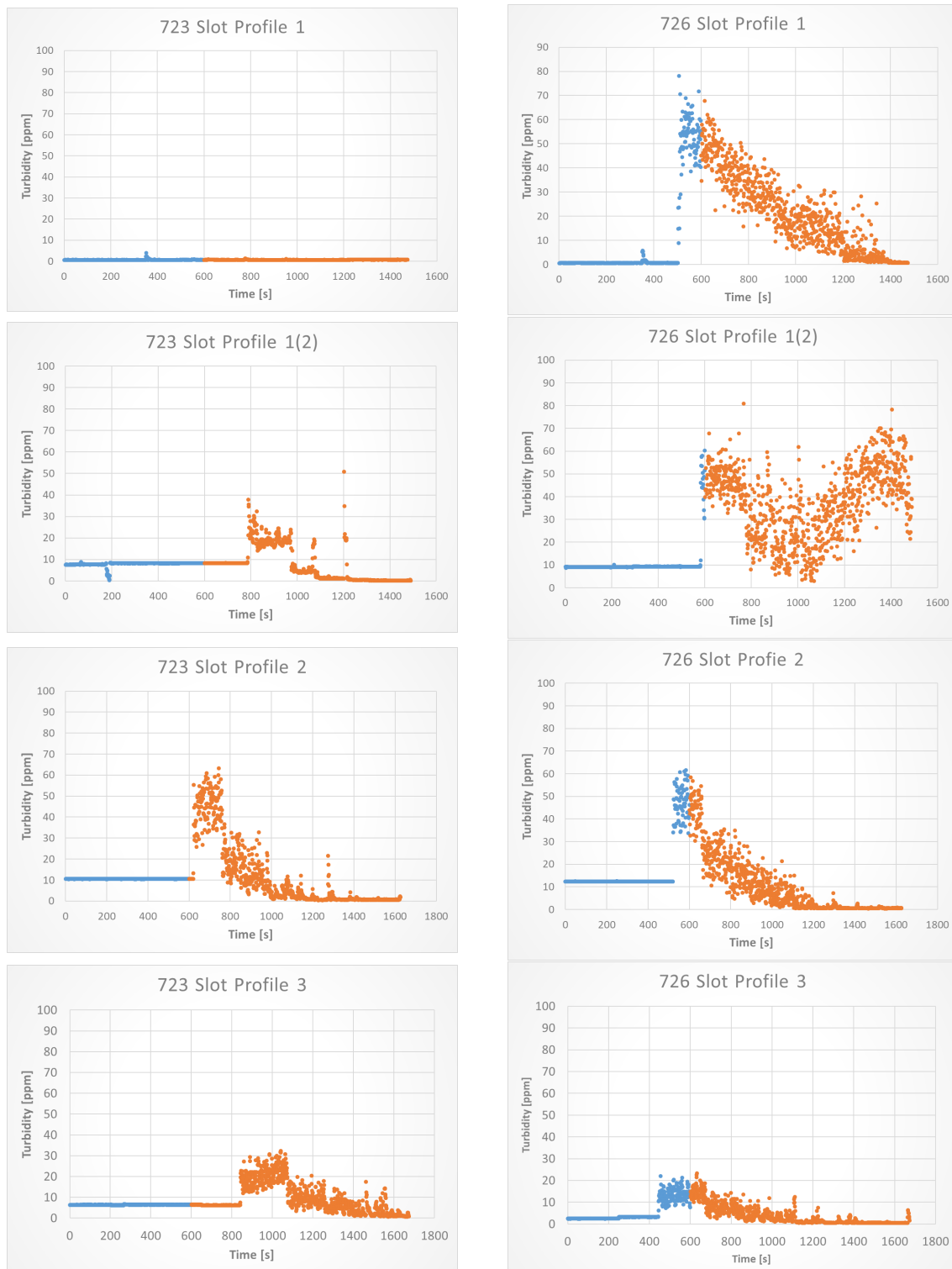# D.2. OBS Time Series

D.2.1. Turbidity Time Series - Slot

Figure D.4: OBS offset and centerline time series-Slot diffuser
Legend - Blue: Readings 10min before measurments / Orange: Readings during measurments

D.2.2. Turbidity Time Series - Vaned

Figure D.5: OBS offset and centerline time series-Vaned diffuser
Legend - Blue: Readings 10min before measurments / Orange: Readings during measurments

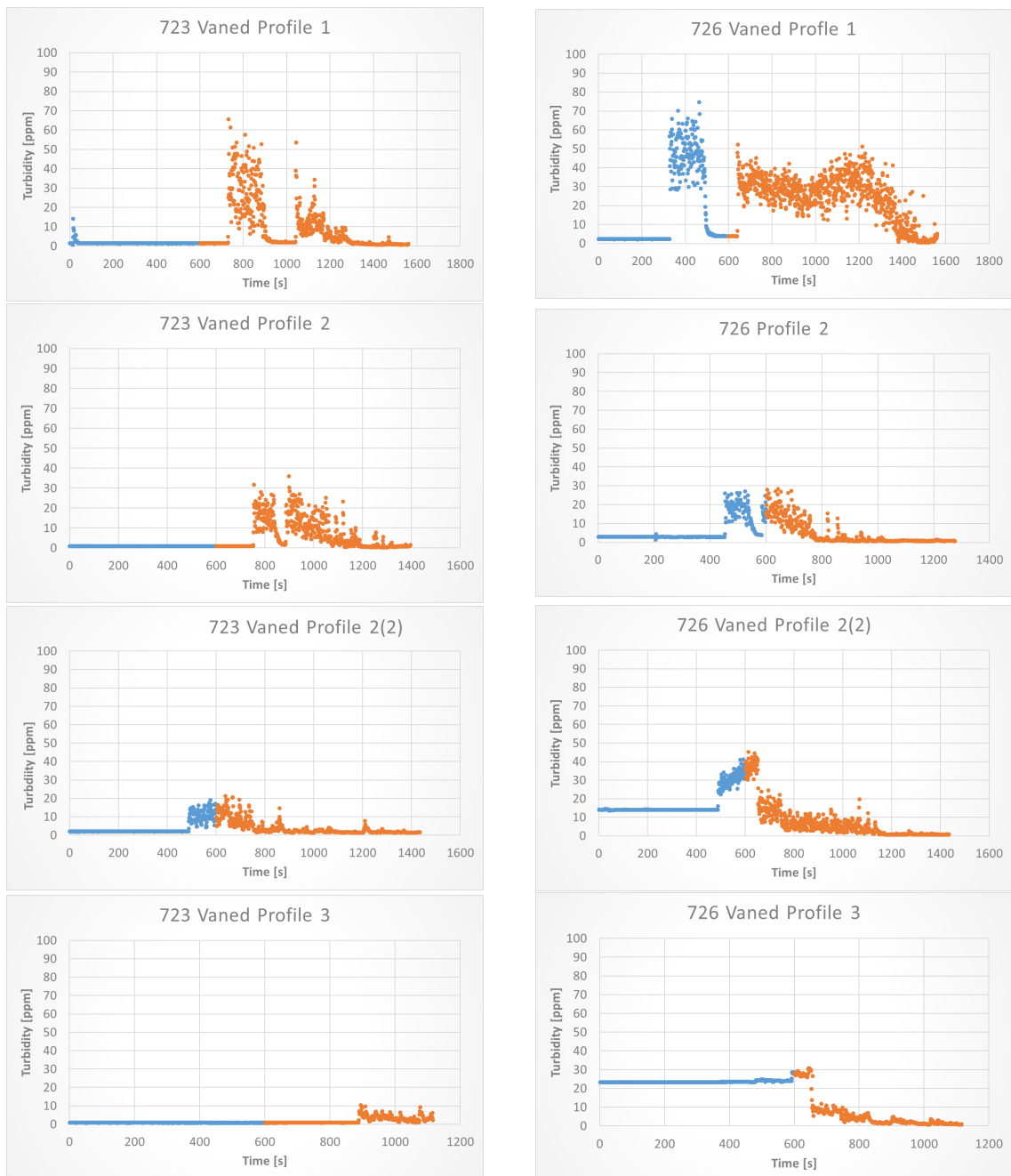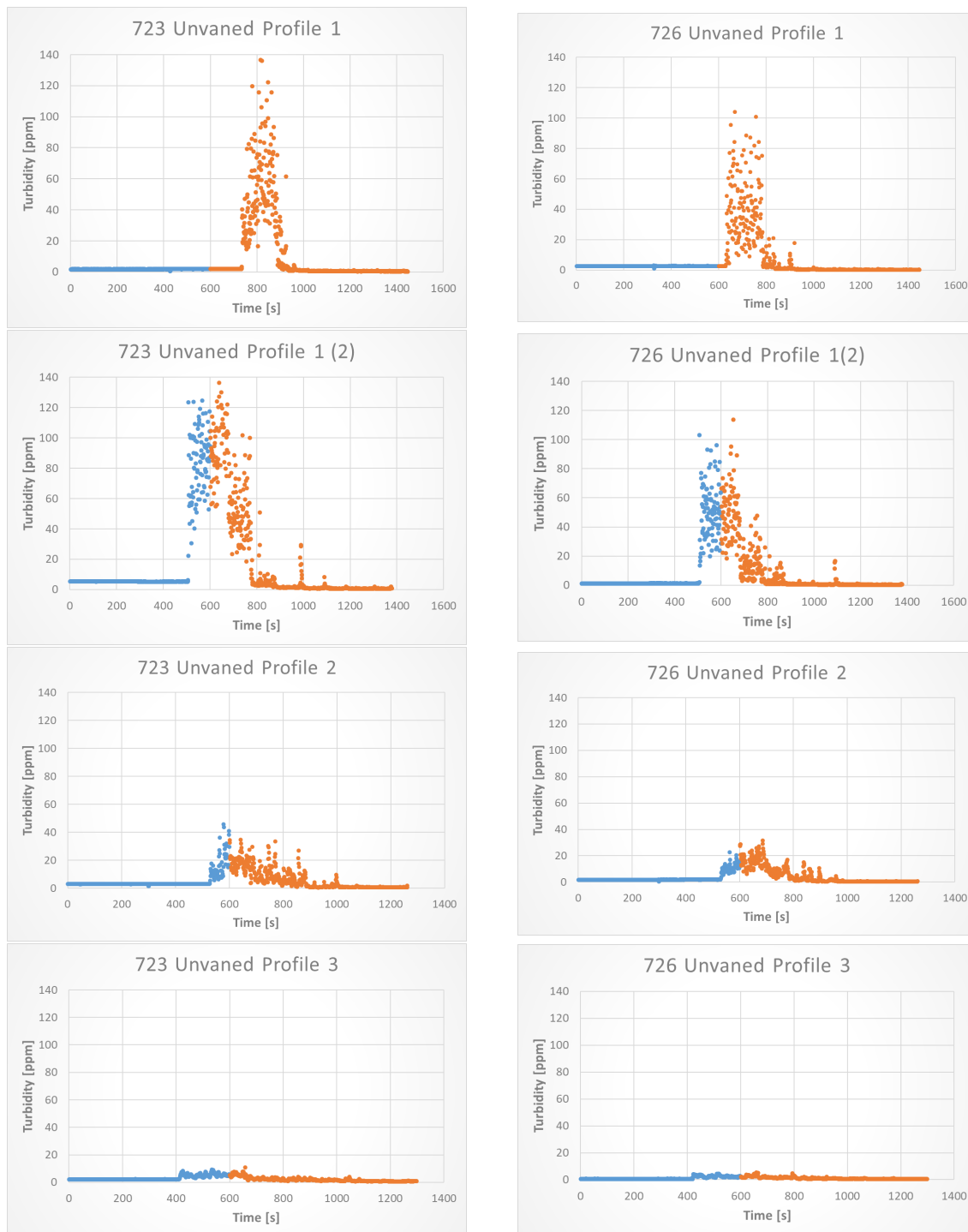### D.2.3. Turbidity Time Series - Unvaned

Figure D.6: OBS offset and centerline time series-Vaned diffuser
Legend - Blue: Readings 10min before measurments / Orange: Readings during measurments

D.2.4. Near Bed Turbidity Measurements

(a) Section A-A

(b) Section B-B

(c) Section C-C

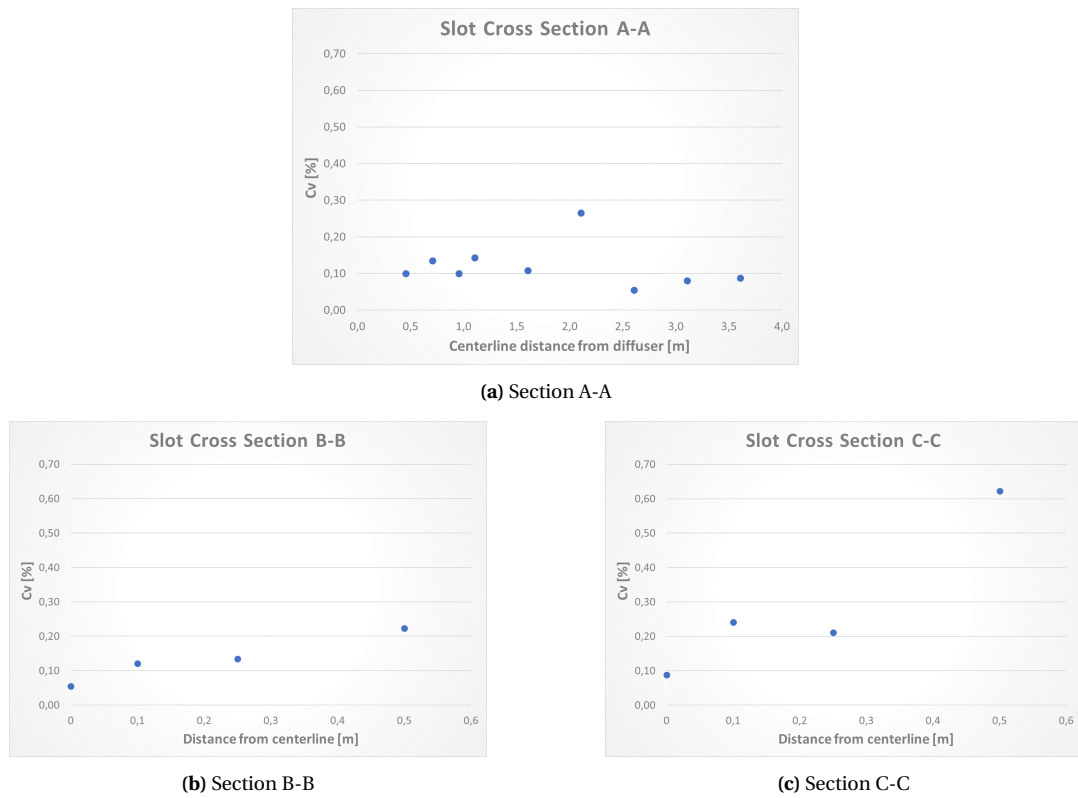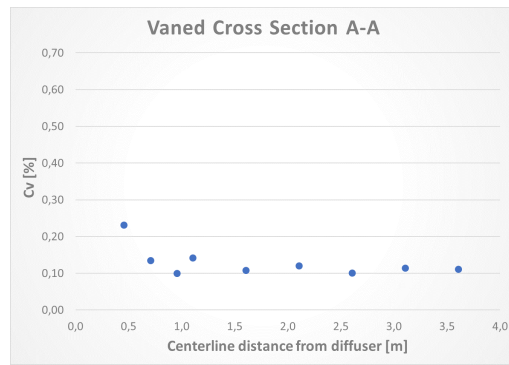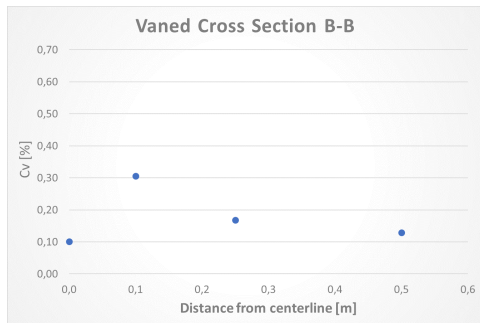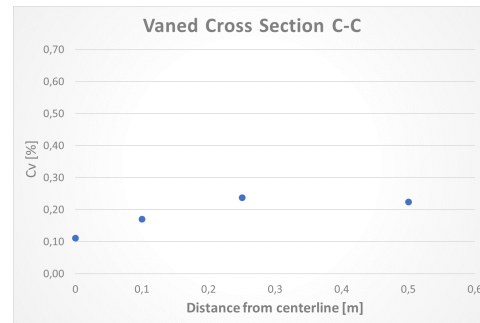**Figure D.7:** Near bed turbidity measurements Slot diffuser

(a) Section A-A
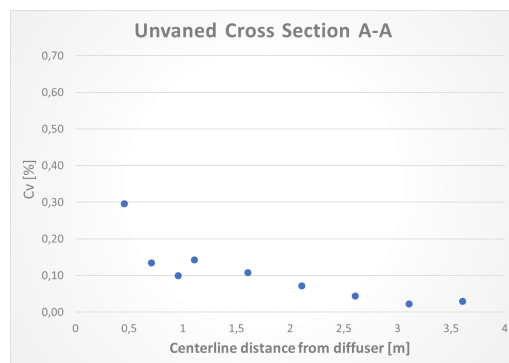

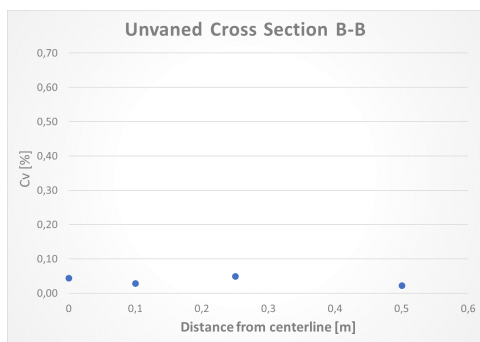
(b) Section B-B

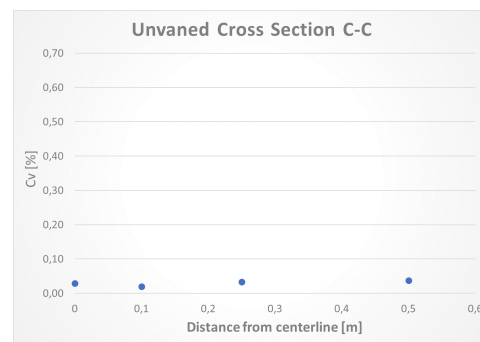**(c)** Section C-C

Figure D.8: Near bed turbidity measurements Vaned diffuser

(a) Section A-A

(b) Section B-B

(c) Section C-C

Figure D.9: Near bed turbidity measurements Unvaned diffuser

E
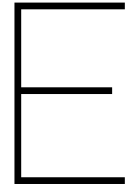
Sediment granulometric data and physical characteristics

E.1. Sediment General Information

PRODUCT INFORMATION

PRODUCT SHEET HM-PI-009-10/06

GLASS BEADS

Glass beads are made conform MIL-G-9954 A specifications.

CHEMICAL ANALYSIS	SiO_2 72 % AL_2O_3 < 2.5 % CaO 9 % MgO < 4 % Na_2O 13.7 % K_2O < 1.2 % Fe_2O_3 < 0.5 % SO_3 < 0.5 %
SHAPE	Round
NATURE	Inert
COLOUR	White
HARDNESS	6 Mohs
BULK WEIGHT	1.5 kg/dm³
SPECIFIC WEIGHT	2.46 kg/dm³
GRAIN SIZE	40 - 70 micron 65 - 105 micron 75 - 125 micron 90 - 150 micron 100 - 200 micron 150 - 250 micron 200 - 300 micron 300 - 400 micron 400 - 600 micron
PACKING	In 25 kg paper bags on pallets of 1000 kg each, covered with a shrink foil.
APPLICATION	Glass beads performance is cleaning of surface without roughening. Glass beads can be used in blast halls and cabinets. Besides cleaning of surface also surface hardening occurs Shot Peening.

HOLLAND MINERAAL bv
ABRASIVES AND BLASTING EQUIPMENT

Tielstraat 8   Tel. 31+(0)570-621161
7418 CS Deventer, Holland   Fax 31+(0)570-634336
www.hollandmineraal.nl   info@hollandmineraal.nl

E.2. Malvern Test Results

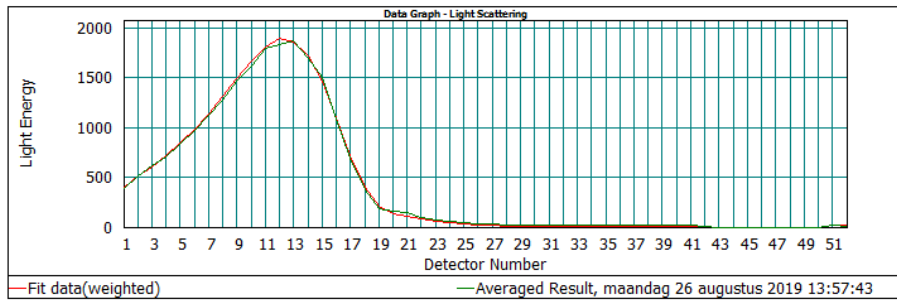|		
Sample Name:	**SOP Name:**	**Measured:**
Averaged Result		maandag 26 augustus 2019 13:57:43
Sample Source & type:	**Measured by:**	**Analysed:**
	fun_fcl	maandag 26 augustus 2019 13:57:45
Sample bulk lot ref:	**Result Source:**	
	Averaged	

Accessory Name:	**Obscuration:**
Hydro 2000MU (A)	13.33 %
Background integration time:	**Measurement integration time:**	**Background measured:**
5000 mS	5000 mS	maandag 26 augustus 2019 13:52:15

Particle Name:	**Analysis model:**	**Sensitivity:**
Default	General purpose	Normal
Particle R.I.:	**Absorption:**	**Residual:**
1.520	0.1	0.631 %
Dispersant Name:	**Dispersant R.I.:**	**Weighted Residual:**
Water	1.330	0.590 %

Data Graph - Light Scattering

Light Energy vs Detector Number

— Fit data(weighted)   — Averaged Result, maandag 26 augustus 2019 13:57:43

No	Weighted Data	Weighted Fit	Difference	No	Weighted Data	Weighted Fit	Difference	No	Weighted Data	Weighted Fit	Difference
1	387.63	402.72	-15.09	19	187.68	209.61	-21.93	37	16.75	6.02	10.73
2	511.71	506.43	5.29	20	159.63	132.52	27.11	38	16.77	6.20	10.57
3	611.44	600.29	11.15	21	145.61	104.00	41.61	39	16.52	6.30	10.22
4	697.35	710.24	-12.90	22	93.61	81.26	12.36	40	15.87	6.23	9.65
5	821.19	835.13	-13.94	23	67.69	58.47	9.23	41	14.50	5.94	8.56
6	962.01	975.65	-13.65	24	52.40	40.01	12.39	42	12.52	5.54	6.98
7	1115.57	1131.12	-15.55	25	39.65	28.68	10.97	43	0.00	0.00	0.00
8	1274.27	1301.72	-27.45	26	31.26	20.79	10.47	44	0.00	0.00	0.00
9	1463.52	1479.33	-15.81	27	25.95	15.31	10.64	45	0.00	0.00	0.00
10	1614.22	1653.49	-39.26	28	22.55	11.77	10.78	46	0.00	0.00	0.00
11	1785.34	1800.26	-14.92	29	20.33	9.31	11.02	47	0.00	0.00	0.00
12	1825.66	1881.56	-55.90	30	19.32	7.76	11.56	48	0.00	0.00	0.00
13	1860.44	1846.24	14.20	31	18.48	6.75	11.72	49	0.00	0.00	0.00
14	1680.25	1713.93	-33.68	32	17.28	5.95	11.33	50	0.00	0.00	0.00
15	1490.11	1452.02	38.10	33	16.70	5.59	11.12	51	23.65	22.83	0.82
16	1072.85	1092.38	-19.53	34	16.37	5.48	10.89	52	8.07	16.78	-8.71
17	687.28	710.08	-22.80	35	16.37	5.57	10.80				
18	366.41	396.44	-30.03	36	16.71	5.79	10.92				

Operator notes: Average of 25 measurements from test 26082019

Particle Size Distribution

Volume (%) vs Particle Size (µm)

— Averaged Result, maandag 26 augustus 2019 13:57:43

Particle Size Distribution

Volume (%) vs Particle Size (µm)

— Averaged Result, maandag 26 augustus 2019 13:57:43